Methodologies in XRF Cytometry

by

Andrew McCarten Crawford

A dissertation submitted in partial fulfillment
of the requirements for the degree of
Doctor of Philosophy
(Chemistry)
in the University of Michigan
2015

Doctoral Committee:
Professor James E. Penner-Hahn, Chair
Professor Mark Banaszak Holl
Professor Carol A. Fierke
Professor Janet Smith
Professor Shuichi Takayama

To my parents, Roderick and Sheila, with the utmost
gratitude for their unconditional love and support.
With all my love, always.

To my brothers Scott and Matt, who, at most times,
are the only people who truly understand me.

To my sisters Laura and Caitlynn,
I love both of you

To Emerita Mendoza Rengifo,
the love of my life.

and,

To the memory of
Candice Anna Waldrip
June 13, 1983 - May 1, 2015
May she finally be at peace.

ACKNOWLEDGEMENTS

First and foremost, I am grateful to my Ph.D. advisor, Professor James E Penner-Hahn, for his guidance during my graduate studies at the University of Michigan. Jim has provided the perfect balance of hands on training while allowing me the free reign to be able to explore and cultivate my own ideas. The primary reason I was able to conduct research at the University of Michigan is because Jim agreed to take me on as a student during my sixth (and thankfully final) rotation through laboratories during the first 1.5 years of my doctoral studies. I am continually amazed by the degree with which Jim cares about his students and the extraordinary lengths to which he goes to help us succeed. Even though he is the associate dean of budget for LSA (a job that requires much of his time), I could never really tell it he has always responded to emails within a day or two. In fact, the only time I can remember not being able to hear back from him right away was Christmas; he had turned off his phone to spend time with his wife. I am beyond grateful for the scientific education I have received from him. I will always be proud to have come from his lab.

Second, I need to thank Dr. Aniruddha Deb, a research scientist in our group. When I first began research in the Penner-Hahn group, Aniruddha was primarily in charge of the cytometer project. We worked closely together towards the development of a microfluidic chip based design that ultimately didn't work. Even though I took the project in a different direction, Aniruddha has been there to encourage and guide my thought processes throughout. His encouragement, especially in these last few stages of my Ph. D., has been amazingly supportive.

He truly cares about the students with whom he works; and there have been times that he has stayed up with me until 3am helping me finish a project.

Also I appreciate all the guidance and instruction of my committee members, Prof. Mark Banaszak Holl, Prof. Carol A. Fierke, Prof. Janet Smith, and Prof. Shuichi Takayama Their feedback and encouragement during my candidacy exam and data meeting was instrumental in the development of my project. Without their support I may have finished my Ph.D. studies quite differently. I'd like to especially thank Prof. Smith for her class on X-Ray Crystallography as well. That class is why I asked her to be on my committee. I would like to specifically thank Prof. Carol Fierke for giving me a chance to do a rotation in her lab and the use of her lab during my short time in the Penner-Hahn lab.

I owe special thanks to my fellow (past) lab member Dr. Soojeong Kim. Our friendship went beyond the science. I would like to thank Soojeong for being a supportive friend and colleague who always encouraged me when I needed it. Most importantly, I need to thank her for running the gauntlet of "formatting a thesis" and then giving me all her notes on it. These notes were instrumental.

I want to thank Dr. Lubomir Dostal and Andrea Stoddard of the Fierke Lab for friendship and collaboration. I want to additionally thank Lubos for support and some really awesome expressway discussion on our road trip to APS. I don't think he realizes how much he has influenced and supported me during times of doubt just by saying the words, "you'll get it done".

I want to thank the executive officers of the Chemistry Graduate Student Council, who served with me. They are, Heidi Alvey, Heidi Hendrickson, Kevin Hartman, Matt Kahlscheuer, Kim Daley, and Andrew Molina. Their friendship has been instrumental in my professional and personal development. I owe Heidi Alvey (as well as, Jo Yourey, Tiberius Moran Lopez, Nicole

Warner, Edward Poisson, Ashley Poisson, and Corinne Tabb, all of who are not past executive officers) special thanks for watching my house and animals while I was away at Argonne National Laboratory conducting my Ph.D. research.

It would have been impossible for me to have made it this far without family and friends. There are too many people to name, and I want to say thank you to all of you.

To Dr. Kathleen Nolta and Dr. Nancy Konigsberg-Kerner, thank you for my experiences teaching general and organic chemistry labs and biochemistry discussions.

To Scott and Matt, thank you both for being my equally closest confidants over the last ten years. I love you both and my life would be very different if I didn't have both of you to remind me that it is okay to be me.

To Emerita Mendoza Rengifo, your encouragement has been amazing. I can't believe I get to spend the rest of my lifetime with you. I can't wait until I can call you "Dr. Mendoza".

Finally, thank you Roderick and Sheila Crawford (my parents). Thank you for always being there. Thank you for being the best role models for who I wanted to become. Thank you for always believing in me. Thank you for giving me perspective on things when I could only see right in front of me. I love you both. I always will.

Table of Contents

List of Figures

List of Tables

ABSTRACT

The "inorganic physiology" of a cell – that is, the storage, uptake, efflux and regulation, of metal ions, is critical to understanding the role(s) that metal ions play in biology. Two new methods for cellular elemental analysis are developed. The first is the creation of an x-ray fluorescence flow cytometer that can determine the total elemental content of single cells. This instrument can directly measure population heterogeneity for metals in the μM to mM concentration range with fL sample volumes, a measurement that is difficult using most analytical methods. Bovine red blood cells (bRBCs) were found to have mean concentrations of ~100 μM Zn and ~15 mM Fe; NIH3T3 and yeast contained ~50 μM Zn and ~130 μM Zn, respectively. These data demonstrated that there is significant variability in the Zn and K content of NIH3T3 cells and in the Fe content of bRBCs. Fe content for bRBCs showed a 1.9-fold difference between the lowest and highest quartiles, variability that is dominated by biological variability and not experimental uncertainty. Likewise, NIH3T3 cells showed 2.3- and 2.8- fold differences between the 1st and 3rd quartiles for Zn and K, respectively.

Second, fitting methods for x-ray fluorescence microprobe imaging were improved. A major advancement was the development of a blank subtraction method to correct the background and calculate elemental concentrations; this gives a significant improvement in quantitation.

Comparison of the new method against the more commonly used baseline subtraction demonstrated not only better precision, but also improved instrument calibration. Differences in quantitation are biologically relevant. Additionally, blank subtraction allows superior sensitivity, best demonstrated with the detection of Cl. This method was used to image and determine the elemental content in NIH3T3 cells in the presence and absence of Cd, confirming 3-fold decrease in Zn content following Cd exposure.

CHAPTER I: THE METALLOME, X_RAY FLUORESCENCE, IMAGING AND FLOW CYTOMETRY

I.1 INTRODUCTION TO METAL HOMEOSTASIS

Metals perform a multitude of functions inside cells. They are crucial components of redox reactions [1]; act as cofactors in the active sites of protein enzymes; bind to structural proteins to aid in stability; stabilize the backbone of nucleic acids (primarily Mg^{2+} and K^{+}) [2-4]; provide tertiary structural stability for functional RNAs [4-9]; are required mediators in many functional RNA ligand binding recognition events via direct participation in the binding pocket [10-12], indirect participation in the binding pocket [13, 14], and as metal-ligand chelates [15-18]; and participate in the regulation/expression of certain genes [19, 20]. This list is not exhaustive.

Under some conditions, metal ions are capable of participating in numerous deleterious reactions. Such reactions include the production of ROS (reactive oxygen species) which can damage DNA (via base oxidation or loss, strand breaks, and DNA-protein crosslinking) [21-23], lipids (via peroxidation) [23, 24], and proteins (via oxidation) [24]. Depletion of nutrients can also occur via metal ion inhibition of cellular processes, such as that caused by Ni^{2+} and Co^{2+} inhibition of ascorbic acid uptake [25]. Metal ion associated inhibition of enzymes involved with DNA repair has been demonstrated [26, 27]. Irreversibly compromised protein function has also been shown, e.g., toxic levels of $Co^{2/3+}$ have been shown to compromise the function of Fe-S cluster proteins, for *Salmonella enterica*, in a manner that is irreversible with Fe supplementation

[28]. As such, aberrant metal ion compartmentalization, localization, concentrations, and oxidation states are correlated with a multitude of diseases and disease states; and in some cases result in death. As an example, uncontrolled ROS generation has been correlated with (or been shown to cause) disease states that include male infertility [29], prostate [30] and other cancers [24, 31-34], neurodegenerative disorders (Alzheimer's, Huntington's [35, 36], and Parkinson's disease) [27, 35-40], cardiovascular disease [41, 42], respiratory disease [43], and diabetes [21, 44] as well as inflammation [27]. Additionally, faulty metal homeostasis leading to abnormally high Fe levels have been linked to type-2 diabetes [45], atherosclerosis [42], Parkinson's and Alzheimer's diseases [46, 47], and various cancers [48, 49] including prostate cancer [33]; in parallel, high levels of Cu have been correlated to Parkinson's and Alzheimer's diseases [47] and cancers [48, 49].

Additionally, the cellular uptake of toxic metals can result in deviations from cellular homeostasis. For example, Zahler et al. combined XRF imaging with bulk sample analysis to demonstrate that cadmium toxicity is correlated to altered copper homeostasis via the redistribution of copper within the cell presumably due to the induction of genes involved in metal uptake. Cadmium exposure also resulted in increased levels of zinc and iron and as such the combined disruption in homeostasis for all three transition metals may contribute to the toxic effects of cadmium [50]. In line with this, Cd has been found to be a biological mimic of Zn in terms of its ability to bind substrates [51]. In this manner, Cd has been shown to be able to exert transcriptional influence over the expression of Zn transporters [52]. Additionally, increases in intracellular Zn have been attributed in *Saccharomyces cerevisiae* to increased expression of Fet4, which transports Cu, Fe, and Zn [53, 54].

Dietary disruptions can also upset metal ion homeostasis. For instance, disruption of Cu ion homeostasis has been demonstrated in cases of Zn supplementation as well as following gastric surgeries (reviewed in [55]) such as gastroectomy, and gastric bypass [56-59]. With gastric bypass, dishomeostasis of Cu ions results as the removed (or bypassed) organs contain most of the sites responsible for copper absorption in humans [56, 59]. Additionally, this surgically imposed malabsorption may have deleterious effects on the acquisition of trace metals as post-surgery patients have been found to be Fe deficient [55] and to have low blood Zn [57], both of which can lead to neurological findings and symptoms.

Likewise, genetic disruption of metal ion homeostasis can result in many specific symptomatic disease states. Among the best studied include copper and/or iron. Both excess and deficiency of copper or iron result in central nervous system disorders and disease. The following examples of both Fe and Cu genetic disease states were reviewed very well by Madsen et al. [60]. In terms of Cu, inappropriate homeostasis has been linked to Menke's disease and Wilson’s disease; and faulty homeostasis of iron has been shown to cause aceruloplasminemia, neuroferritinopathy, Friedreich’s Ataxia, and brain neurodegeneration due to iron accumulation. Although much has been learned genetically about diseases such as Menkes and Wilson’s revealing much about the cell biology of metal metabolism (copper in the case of Menkes and Wilson’s), there is still information that has yet to be learned [60].

The above facts outline the need for specific regulation of metal ion concentrations and activities both within and across cells; however, maintaining the appropriate levels of the functionally relevant/necessary metals is met with difficulty as environmental metal ion concentrations fluctuate constantly, making it necessary for cells to have evolved adaptive physiological responses to these fluctuations. Accordingly, cells have evolved complex regulatory mechanisms at transcriptional, post-transcriptional, and post-translational levels that are responsive not only to metal ion availability but also, among other things, oxygen levels (as in the case of *S. cerevisiae* transcriptional level regulation of Fe). A comprehensive review by Dlouhy and Outten [61] discusses all three levels of Fe homeostatic regulation for *S. cerevisiae*. These regulatory mechanisms ensure adequate, but not toxic, intracellular metal ion concentrations; and at the same time prevent the mis-metallation of proteins. However, the understanding of these homeostatic mechanisms is still in its infancy; and the interplay between metal ions in living organisms continues to be an extensively studied and growing field.

I.2 AN EXAMPLE OF METAL HOMEOSTASIS: THE ZAP1 REGULON OF YEAST

As an example of cellular homeostasis involving the metallome, consider the homeostatic regulation (e.g., the uptake, utilization, storage, conservation, and export) of Zn by the Zap1 regulon in *S. cerevisiae*. Optimal growth for *S. cerevisiae*, in terms of Zn, occurs at a concentration of 1.5×10^7 Zn atoms per cell (the Zn quota) [62]. Below this concentration, suboptimal growth occurs with the lower threshold being 5×10^6 Zn atoms per cell; below that, all cell growth halts. During Zn replete conditions, vacuolar storage can account for up to 7×10^8 atoms of Zn atoms per cell [63]; this is enough Zn to allow for eight generations of progeny during conditions of Zn starvation. Conservation during Zn starvation includes cross talk with Fe homeostatic regulation leading to the down regulation of Zn-dependent enzymes accompanied by the up regulation of both their Fe-dependent counterparts as well as Fe importers [64]. Zn regulation at the transcriptional level includes Zap1, a transcription factor which directly senses Zn and resides only in the nucleus under all conditions [65]. Its expression under Zn limited conditions coincides with the up-regulation of >80 genes [64, 66-70] and the predicted down-regulation of >30 genes [44]. Homeostatic responses of Zap1 to Zn deficiency are multifold and include, auto-regulation [71], Zn^{2+} sequestration [72-74], Zn^{2+} mobilization [64, 66, 67, 69, 75-78], Zn^{2+} conservation of via down-regulation of Zn-dependent enzymes [64, 79] with the synchronous up-regulation of analogs dependent on either less Zn or another element entirely [80], remodeling of sulfate metabolism [81, 82], and remodeling of phospholipid metabolism [83, 84]. Collectively, these changes function to, among other things, avoid misfolded proteins from the endoplasmic reticulum [85, 86], safeguard against potential future Zn shock [76], and to conserve NADPH to combat increased formation of reactive oxygen species; all of which are coincident with Zn depleted cellular status.

This example is specific to *S. cerevisiae* and Zn. It serves to demonstrate the complexity associated with the methods employed by organisms to maintain metal homeostasis. Since there are countless other essential biominerals (e.g., Cu, Fe, Mn, Co, and Ni), and since it is known that the homeostatic regulatory mechanisms that govern mobilization, utilization, and compartmentalization of these minerals are able to cross-talk, one quickly can see why the study of these mechanisms is quickly becoming a field of its own.

I.3 IMPORTANCE OF SINGLE CELL ANALYSES

I.3.1 HETEROGENEITY OF CELL POPULATIONS (SINGLE CELL ANALYSIS)

Davey et al. have stated that because of the existence of thresholds, cases of unforeseen heterogeneity across populations of cells are to be expected in fluctuating systems, whose gene expression is controlled by a small number of repressor molecules or other elements [87]. The driving force behind the need for single-cell methods is the possibility of otherwise undetectable heterogeneity, which can arise from five key factors: genetic, biochemical, physiological, behavioral, and environmental. Such heterogeneity is the foundation of biological stability and survival as it allows organisms to adapt and survive adverse conditions. As such, microbial populations exhibit multitudes of genetic and phenotypic differences among their constituent members. Additionally, heterogeneities have been observed in cell populations that arise from a single parent cell [88]. Importantly, it has also been noted in some cases that subpopulations can direct the behavior of whole populations [89]. Therefore, the importance of single cell measurements finds its value in its ability to dissect the heterogeneity inherent in populations of cells [90]. Bulk-scale measurements, as opposed to individual cell-by-cell measurements, fail to capture these discrete properties, in turn, producing “average” answers; such average answers may be very misleading, especially in cases such as [89]. Properties such as cellular metal concentration, production of a specific gene product or protein concentration are specific to each individual cell.

I.3.2 THE POTENTIAL EXISTENCE OF SUBPOPULATIONS AND SKEWS

Although the $[free\,metal]_{Cell}$ in yeast can vary by 4 orders of magnitude [91], the $[total\,metal]_{Cell}$ only varies by ~2 orders of magnitude (e.g., yeast is ~140 [63, 92]). Under environmental conditions of Zn starvation, this allows 8 generations before the $[total\,Zn]_{Cell}$ becomes nonviable. Because of this, one might expect the distribution of metal concentrations across a population of cells to be skewed rather than Gaussian. A skewed distribution results from the presence of more cells at lower concentrations of total metal than at higher concentrations. Such a distribution would coincide with the existence of upper and lower thresholds that control the activation and deactivation of genes involved in metal homeostasis. For example, assume that a cell is able to undergo N rounds of reproduction in the window between the upper and lower thresholds. Starting at the highest possible concentration, the first division will lead to 2 daughter cells which will contain half the amount of metal as the original parent cell. Upon each subsequent division, the total number of cells will double but the total metal per cell will be half of the immediate parent cell. This will happen until N rounds of replication cause the metal content of each cell to drop below the minimal threshold. This will lead to the reactivation of cellular metal uptake, which will the cause the associated cells to replenish their stores of the metal (ideally) to the level of the upper threshold. Following millions of rounds of replication, the population distribution arising from a single cell can be separated into N distinct populations depicted by a population constituency ratio of 2^0:2^1:2^2:,…,:2^{N-1}, with relative concentration ratios of $\left(\frac{1}{2}\right)^0 : \left(\frac{1}{2}\right)^1 : \dots : \left(\frac{1}{2}\right)^{N-1}$respectively. For instance, if N is 5, this leads to a population constituency ratio of 1:2:4:8:16 with relative concentration ratios of $1{:}\frac{1}{2}{:}\frac{1}{4}{:}\frac{1}{8}{:}\frac{1}{16}$. This would create a population distribution that is slanted (or “skewed”) towards lower concentrations as there will always be an exponential number of cells at the lower concentration. As an example, **Figure I.1** models a resultant skewed population following 35 replication events (starting from a single cell) as well as the distribution plot of the skews obtained from randomly generating pseudo-normal distributions of two different sample sizes.

The above example outlines the formation of a skew and is but one explanation for the existence of small subpopulations for a particular trait/property (metal content in the example above) existing among a total population. It is possible that, due to variable expression of entire genomes combined with the heterogeneity that is ever present in all environments, subpopulations may arise. Importantly, without a technique capable of investigating a population of cells, individually, it is impossible to adequately detect the existence of subpopulations.

I.3.3 A STATISTICAL JUSTIFICATION FOR SINGLE CELL TECHNIQUES

Even in the absence of a skewed distribution, the importance of heterogeneity can easily be understood via a quick statistical analysis. Assuming a normal distribution for any particular trait, 95% of the population under investigation will be distributed within two standard deviations of the mean population value for that trait. As the number of traits considered increases, the likelihood that any cell will contain those traits within two standard deviations decreases according to 0.95^N; where N is the number of traits under inspection. Likewise, as the number of cells increases, the chance that those cells will all have a given single trait within two standard deviations of the population mean, also decreases according to 0.95^N; where N is the number of cells under inspection. Since cells have thousands of genes controlling things such as metal ion content, metabolite uptake, response to environmental variations (which are themselves heterogeneous), this means that heterogeneity is ever present in cell populations and understanding homeostatic mechanisms that govern, for instance, trace metal content, in cells can, therefore, not be understood by treating cultures as ensembles of identically constituent cells; for no two cells will ever be identical [88, 89, 93]. This highlights the huge advantage of (and the absolute need for) single-cell methods over bulk-scale methods, if one wants to directly measure the heterogeneity [90].

In comparison to single cell measurements, bulk-scale measurements fail to capture discrete properties inherent in populations, and, in turn, produce only average answers. For example, entertain a hypothetical study in which the total metal of a cell population being monitored doubles. This could result from all the cells doubling their metal concentrations or half the cells quadrupling their metal concentrations or any other combination that produces a doubling in the average metal concentration. Such average values provide no details of population distribution which is, in most cases, just as important as the mean value.

To date, there have been very few studies that are capable of speaking to the interplay of these properties with single cell precision. This makes a very strong case for the need of single-cell methods capable of analyzing population size data sets in appreciable amounts of time and thereby providing direct measurement of the heterogeneity that bulk-scale measurements miss. Methods such as microfluidic cytometry and x-ray fluorescence microscopy (XRM) have permitted single cell interrogation, and have enabled a level of understanding far superior to that which is accessible via population-scale approaches [94].

Through the use of optical probes it is possible to simultaneously gain information pertaining to cell size, cell cycle, and gene expression levels; combined with metal detection techniques such as ICP-MS or X-ray fluorescence (among others) it becomes possible to correlate changes in concentrations to changes in expression, degradation, and localization of gene products. Together, methods such as microfluidic cytometry and x-ray fluorescence microscopy are capable of analyzing cell specific properties enabling a level of understanding far superior to that which is accessible via population-scale approaches [94].

I.3.4 REQUIRED SAMPLE FREQUENCY/TURNOVER

Figure I.1A illustrates a skewed population based on > 50,000,000 cells arising after 35 replication events. This distribution has a skew of 1.7. **Figure I.1**B demonstrates the accuracy with which skew can be determined for different numbers of observations, n (15 vs. 500). This means that, realistically speaking, in order to adequately investigate a population of cells, the data set needs to include on the order of, at least, ~1,000 cells; ~10,000 cells would be ideal. Conventional XRF imaging techniques take, on average, ~1 hour/cell (if not more). This would require 10,000 hours to accrue such data (this is completely neglecting down time between samples, of course). Since beam time at national synchrotrons is limited to a few days, this leaves the other 9,928 required hours of data collection unaccounted for. In contrast, a better scan time, working backwards, would be 10,000 cells / 3 days. This works out to ~ 0.04 Hz or 1 cell every 25 seconds. Such sample frequency is entirely possible with cytometric techniques. Although such a sample frequency would be considered extremely slow by traditional flow cytometry standards - which are capable of sampling rates on the order of 2K cells / second - the required integration time of XRF flow cytometry (~0.25 seconds for the purposes entailed herein) coincides nicely with such a sample turnover rate.

I.4 COMPARISON OF METHODS FOR METAL ANALYSIS

The following section compares and contrasts the use of mass spectrometry, metal specific organic fluorophores, and intrinsic x-ray fluorescence as tools to explore the cellular metallome. For a more thorough discussion of techniques, please see [95-98].

I.4.1 MASS SPECTROMETRY

In mass spectrometry, a small portion of sample is isolated, ionized, and then separated and detected. Mass spec generally has a wide dynamic range (important for application to heterogeneous samples) and is known for its spectacular detection limits due to its ability to detect single ions [99]. This corresponds to concentrations as low as pg/g. Corresponding spatial resolution is dependent on the particular mass spec technique employed. The spatial resolution associated with mass spectrometry techniques is on the order of a few to hundreds of microns [100-102] and can get as low as 50 nm [100, 101, 103, 104]; however, smaller spatial resolution comes at the sacrifice of sensitivity.

Unfortunately, mass spectrometry can suffer from strong "matrix" (environmental) effects, and for some techniques, the matrix in which the ion is contained has been shown to vary the secondary ion yield by orders of magnitude [101]. Additionally, for some techniques, such as inductively coupled plasma mass spectrometry (ICP-MS) ionization is both element dependent and (to a much smaller extent) matrix dependent. As such, quantitation requires suitable reference materials [105].

I.4.2 MICROSCOPY COUPLED WITH METAL SPECIFIC FLUOROPHORES

Ideally speaking, an effective fluorophore will be specific only for its target metal and will have a high quantum yield and high molar absorptivity coefficient. As opposed to other methods herein, fluorescence microscopy has two key benefits. First, it can be used to study living organisms allowing time resolved *in vivo* investigations such as changes of metal concentrations as a function of time [91]. Second, confocal microscopy, due to the penetration depth of visible light, allows for 3-dimensional fluorescence measurements [106].

Unfortunately, quantitation of fluorescence is rarely straightforward. Even if one knows the binding kinetics that govern fluorophore metal binding, alternative binding of the analyte metal to proteins, nucleic acids, and various other small intracellular molecules are all competing kinetics that must be taken into account to calculate total cellular metal content. Because of this, the fluorophore-detected concentration represents the "free" or "loosely bound" cellular metal. Since free metal concentrations are known to be time dependent and variable [91], one must be sure that the fluorophore does not alter cellular homeostasis. As an example, a ten-fold change in fluorophore was shown to result in a two-fold increase in the calculated "free" metal concentration [107].

Fluorophores are not without complications. Photobleaching reactions involving the excited state are known to occur and cause most to stop fluorescing after some time. Even an ideal fluorophore, completely impervious to photobleaching, will still be constrained if it cannot be delivered to the appropriate cellular location. Multiple methods have been developed to get the fluorophores into the cells [108-111]; however, these can be difficult and time consuming.

I.4.3 X-RAY FLUORESCENCE

X-ray fluorescence imaging currently ranks as one of the most sensitive techniques for detecting trace elements in biological samples [95, 112-115]. In X-ray fluorescence spectroscopy, a material is bombarded with X-rays causing atoms to ionize and eject an inner core electron when the energy of the incoming X-ray exceeds the ionization potential of the atom. X-rays are used because they are sufficiently energetic to expel tightly held inner orbital electrons. The core-shell hole in the excited atom is subsequently filled as an electron from an outer shell relaxes to fill the gap. The falling electron emits a photon with energy equal to the energy difference between the two orbitals. The emitted photon's energy is characteristic of the atom and can be used to identify it. Taken together, the representative emission lines from each atom represent distinct "finger prints". Additionally, with appropriate calibration curves, the amount of metal can be calculated; this makes XRF both qualitative and quantitative.

There are multiple ways to excite a sample to emit x-rays [95, 96]; the two most common are particle induced excitation of x-ray emission (PIXE) and synchrotron x-ray fluorescence. Since the core of this thesis focuses on cytometry performed on living cells, the requirement of vacuum conditions for PIXE disqualifies it as a possible technique.

With the intense x-rays available at modern synchrotron x-ray sources, XRF can be used to determine the metal composition of individual cells. Although there are other techniques (such as those already mentioned) that can be used to determine metal composition, XRF is the only approach that can determine metal concentration independent of the chemical form of the metal and its surrounding environment. This is because the atomic transitions which give rise to XRF (e.g., the 2p → 1s transition in the case of Kα emission) are independent of local environment and oxidation state of the metal of interest. This nature of XRF is what makes it an ideal tool for interrogating the cellular metalome.

As such, XRF was chosen for this study because it benefits from three significant advantages compared to methods that use mass spectrometry and metals specific organic fluorophores: 1) XRF detects both bound and free metal ions in the cell whereas metal-specific fluorophores are only sensitive to the chelatable portion of metal ions in the cell; 2) is always detectable; and 3) equally detects both paramagnetic and diamagnetic trace elements. Although concentration detection limits for XRF are less than ICP-MS, the minimum required sample volume for XRF is quite small (less than 1 pL). This volume is much smaller than that typically required for ICP-MS (~1 mL); as such, XRF has very good mass detection limits.

I.5 CURRENT USE OF XRF FOR SINGLE CELL IMAGING STUDIES

XRF microscopy (XRM) is a well-defined technique that has been refined over more than half a century, since the pioneering days of Kirkpatrick and Baez [116, 117]. Spatial resolution on the order of microns is typical but can get as low as 30 nm depending on the optics. XRF studies relevant to this thesis encompass the 2D microscopy of XRF imaging. Classically, XRF imaging has used freeze dried cells. The preparation of freeze dried samples used in imaging is as follows: samples are put onto a silicon nitride window, allowed to settle for a short time period, and then blotted to remove the liquid. The wafer is then plunged into an organic cryogen. The cells freeze rapidly which should (ideally) preserve the structure. The frozen slide is then placed in a lyophilizer at a temperature below the freezing point of water. This removes residual water by sublimation and cell shrinkage. Based on past applications of XRF, a single XRF image (or projection) requires a sampling time on the order of greater than 1 hour [118].

Alternatively, imaging can be done using the Bionanoprobe (undulator beamline, Sector 21, Advanced Photon Source, Argonne National Lab, Lemont, Illinois, USA) [119], an x-ray fluorescence nanoprobe with a cryogenic sample environment and cryo transfer capabilities specifically designed for studying frozen, hydrated, biological samples. This probe affords the imaging of hydrated cells and therefore avoids structural deformation of cells due to collapse and cell shrinkage associated with freeze drying. This preserves the ultrastructure of cellular organelles.

I.6 FLOW CYTOMETRY

I.6.1 OVERVIEW OF FLOW CYTOMETRY

Like XRF, flow cytometry techniques are well established. Moldovan first used photoelectronics to count cells flowing through a capillary mounted on a microscope in 1934 [120]. Flow cytometry as a technique was significantly further advanced by Guker et al [121], whose device was used by the U.S. Army during WWII to detect airborne bacterial spores [93]. The 1970s saw application of flow cytometry to the study of mammalian cells [122, 123] with applications in the late 70s to microrganisms (*Escherichia coli, Rhizobium meliloti, and Rhizobium japonicum*) [124].

Generally, a solution containing cells is pumped through a tube and hydrodynamically focused by a faster moving sheath fluid. Samples are usually ejected onto a circular coverslip and then interrogated as they pass a specified zone. Detection usually uses light-scattering events or fluorescence [93]. These techniques are usually capable of interrogating thousands of cells per second.

Flow cytometry has also been paired with mass spectrometry [125]. For example, rare earth heavy metal isotope markers can be used to tag cells via antibodies. The cells are individually ionized using inductively coupled plasma and then analyzed with time-of-flight mass spectrometry. By combining different ratios of the isotopes, distinct tags can be used. This allows for multiparametric analysis.

I.6.2 THE XRF FLOW CYTOMETER

By combining XRF with flow cytometry it should be possible to investigate, *in vivo*, trace metal concentrations of individual aquated, respiring cells. Realization of an XRF flow cytometer for elemental analysis of single cells requires systematic, reproducible and reliable positioning of individual cells in an x-ray beam. In imaging studies, this is not an issue because cells are fixed in 3D space; however, with cells in solution where they are free to float around, this posed the initial problem. The second problem involves sample frequency.

In contrast to all other forms of flow cytometry, the XRF flow cytometer developed in this thesis required a slow sampling frequency because of the relatively low sensitivity of XRF. In order to maximize the number of cells detected, despite the low flow rate, we used a concentration that led to unavoidable overlap for some cells. Because of this, the XRF data absolutely must be paired with microscopy videos to track the cells and identify the location of the x-ray beam. As such, XRF flow cytometry is a combination spectroscopic-microscopic technique.

I.6.3 BETTER STATISTICS

The core goal of this thesis was to develop a technique capable of acquiring metal concentrations for a large sample size. An increased sample size provides for a better description of metal ion distribution (inside the cell in the case of imaging or among the population in the case of cytometry). This provides for greater certainty in measurements in addition to providing a better foundation for statistical analysis, and would provide direct information on the detail of the distribution.

Based on the work in this thesis, XRF studies may eventually no longer be limited to imaging. The microfluidic XRF flow cytometer developed in this thesis has the potential to become an additional technique applicable for the XRF detection of metals in cells. The flow cytometer provides *in vivo* single cell measurements with a frequency of ~1Hz. Although the flow cytometer only yields total metal content (it does not provide localization information) it is the only technique capable of using XRF to study the metallome in living actively respiring cells and has a sample turnover rate that makes possible the acquisition of population sized data sets (albeit, at a much slower rate than traditional flow cytometric techniques).

I.7 GENERAL OVERVIEW OF ORGANIZATION

This thesis focuses on the development of a novel analytical probe capable of performing X-ray flow cytometry experiments and the associated methodology and software required to analyze the associated data. Chapter II describes the first successful application of the new probe and Chapters III, IV, V & VI present the methodology of analysis, improvements to the probe, comparison of the fitting software to the dominant program currently used in the field, and the application of that fitting software to imaging data for freeze dried cells and hydrated, cryogenically frozen cells.

Chapter II discusses the development of an x-ray fluorescence flow cytometer that can determine the total metal concentration of single cells. The novel probe is capable of measuring population heterogeneity for metals in the µM to mM concentration range with fL cell volumes. The probe was used to determine the metal composition of over 800 individual bovine red blood cells and over 30 individual 3T3 mouse fibroblasts with an average measurement frequency of ~ 4 cells/minute. Details of the device design, data analysis, and options (both implemented and tentative) for further sensitivity improvement will be described. Patrick Kureka helped with all phases of instrument design and cell loading methodologies as well as data collection at APS. Aniruddha Deb provided project guidance. Jim Penner-Hahn provided project guidance and participated in data collection at APS. The staff of the LSA Scientific Instruments Shop provided valuable collaboration on sample older design.

Chapter III discusses the methodologies necessary to address four key research requirements for analyzing XRF flow cytometry data: instrument calibration, signal calibration, signal identification, and signal quantification. Because the analysis of XRF flow cytometry data absolutely requires video data, the second portion of this chapter will discuss the additional treatment of the video data and the new methodologies developed to combine the two data sets from XRF and video. Aniruddha Deb provided project guidance. Jim Penner-Hahn provided invaluable collaboration towards the developed methodologies.

Chapter IV discusses improvements made to the flow cytometer. These improvements include the addition of a second horizontal microscope, an increase in the solid angle that is measured and a decrease in the background. It addresses the effect of the horizontal beam profile on the observed population distributions of elemental masses obtained from biological samples using the cytometer. Additionally, the use of a He shroud to reduce scatter is discussed and preliminary results are presented that indicate the potential of future improvements. The staff of the LSA Scientific Instruments Shop provided valuable collaboration on the redesign of the sample older design. Aniruddha Deb provided project guidance. Jim Penner-Hahn provided invaluable collaboration towards the developed methodologies. Tsz Kwan Yim and Claire Kozemchek both participated in capillary experiments and with data collection at APS.

Chapter V extends M-BLANK, the software developed for the fitting of time-course x-ray fluorescence flow cytometry data, to the fitting of imaging data. The quality of these fits is compared with the quality obtained from MAPS, the dominant program currently used in the field of x-ray fluorescence microscopy.

Chapter VI discusses the application of M-BLANK to the imaging of mouse fibroblasts (NIH3T3). This chapter extends from previous XRF imaging studies on the effect of Cd on metal homeostasis in yeast. Previous studies, from 2010, using this cell line showed significant Cu contamination and completely vacated nuclei. In order to test these results, the studies presented in this chapter were undertaken on mouse fibroblasts cells, cryogenically encased in ice and analyzed at the bionanoprobe. Lubomir Dostal is the lead of this project. I was present at data collection and performed the fitting and analysis.

I.8 REFERENCES

1. Askwith, C. and J. Kaplan, *Iron and copper transport in yeast and its relevanace to human disease.* Trends in Biochemical Sciences, 1998. **23**(4): p. 135-138.
2. Draper, D.E., D. Grilley, and A.M. Soto, *Ions and RNA folding*, in *Annual Review of Biophysics and Biomolecular Structure*. 2005. p. 221-243.
3. Misra, V.K., R. Shiman, and D.E. Draper, *A thermodynamic framework for the magnesium-dependent folding of RNA.* Biopolymers, 2003. **69**(1): p. 118-136.
4. Sigel, R.K.O. and A.M. Pyle, *Alternative roles for metal ions in enzyme catalysis and the implications for ribozyme chemistry.* Chemical Reviews, 2007. **107**(1): p. 97-113.
5. Dambach, M.D. and W.C. Winkler, *Expanding roles for metabolite-sensing regulatory RNAs.* Current Opinion in Microbiology, 2009. **12**(2): p. 161-169.
6. Draper, D.E., *A guide to ions and RNA structure.* Rna-a Publication of the Rna Society, 2004. **10**(3): p. 335-343.
7. Edwards, T.E., D.J. Klein, and A.R. Ferre-D'Amare, *Riboswitches: small-molecule recognition by gene regulatory RNAs.* Current Opinion in Structural Biology, 2007. **17**(3): p. 273-279.
8. Klein, D.J., T.E. Edwards, and A.R. Ferre-D'Amare, *Cocrystal structure of a class I preQ(1) riboswitch reveals a pseudoknot recognizing an essential hypermodified nucleobase.* Nature Structural & Molecular Biology, 2009. **16**(3): p. 343-344.
9. Klein, D.J., P.B. Moore, and T.A. Steitz, *The contribution of metal ions to the structural stability of the large ribosomal subunit.* Rna-a Publication of the Rna Society, 2004. **10**(9): p. 1366-1379.
10. Edwards, T.E. and A.R. Ferre-D'Amare, *Crystal structures of the thi-box riboswitch bound to thiamine pyrophosphate analogs reveal adaptive RNA-small molecule recognition.* Structure, 2006. **14**(9): p. 1459-1468.
11. Serganov, A., et al., *Structural basis for gene regulation by a thiamine pyrophosphate-sensing riboswitch.* Nature, 2006. **441**(7097): p. 1167-1171.
12. Thore, S., C. Frick, and N. Ban, *Structural basis of thiamine pyrophosphate analogues binding to the eukaryotic riboswitch.* Journal of the American Chemical Society, 2008. **130**(26): p. 8116-+.
13. Cochrane, J.C., S.V. Lipchock, and S.A. Strobel, *Structural investigation of the GlmS ribozyme bound to its catalytic cofactor.* Chemistry & Biology, 2007. **14**(1): p. 97-105.
14. Klein, D.J., et al., *Requirement of helix p2.2 and nucleotide g1 for positioning the cleavage site and cofactor of the glmS ribozyme.* Journal of Molecular Biology, 2007. **373**(1): p. 178-189.
15. Baird, N.J. and A.R. Ferre-D'Amare, *Idiosyncratically tuned switching behavior of riboswitch aptamer domains revealed by comparative small-angle X-ray scattering analysis.* Rna-a Publication of the Rna Society, 2010. **16**(3): p. 598-609.
16. Basu, S., et al., *A specific monovalent metal ion integral to the AA platform of the RNA tetraloop receptor.* Nature Structural Biology, 1998. **5**(11): p. 986-992.
17. Garst, A.D., et al., *Crystal structure of the lysine riboswitch regulatory mRNA element.* Journal of Biological Chemistry, 2008. **283**(33): p. 22347-22351.
18. Serganov, A., L.L. Huang, and D.J. Patel, *Structural insights into amino acid binding and gene control by a lysine riboswitch.* Nature, 2008. **455**(7217): p. 1263-U76.
19. Dann, C.E., et al., *Structure and mechanism of a metal-sensing regulatory RNA.* Cell, 2007. **130**(5): p. 878-892.
20. Groisman, E.A., et al., *A Mg2+-responding RNA that controls the expression of a Mg2+ transporter.* Cold Spring Harbor Symposia on Quantitative Biology, 2006. **71**: p. 251-258.
21. Jomova, K. and M. Valko, *Advances in metal-induced oxidative stress and human disease.* Toxicology, 2011. **283**(2-3): p. 65-87.

22. Valko, M., et al., *Free radicals and antioxidants in normal physiological functions and human disease.* International Journal of Biochemistry & Cell Biology, 2007. **39**(1): p. 44-84.
23. Valko, M., et al., *Free radicals, metals and antioxidants in oxidative stress-induced cancer.* Chemico-Biological Interactions, 2006. **160**(1): p. 1-40.
24. Klaunig, J.E., et al., *Oxidative stress and oxidative damage in chemical carcinogenesis.* Toxicology and Applied Pharmacology, 2011. **254**(2): p. 86-99.
25. Salnikow, K., et al., *Depletion of intracellular ascorbate by the carcinogenic metals nickel and cobalt results in the induction of hypoxic stress.* Journal of Biological Chemistry, 2004. **279**(39): p. 40337-40344.
26. Baldwin, E.L., J.A.W. Byl, and N. Osheroff, *Cobalt enhances DNA cleavage mediated by human topoisomerase II alpha in vitro and in cultured cells.* Biochemistry, 2004. **43**(3): p. 728-735.
27. Calderon-Garciduenas, L., et al., *The impact of environmental metals in young urbanites' brains.* Experimental and Toxicologic Pathology, 2013. **65**(5): p. 503-511.
28. Thorgersen, M.P. and D.M. Downs, *Cobalt targets multiple metabolic processes in Salmonella entefica.* Journal of Bacteriology, 2007. **189**(21): p. 7774-7781.
29. Desai, N., et al., *Free Radical Theory of Aging: Implications in Male Infertility.* Urology, 2010. **75**(1): p. 14-19.
30. Malins, D.C., et al., *Cancer-related changes in prostate DNA as men age and early identification of metastasis in primary prostate tumors.* Proceedings of the National Academy of Sciences of the United States of America, 2003. **100**(9): p. 5401-5406.
31. Hakim, M., et al., *Volatile Organic Compounds of Lung Cancer and Possible Biochemical Pathways.* Chemical Reviews, 2012. **112**(11): p. 5949-5966.
32. Luijsterburg, M.S. and H. van Attikum, *Chromatin and the DNA damage response: The cancer connection.* Molecular Oncology, 2011. **5**(4): p. 349-367.
33. Yaman, M., et al., *Comparison of trace metal concentrations in malign and benign human prostate.* Journal of Medicinal Chemistry, 2005. **48**(2): p. 630-634.
34. Ziech, D., et al., *The role of reactive oxygen species and oxidative stress in environmental carcinogenesis and biomarker development.* Chemico-Biological Interactions, 2010. **188**(2): p. 334-339.
35. Chen, J., et al., *Iron Accumulates in Huntington's Disease Neurons: Protection by Deferoxamine.* Plos One, 2013. **8**(10).
36. Rosas, H.D., et al., *Alterations in Brain Transition Metals in Huntington Disease An Evolving and Intricate Story.* Archives of Neurology, 2012. **69**(7): p. 887-893.
37. Benedetto, A., C. Au, and M. Aschner, *Manganese-induced Dopaminergic Neurodegeneration: Insights into Mechanisms and Genetics Shared with Parkinson's Disease.* Chemical Reviews, 2009. **109**(10): p. 4862-4884.
38. Eskici, G. and P.H. Axelsen, *Copper and Oxidative Stress in the Pathogenesis of Alzheimer's Disease.* Biochemistry, 2012. **51**(32): p. 6289-6311.
39. Geier, D.A. and M.R. Geier, *An autism cohort study of cobalt levels following vitamin B12 injections.* Toxicological and Environmental Chemistry, 2010. **92**(5): p. 1025-1037.
40. Tunez, I., et al., *Important Role of Oxidative Stress Biomarkers in Huntington's Disease.* Journal of Medicinal Chemistry, 2011. **54**(15): p. 5602-5606.
41. Ide, T., et al., *Mitochondrial DNA damage and dysfunction associated with oxidative stress in failing hearts after myocardial infarction.* Circulation Research, 2001. **88**(5): p. 529-535.
42. Stadler, N., R.A. Lindner, and M.J. Davies, *Direct detection and quantification of transition metal ions in human atherosclerotic plaques: Evidence for the presence of elevated levels of iron and copper.* Arteriosclerosis Thrombosis and Vascular Biology, 2004. **24**(5): p. 949-954.

43. Salnikow, K. and A. Zhitkovich, *Genetic and epigenetic mechanisms in metal carcinogenesis and cocarcinogenesis: Nickel, arsenic, and chromium.* Chemical Research in Toxicology, 2008. **21**(1): p. 28-44.
44. Hua, Y., et al., *Molecular mechanisms of chromium in alleviating insulin resistance.* Journal of Nutritional Biochemistry, 2012. **23**(4): p. 313-319.
45. Lee, D.H., et al., *Common presence of non-transferrin-bound iron among patients with type 2 diabetes.* Diabetes Care, 2006. **29**(5): p. 1090-1095.
46. Bush, A.I. and C.C. Curtain, *Twenty years of metallo-neurobiology: where to now?* European Biophysics Journal with Biophysics Letters, 2008. **37**(3): p. 241-245.
47. Rajendran, R., et al., *A novel approach to the identification and quantitative elemental analysis of amyloid deposits-Insights into the pathology of Alzheimer's disease.* Biochemical and Biophysical Research Communications, 2009. **382**(1): p. 91-95.
48. Gupte, A. and R.J. Mumper, *Elevated copper and oxidative stress in cancer cells as a target for cancer treatment.* Cancer Treatment Reviews, 2009. **35**(1): p. 32-46.
49. Malins, D.C., *Free radicals and breast cancer.* Environmental Health Perspectives, 1996. **104**(11): p. 1140-1140.
50. Zahler, N.H., et al., *X-ray Fluorescence Imaging Reveals Cadmium Toxicity is Linked to Altered Copper Homeostasis in Yeast*. University of Michigan: Ann Arbor.
51. Kamizono, A., et al., *Identification of a Gene Conferring Resistance to Zinc and Cadmium Ions in the Yeast Saccharomyces cerevisiae.* Molecular & General Genetics, 1989. **219**(1-2): p. 161-167.
52. Vicentefranqueira, R., et al., *The zrfA and zrfB genes of Aspergillus fumigatus encode the zinc transporter proteins of a zinc uptake system induced in an acid, zinc-depleted environment.* Eukaryotic Cell, 2005. **4**(5): p. 837-848.
53. Li, L.T. and J. Kaplan, *Defects in the yeast high affinity iron transport system result in increased metal sensitivity because of the increased expression of transporters with a broad transition metal specificity.* Journal of Biological Chemistry, 1998. **273**(35): p. 22181-22187.
54. Pagani, M.A., et al., *Disruption of iron homeostasis in Saccharomyces cerevisiae by high zinc levels: a genome-wide study.* Molecular Microbiology, 2007. **65**(2): p. 521-537.
55. Griffith, D.P., et al., *Acquired Copper Deficiency: A Potentially Serious and Preventable Complication Following Gastric Bypass Surgery.* Obesity, 2009. **17**(4): p. 827-831.
56. Fujioka, K., *Follow-up of nutritional and metabolic problems after bariatric surgery.* Diabetes Care, 2005. **28**(2): p. 481-484.
57. Kumar, N., J.E. Ahlskog, and J.B. Gross, *Acquired Hypocupremia After Gastric Surgery.* Clinical Gastroenterology and Hepatology, 2004. **2**(12): p. 1074-1079.
58. Steinbrook, R., *Surgery for severe obesity.* New England Journal of Medicine, 2004. **350**(11): p. 1075-1079.
59. Tan, J.C., D.L. Burns, and H.R. Jones, *Severe ataxia, myelopathy, and peripheral neuropathy due to acquired copper deficiency in a patient with history of gastrectomy.* Journal of Parenteral and Enteral Nutrition, 2006. **30**(5): p. 446-450.
60. Madsen, E. and J.D. Gitlin, *Copper and Iron Disorders of the Brain.* Annu. Rev. Neurosci., 2007. **30**: p. 317-337.
61. Dlouhy, A.C. and C.E. Outten, *The Iron Metallome in Eukaryotic Organisms*, in *Metallomics and the Cell*, L. Banci, Editor. 2013, Springer: Dordrecht. p. 241-278.
62. Eide, D.J., *Homeostatic and Adaptive Responses to Zinc Deficiency in Saccaromyces cerevisiae.* J. Biol Chem, 2009. **284**(28): p. 18565-18569.
63. Simm, C., et al., *Saccharomyces cerevisiae Vacuole in Zinc Storage and Intracellular Zinc Distribution.* Eukaryotic Cell, 2007. **6**(7): p. 1166-1177.

64. Lyons, T.J., et al., *Genome-wide characterization of the Zap1p zinc-responsive regulon in yeast.* PNAS, 2000. **97**(14): p. 7957-7962.
65. Bird, A.J., et al., *A dual role for zinc fingers in both DNA binding and zinc sensing by the Zap1 transcriptional activator.* Embo Journal, 2000. **19**(14): p. 3704-3713.
66. Yuan, D.S., *Zinc-regulated genes in Saccharomyces cerevisiae revealed by transposon tagging.* Genetics, 2000. **156**(1): p. 45-58.
67. Wu, C.-Y., et al., *Differential control of Zapl-regulated genes in response to zinc deficiency in Saccharomyces cerevisiae.* Bmc Genomics, 2008. **9**.
68. Higgins, V.J., P.J. Rogers, and I.W. Dawes, *Application of genome-wide expression analysis to identify molecular markers useful in monitoring industrial fermentations.* Applied and Environmental Microbiology, 2003. **69**(12): p. 7535-7540.
69. De Nicola, R., et al., *Physiological and transcriptional responses of Saccharomyces cereviside to zinc limitation in chemostat cultures.* Applied and Environmental Microbiology, 2007. **73**(23): p. 7680-7692.
70. Wu, C.-Y., et al., *Regulation of the yeast TSA1 peroxiredoxin by ZAP1 is an adaptive response to the oxidative stress of zinc deficiency.* Journal of Biological Chemistry, 2007. **282**(4): p. 2184-2195.
71. Zhao, H., et al., *Regulation of zinc homeostasis in yeast by binding of the ZAP1 transcriptional activator to zinc-responsive promoter elements.* Journal of Biological Chemistry, 1998. **273**(44): p. 28713-28720.
72. Zhao, H. and D. Eide, *The yeast ZRT1 gene encodes the zinc transporter protein of a high-affinity uptake system induced by zinc limitation.* Proceedings of the National Academy of Sciences of the United States of America, 1996. **93**(6): p. 2454-2458.
73. Zhao, H. and D. Eide, *The ZRT2 gene encodes the low affinity zinc transporter in Saccharomyces cerevisiae.* Journal of Biological Chemistry, 1996. **271**(38): p. 23203-23210.
74. Waters, B.M. and D.J. Eide, *Combinatorial control of yeast FET4 gene expression by iron, zinc, and oxygen.* Journal of Biological Chemistry, 2002. **277**(37): p. 33749-33757.
75. MacDiarmid, C.W., L.A. Gaither, and D. Eide, *Zinc transporters that regulate vacuolar zinc storage in Saccharomyces cerevisiae.* Embo Journal, 2000. **19**(12): p. 2845-2855.
76. MacDiarmid, C.W., M.A. Milanick, and D.J. Eide, *Induction of the ZRC1 metal tolerance gene in zinc-limited yeast confers resistance to zinc shock.* Journal of Biological Chemistry, 2003. **278**(17): p. 15065-15072.
77. Miyabe, S., S. Izawa, and Y. Inoue, *Expression of ZRC1 coding for suppressor of zinc toxicity is induced by zinc-starvation stress in Zap1-dependent fashion in Saccharomyces cerevisiae.* Biochemical and Biophysical Research Communications, 2000. **276**(3): p. 879-884.
78. Wu, Y.-H., A.G. Frey, and D.J. Eide, *Transcriptional regulation of the Zrg17 zinc transporter of the yeast secretory pathway.* Biochemical Journal, 2011. **435**: p. 259-266.
79. Bird, A.J., et al., *Repression of ADH1 and ADH3 during zinc deficiency by Zap1-induced intergenic RNA transcripts.* Embo Journal, 2006. **25**(24): p. 5726-5734.
80. Drewke, C. and M. Ciriacy, *OVEREXPRESSION, PURIFICATION AND PROPERTIES OF ALCOHOL DEHYDROGENASE-IV FROM SACCHAROMYCES-CEREVISIAE.* Biochimica Et Biophysica Acta, 1988. **950**(1): p. 54-60.
81. Kaiser, P., et al., *The yeast ubiquitin ligase SCFMet30: connecting environmental and intracellular conditions to cell division.* Cell Division, 2006. **1**.
82. Thomas, D. and Y. SurdinKerjan, *Metabolism of sulfur amino acids in Saccharomyces cerevisiae.* Microbiology and Molecular Biology Reviews, 1997. **61**(4): p. 503-&.

83. Carman, G.M. and G.S. Han, *Regulation of phospholipid synthesis in Saccharomyces cerevisiae by zinc depletion.* Biochimica Et Biophysica Acta-Molecular and Cell Biology of Lipids, 2007. **1771**(3): p. 322-330.
84. Iwanyshyn, W.M., G.S. Han, and G.M. Carman, *Regulation of phospholipid synthesis in Saccharomyces cerevisiae by zinc.* Journal of Biological Chemistry, 2004. **279**(21): p. 21976-21983.
85. Ellis, C.D., C.W. MacDiarmid, and D.J. Eide, *Heteromeric protein complexes mediate zinc transport into the secretory pathway of eukaryotic cells.* Journal of Biological Chemistry, 2005. **280**(31): p. 28811-28818.
86. Ellis, C.D., et al., *Zinc and the Msc2 zinc transporter protein are required for endoplasmic reticulum function.* Journal of Cell Biology, 2004. **166**(3): p. 325-335.
87. Davey, H.M. and D.B. Kell, *Flow Cytometry and Cell Sorting of Hterogeneous Microbial Populations: The Importance of Single-Cell Analyses.* Microbiological Reviews, 1996. **60**(4): p. 641-696.
88. Kalisky, T. and S.R. Quake, *Single-cell genomics.* Nature Methods, 2011. **8**(4): p. 311-314.
89. Musat, N., et al., *A single-cell view on the ecophysiology of anaerobic phototrophic bacteria.* Proceedings of the National Academy of Sciences of the United States of America, 2008. **105**(46): p. 17861-17866.
90. Leslie, M., *The Power Of One*, in *Science*. 2011. p. 24-26.
91. Wang, D., O. Hosteen, and C.A. Fierke, *ZntR-mediated transcription of zntA responds to nanomolar intracellular free zinc.* Journal of Inorganic Biochemistry, 2012. **111**: p. 173-181.
92. Eide, D.J., *Homeostatic and Adaptive Responses to Zinc Deficiency in Saccharomyces cerevisiae.* Journal of Biological Chemistry, 2009. **284**(28): p. 18565-18569.
93. Davey, H.M. and D.B. Kell, *Flow Cytometry and Cell Sorting of Heterogeneous Microbial Populations: The Importance of Single-Cell Analyses.* Microbiological Reviews, 1996. **60**(4): p. 641-696.
94. Brehm-Stecher, B.F. and E.A. Johnson, *Single-Cell Microbiology: Tools, Technologies, and Applications.* Microbiology and Molecular Biology Reviews, 2004. **68**(3): p. 538-559.
95. McRae, R., et al., *In Situ Imaging of Metals in Cells and Tissues.* Chemical Reviews, 2009. **109**(10): p. 4780-4827.
96. Penner-Hahn, J.E., *Metal Ions in Life Sciences*. 2013, Springer Science+Business Media Dordrecht.
97. Zhao, F.J., et al., *Imaging element distribution and speciation in plant cells.* Trends in Plant Science, 2014. **19**(3): p. 183-192.
98. Kaufmann, R., C. Hagen, and K. Grunewald, *Fluorescence cryo-microscopy: current challenges and prospects.* Current Opinion in Chemical Biology, 2014. **20**: p. 86-91.
99. Nemes, P. and A. Vertes, *Ambient mass spectrometry for in vivo local analysis and in situ molecular tissue imaging.* Trac-Trends in Analytical Chemistry, 2012. **34**: p. 22-34.
100. Hammond, J.S., *Comparison of SIMS and MALDI for Mass Spectrometric Imaging*. Imaging Mass Spectrometry: Protocols for Mass Microscopy, ed. M. Setou. 2010. 235-257.
101. Wu, B. and J.S. Becker, *Imaging of elements and molecules in biological tissues and cells in the low-micrometer and nanometer range.* International Journal of Mass Spectrometry, 2011. **307**(1-3): p. 112-122.
102. Qin, Z.Y., et al., *Trace metal imaging with high spatial resolution: Applications in biomedicine.* Metallomics, 2011. **3**(1): p. 28-37.
103. Boxer, S.G., M.L. Kraft, and P.K. Weber, *Advances in Imaging Secondary Ion Mass Spectrometry for Biological Samples*, in *Annual Review of Biophysics*. 2009. p. 53-74.

104. Zimmerman, T.A., et al., *Imaging of Cells and Tissues with Mass Spectrometry: Adding Chemical Information to Imaging*, in *Biophysical Tools for Biologists, Vol 2: In Vivo Techniques*, J.J. Correia and H.W. Detrich, Editors. 2008. p. 361-+.
105. Becker, J.S., et al., *Mass spectrometric imaging (MSI) of metals using advanced BrainMet techniques for biomedical research.* International Journal of Mass Spectrometry, 2011. **307**(1-3): p. 3-15.
106. O'Malley, D., *Imaging in Depth: Controversies and Opportunities*, in *Biophysical Tools for Biologists, Vol 2: In Vivo Techniques*, J.J. Correia and H.W. Detrich, Editors. 2008. p. 95-+.
107. Krezel, A. and W. Maret, *Zinc-buffering capacity of a eukaryotic cell at physiological pZn.* Journal of Biological Inorganic Chemistry, 2006. **11**(8): p. 1049-1062.
108. Fierke, C.A. and R.B. Thompson, *Fluorescence-based biosensing of zinc using carbonic anhydrase.* Biometals, 2001. **14**(3-4): p. 205-222.
109. Tsien, R.Y., *A NON-DISRUPTIVE TECHNIQUE FOR LOADING CALCIUM BUFFERS AND INDICATORS INTO CELLS.* Nature, 1981. **290**(5806): p. 527-528.
110. Van Dongen, E., et al., *Ratiometric fluorescent sensor proteins with subnanomolar affinity for Zn(II) based on copper chaperone domains.* Journal of the American Chemical Society, 2006. **128**(33): p. 10754-10762.
111. Wang, D., et al., *Genetically encoded ratiometric biosensors to measure intracellular exchangeable zinc in Escherichia coil.* Journal of Biomedical Optics, 2011. **16**(8).
112. Fahrni, C.J., *Biological applications of X-ray fluorescence microscopy: exploring the subcellular topography and speciation of transition metals.* Current Opinion in Chemical Biology, 2007. **11**(2): p. 121-127.
113. Paunesku, T., et al., *X-ray fluorescence microprobe imaging in biology and medicine.* Journal of Cellular Biochemistry, 2006. **99**(6): p. 1489-1502.
114. Paunesku, T., et al., *X-RAY FLUORESCENCE MICROSCOPY FOR INVESTIGATION OF ARCHIVAL TISSUES.* Health Physics, 2012. **103**(2): p. 181-186.
115. Vogt, S., et al., *Imaging trace elements in cells with x-ray fluorescence microscopy.* Microscopy and Microanalysis, 2007. **13**: p. 40-41.
116. Baez, A.V., *FRESNEL ZONE PLATE FOR OPTICAL IMAGE FORMATION USING EXTREME ULTRAVIOLET AND SOFT X RADIATION.* Journal of the Optical Society of America, 1961. **51**(4): p. 405-&.
117. Kirkpatrick, P. and A.V. Baez, *FORMATION OF OPTICAL IMAGES BY X-RAYS.* Journal of the Optical Society of America, 1948. **38**(9): p. 766-774.
118. Bourassa, D., et al., *3D imaging of transition metals in the zebrafish embryo by X-ray fluorescence microtomography.* Metallomics, 2014. **6**(9): p. 1648-1655.
119. Chen, S., et al., *The Bionanoprobe: hard X-ray fluorescence nanoprobe with cryogenic capabilities.* Journal of Synchrotron Radiation, 2014. **21**: p. 66-75.
120. Moldovan, A., *Photo-electric Technique for for the counting of microscopical cells.* Science, 1934. **80**(2069): p. 188-189.
121. Gucker, F.T., et al., *A Photoelectronic Counter for Colloidal Particles.* Journal of the American Chemical Society, 1947. **69**(10): p. 2422-2431.
122. Barlogie, B., et al., *DNA HISTOGRAM ANALYSIS OF HUMAN HEMATOPOIETIC CELLS.* Blood, 1976. **48**(2): p. 245-258.
123. Crissman, H.A., et al., *DETAILED STUDIES ON THE APPLICATION OF 3 FLUORESCENT ANTIBIOTICS FOR DNA STAINING IN FLOW CYTOMETRY.* Stain Technology, 1978. **53**(6): p. 321-330.
124. Pauu, A.S., J.R. Cowles, and J. Oro, *Flow-microfluorometric analysis of Escherichia coli, Rhizobium meliloti, and Rhizobium japonicum at different stages of the growth cycle.* Can. J. Microbiol., 1977. **23**: p. 1165-1169.

125. Ornatsky, O., et al., *Highly multiparametric analysis by mass cytometry.* Journal of Immunological Methods, 2010. **361**(1-2): p. 1-20.

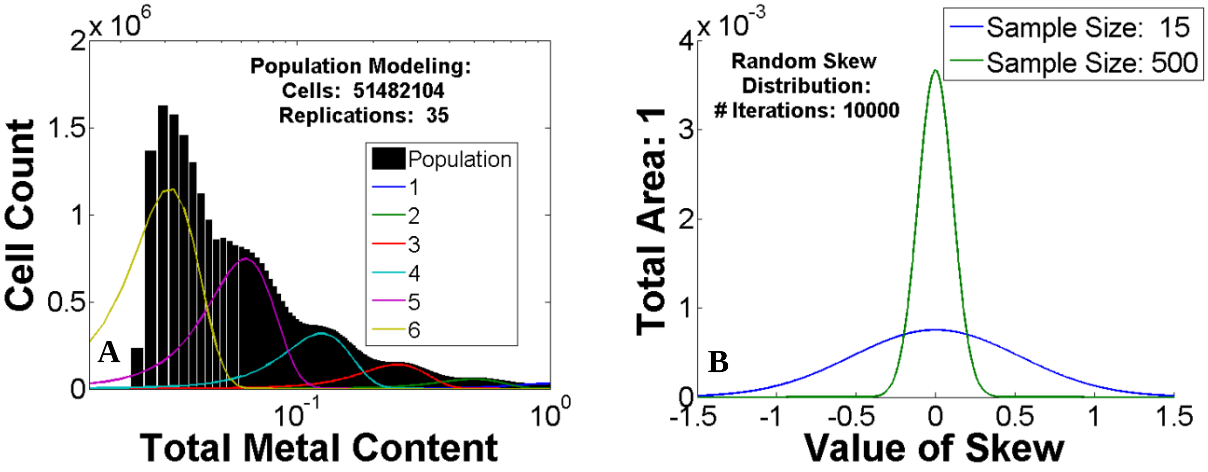

Figure I.1 Modeling Populations and Skews: (A) The modeled population distribution starting with a single cell and then allowing for 35 rounds of replication. The modeled replication included gated transcriptional activation and deactivation of cellular metal ion uptake using upper and lower thresholds. The x-axis is logarithmic. There were six allowed replication events between gated thresholds. This corresponded to an upper threshold and lower threshold that differed by 2^6, or 128-fold. (B) The distribution of apparent skews based on randomly generated sample sizes of 15 and 500 data points taken randomly from a symmetric distribution. After each sample was generated, the skew from that sample was calculated. This was performed 10,000 times and the resulting skews for the two sample sizes were plotted as histograms and the histograms were fit to the two Gaussian distributions depicted here. For a sample size of 500, a calculated skew of ±0.5 would be significantly different from zero ($p = 0.001$); for a sample size of 15 a skew does not become statistically significant from zero ($p = 0.001$) until a value of ± 1.5.

CHAPTER II: DEVELOPMENT OF A SINGLE-CELL X-RAY FLUORESCENCE FLOW CYTOMETER[1]

II.1 INTRODUCTION

In addition to their organic constituents, cells contain a variety of bulk, trace and ultra-trace elements. In most cases, cells appear to have homeostatic mechanisms that maintain elemental concentrations within narrow limits. Knowledge of these cellular concentrations under different conditions is important for understanding homeostasis. Relevant concentrations range from ~10 – 100 mM for bulk elements (P, K, Na, Fe, in red blood cells) to 0.1 – 3 mM for trace elements (Zn, Mg, Ca, Fe in other cell types) to 1 – 20 µM for ultratrace elements (Cu, Ni, Mn, Se) [1, 2]. These concentrations are perturbed under various conditions and disease states [3, 4], and these variations can be clinically diagnostic for disease states [4].

Cellular uptake of toxic metals can also result in disruption of metal concentrations. For example, Zahler *et al.* combined x-ray fluorescence (XRF) imaging and bulk sample analysis to demonstrate that cadmium toxicity in *Saccharomyces cerevisiae* is correlated to altered copper homeostasis and increased levels of zinc and iron [5]. In line with this, cadmium has been found

---

[1] Patrick Kureka helped with all phases of instrument design and cell loading methodologies as well as data collection at APS. Aniruddha Deb provided project guidance. Jim Penner-Hahn provided project guidance and participated in data collection at APS. The staff of the LSA Scientific Instruments Shop provided valuable collaboration on sample holder design. This research was supported by NSF IDBR-0852802. This research used resources of the Advanced Photon Source, a U.S. Department of Energy (DOE) Office of Science User Facility operated for the DOE Office of Science by Argonne National Laboratory under Contract No. DE-AC02-06CH11357. This project was supported by grant 9 P41 GM103622 from the National Institute of General Medical Sciences of the National Institutes of Health. The content is solely the responsibility of the author and does not necessarily reflect the official views of the National Institute of General Medical Sciences or the National Institutes of Health.

to biologically mimic the substrate binding of zinc [6], and cadmium has been shown to exert transcriptional influence over the expression of Zn transporters [7]. Additionally, increases in intracellular Zn have been attributed in *S. cerevisiae* to increased expression of Fet4, which transports Cu, Fe, and Zn [8, 9]. Likewise, dietary or genetic disruption of metal ion homeostasis causes many disease states, particularly copper and iron [10, 11].

The dynamic regulatory processes involved in homeostasis can lead to significant heterogeneity in elemental concentrations [12-14]. Therefore, a complete characterization of homeostasis requires knowing not only the mean concentration of an element for a sample, but also the cell-to-cell variability in concentrations. In comparison to single cell measurements, bulk-scale measurements fail to capture discrete properties of a population. There have been very few single cell studies of elemental composition. There are several methods that have sufficient sensitivity to give single cell elemental compositions. These include mass spectrometry (MS), metal specific organic fluorophores, and intrinsic (x-ray) fluorescence. Fluorescent probes have been used to report on subcellular transition metal cations such as zinc [15] or copper [16] and can have excellent sensitivity. However, these are generally less useful for paramagnetic ions, and even for diamagnetic metals, fluorescent probes are limited to detecting only the chelatable metal in the cell. Mass spectrometric methods can have exquisite sensitivity and multielement detection capability. However, MS methods can suffer from matrix effects and haven't been widely used for single cell studies. In contrast, XRF is always detectable, has minimal matrix effects, and detects both bound and free metal ions in the cell.

In this paper, we describe the development and testing of an XRF-based flow cytometer that permits detection of total trace element levels in aquated living cells at high throughput.

II.2 EXPERIMENTAL

II.2.1 SAMPLE PREPARATION, HANDLING AND ANALYSIS

Samples were prepared/acquired ahead of our experimental time and then transported for analysis.

II.2.2 SAMPLE PREPARATION AND HANDLING

Red blood cell experiments were performed using trypsinized bovine red blood cells (bRBCs, 0.1 hematocrit, obtained from Lampire), diluted 1:30 using phosphate buffered saline (PBS – obtained from Fisher Scientific). When not used, the stock and the diluted aliquots were kept at 4˚C. NIH3T3 experiments were done using cells grown from cryopreserved aliquots in atmospheric O_2 and 5% CO_2 at 37°C. Cells were thawed and placed in 12 ml of complete medium (CM) [Dulbecco's modified Eagle medium (DMEM), high glucose variant (4.5 mg ml–1), supplemented with 10%donor bovine in 75 cm^2 flasks at 5 x 10^5 cells flask^{-1} (6.7 x 10^3 cells cm^{-2}). The cells were fed on day 2 (75% replacement) and then subcultured on day 5 into six 75 cm^2 flasks at 5.5 x 10^5 cells flask^{-1}. After 2 days of further proliferation, the cells were subcultured into twelve 75 cm^2 flasks at 5.5 x 10^5 cells flask^{-1}. The next day CM medium in flasks was increased from 12 ml to 200 ml. This CM medium increase promotes cell survival outside incubator at room temperature and atmospheric CO_2 levels for about a week. Cells were transported to APS and kept at room temperature and atmospheric CO_2 for 3-5 days. Cells were then harvested and resuspended in phosphate buffered saline (PBS) solution for measurement of metal concentration.

II.2.3 SAMPLE ANALYSIS

Samples were contained in acrylic (polymethylmethacrylate) capillaries (50 µm i.d., 100 µm o.d.) and were loaded using capillary action. The velocities of the cells were measured to be on the order of ~1 mm s^{-1} and a 20 cm capillary takes ~10 minutes to fill. Based on this, capillary action was used to load the sample capillary. The addition of a curve at the top of the capillary higher than the terminal end allowed for an air pocket to be trapped when a droplet was placed over the terminal end of the capillary, sealing it. This caused a dramatic decrease of cellular velocity (from ~ 500 µm s^{-1} to ~ 5 µm s^{-1}). As the droplet slowly evaporated, the air pocket was allowed to rise. This resulted in the cells climbing farther up the capillary as illustrated in **Figure II.1**. Each position of the capillary was scanned for 10 minutes, while the full 2048 channel XRF signal was captured at 4 Hz. A typical scan detected between 20 – 60 cells depending on the cell density. After each scan, the capillary was translated by 100 µm vertically to avoid excessive radiation damage to the capillary.

XRF spectra were collected using an energy resolving solid state detector (Vortex-ME4, SII NanoTechnology) and fluorescence counts were normalized to the incident intensity measured with a N_2 filled ion chamber immediately upstream from the sample. The distance between the detector elements and the center of the capillary was ~2.5 cm. The x-ray beam was focused to 50 µm horizontal x 20 µm vertical using a pair of Kirkpatrick-Baez mirrors[17], with the precise beam profile determined by a knife edge scan.

II.2.4 INSTRUMENT CALIBRATION

The instrument was calibrated using standard solutions (~100, ~200, and ~500 µM $Cr(NO_3)_3$, $Fe(NO_3)_3$, $Ni(NO_3)_2$, and $Zn(NO_3)_2$ in water at low pH to ensure solubility). Where most x-ray fluorescence analyses at synchrotron sources rely on single point calibrations, we have used three different concentrations for each element. These concentrations were confirmed by ICP-OES (Perkin-Elmer Optima 2000 DV with Winlab software) pre- and post-experiment. Although Zn was present in the standard solutions, there was no Zn ICP-EOS standard with which to perform mass quantitation of our XRF standards. Therefore, we were unable to include Zn in Figure 2. Additionally, the amounts of Ni, Cr, and Fe in each sample were found to be considerably different. This is demonstrated most notably by the point for Ni at ~2,500 fg relative the amount of Fe and Cr in the highest concentrated sample where both were ~1,000 fg.

Prior to collecting XRF data for each standard, a blank scan of each capillary was obtained. The standard solutions were then loaded into capillaries via capillary action and the XRF spectra then obtained. Each blank was then subtracted from its associated XRF spectra to yield the blank subtracted XRF data for each standard solution. This XRF data was then fitted with a series of Gaussians, one for each Kα and Kβ peak together with a third-order polynomial background; the summation of the area under the Kα and Kβ curves was taken as the fluorescence counts for each element. Instrument sensitivity (counts/fg metal/second) for each element was determined from the slope of the calibration curves (see Fig. 2), and as expected, increased with increasing atomic number. The optimized parameters, energy calibration, Gaussian widths, and Kα:Kβ branching ratios from the standards were held constant in subsequent linear least-squares fits of the XRF data for the cytometer traces.

In order to convert fluorescence counts from a cell to metal mass, it is necessary to know when the cell is in the beam. A visible-light microscope (Mitutoyo, M Plan Apo 5x objective; Infinitube Standard with Iris diaphragm; Edmund Optics 5012C, Color GigE Camera) was used to image cells in the capillary. Video data were analyzed by aligning each cell in each frame of the video with an ellipse, giving the time dependent position and velocity of each cell. The time-base for the optical and XRF traces were aligned by fitting the measured XRF for the element of greatest fluorescent intensity (Fe for red blood cells and Zn for 3T3 cells) to the predicted XRF based on the video. The latter was calculated using the measured time-dependent cell position and vertical beam profile. The position and rotation of the capillary relative to the beam were refined as part of the fitting process. The result of this analysis is a table giving the beam-profile-weighted fraction of each cell that is illuminated at each time point. This was used to fit, in a linear least-squares sense, the measured time-dependent Fe and Zn XRF signals to give the apparent mass of Fe and Zn per cell.

In addition to fluorescence from the cell, the measured XRF includes x-ray scattering and impurity fluorescence from the capillary. The first step in quantifying XRF fluorescence was to quantify this contribution, which we will call a blank, and remove it. The blank was determined by first identifying those time points at which no cells were present in the beam. The XRF for these points was summed and normalized by I_0, giving an experimentally determined blank which was subtracted from the remaining data. The blank subtracted XRF for each time point was then fit in a linear least squares sense using a series of Gaussians with the energy calibration, Gaussian widths, and K_α:K_β ratios fixed at the experimentally determined values.

II.3 RESULTS:

II.3.1 BOVINE RED BLOOD CELLS

A total of 805 bovine RBC cells were detected in 24 individual scans taken over a time period of ~5 hours. The linear velocity (3.2 µm/sec ± 2.5 µm/sec) resulted in cells being exposed to the beam for a mean of ~5 seconds. The total fluorescence from all 805 cells is shown in Figure 3. Despite the fact that the capillary contained significant Fe and Zn impurities, it was nevertheless possible to detect a well-defined Fe peak and a very small Zn peak in the background subtracted data. The higher noise level above ~10 keV is due to the much higher count rate at that energy due to the elastic and Compton scattering. The experimental uncertainty is proportional to the total number of counts, resulting in greater uncertainty in the difference (cell minus background) at 10 keV.

II.3.2 MOUSE FIBROBLASTS (NIH3T3)

A total of 31 mouse fibroblasts (NIH3T3) cells were detected in 6 individual scans taken over a time period of ~4 hours. Due to incomplete residence times, 7 cells were rejected leaving 24 cells for analysis. The linear velocity (8.3 μm/sec ± 5.4 μm/sec) resulted in cells being exposed to the beam for a mean time of ~5.5 seconds. The data for 3T3 cells are qualitatively similar to those shown in Figure 3, with the exception that the capillary used for these scans contained negligible Fe impurity.

The fluorescence signals for a single RBC and a single 3T3 cell are shown in Figure 4. For single RBC there is a detectable Fe peak but no Zn peak above the noise level. For 3T3 cells the Zn and K fluorescence peaks are both above background noise; however, Fe is undetectable. The histograms summarizing the Fe in RBCs, the Zn and K in fibroblasts, and the correlation plot summarizing the relationship between Zn and K in fibroblasts are shown in Figure 5.

II.4 DISCUSSION:

II.4.1 TESTS FOR ACCURACY

In order to test the accuracy of our data analysis, we examined the effect of cell density, background contamination and cell velocity on the apparent Fe concentrations.

II.4.1.1 CELL DENSITY

For some scans, the cellular concentration was high enough that two or more cells were in the beam at the same time. In order to test whether we were able to reliably deconvolve these signals we compared the apparent distributions for overlapping vs. nonoverlapping cells. Although the apparent Fe concentration of RBCs is not affected by cell overlap, the apparent width of the distribution in metal concentration increases significantly if more than two cells are in the beam at the same time (See Figure 6). This is presumably due to the inability of our fitting algorithm to reliably assign fluoresce to individual cells if more than two cells are in the beam. Accordingly, all of the analysis excludes cases with more than two cells in the beam at one time.

II.4.1.2 BACKGROUND Fe CONTAMINATION

Each position of each capillary (i.e., each individual scan containing multiple cells) was analyzed separately because of spatial differences in background contaminants. In order to test whether these variations in background interfered with cellular quantitation, we compared the apparent mean Fe content for each scan with the associated background level of Fe. Figure 7 shows the results of this comparison for the 24 bRBC scans, with each scan's mean Fe value representing data for ~ 20 to 60 cells.

Despite a 50-fold variation in Fe background levels, the slope of the best fit line for signal vs. background (0.024 ± 0.050; 95% certainty interval; r^2-value, 0.053) is not distinguishable from zero, indicating that the background had no effect on Fe quantitation. Both the lowest and highest mean Fe concentrations are found for scans having among the lowest contamination. The slope of the best fit line for population width vs. background (0.054 ± 0.050; 95% certainty interval; r^2-value, 0.22) is both positive and apparently different from zero. This might be a consequence of counting statistics, since cells with a larger background should be quantified less accurately.

II.4.1.3 CELL VELOCITY AND MASS QUANTITATION

Depending on the details of capillary conditions, there was a ~10-fold variation in cell velocity during measurement. If not properly accounted for in our analysis, this could affect the apparent XRF-determined concentrations. However (see Figure 8) there is no dependence of Fe concentration on cell velocity during measurement.

II.4.2 DISTRIBUTION WIDTHS

The experimentally determined mean Fe content of individuals RBCs (58 fg ± 27 fg) is in good agreement with previous findings [1, 2, 4]. One of the striking observations for the data is the surprisingly wide distribution in metal concentrations, with a 1.9-fold difference between the cutoff for the lowest quartile (39.9) and the highest quartile (76.7). Given the noisy signal (i.e., Fig 4) one might assume that the width in the distributions in Fig 5 is the result of noisy data. However, an average RBC traveling at the average velocity, after blank subtraction, gives ~173 fluorescent counts for Fe during its residence time in the beam. The statistical uncertainty in this measurement is governed by counting statistics ($\sim \frac{\sqrt{173}}{173} = 7.6\ \%$ or ~ 4.4 fg). The observed standard deviation (27 fg) is more than 6 times larger, indicating that the distribution in Fig 5a is dominated by biological variability not experimental uncertainty.

Similarly, the experimentally determined Zn and K content of individual NIH3T3 mouse fibroblasts, was 27 (± 16) fg and 789 (± 550) fg, respectively, in good agreement with known mammalian concentrations for Zn [18]. These showed a 2.3- and 2.8- fold differences between the 1st (16.3, 421) and 3rd (37.7, 1160) quartiles for Zn and K, respectively. Similar results are found for NIH3T3 cells, with experimental uncertainties of ±3 and ±53 fg for Zn and K, vs measured distribution widths of 16 and 550 fg, respectively.

Interestingly, the distribution is apparently asymmetric with an associated skew of 0.3885.

II.5 CONCLUSIONS:

We have developed an XRF-coupled flow cytometer that permits measurement of trace element concentrations for single cells with a frequency of ~0.25 Hz. Although the current data are quite noisy, it should be possible both to increase the solid angle from which signal is detected and to decrease the background signal. Even with the current instrument, we have found the biological population distributions of Fe, Zn, and K are quite large. This may reflect variation in sample condition (for example, no effort was made to synchronize cell ages or developmental stage) or may represent intrinsic variability due to mechanisms of homeostasis. Future work will be aimed at better understanding the factors behind these distributions. Nevertheless, it is clear that cell specific determination provides novel information not available from conventional bulk measurements.

II.6 REFERENCES:

1. Herring, W.B., et al., *Trace Metals in Human Plasma and Rd Blood Cells: A Study of Magnesium, Chromium, Nickel, Copper, and Zinc I. Observations of Normal Subjects.* American Journal of Clinical Nutrition 1960. **8**: p. 846-854.
2. Shamberger, R.J., *Calcium, Magnesium, and Other Elements in the Red Blood Cells and Hair of Normal Patients with Premenstrual Syndrome.* Biological Trace Element Research, 2003. **94**: p. 123-129.
3. Herring, W.B., et al., *Trace Metals in Human Plasma and Rd Blood Cells: A Study of Magnesium, Chromium, Nickel, Copper, and Zinc II. Observations of Patients with Some Hematologic Diseases.* American Journal of Clinical Nutrition, 1960. **8**: p. 855-863.
4. Kakkar, N. and M. Makkar, *Red Cell Cytograms Generated by an ADVIA 120 Automated Hematology Analyzer: Characteristic Patterns in Common Hematological Conditions.* Lab Medicine, 2009. **40**(9): p. 549-555.
5. Zahler, N.H., et al., *X-ray Fluorescence Imaging Reveals Cadmium Toxicity is Linked to Altered Copper Homeostasis in Yeast*. University of Michigan: Ann Arbor.
6. Kamizono, A., et al., *Identification of a Gene Conferring Resistance to Zinc and Cadmium Ions in the Yeast Saccharomyces cerevisiae.* Molecular & General Genetics, 1989. **219**(1-2): p. 161-167.
7. Vicentefranqueira, R., et al., *The zrfA and zrfB genes of Aspergillus fumigatus encode the zinc transporter proteins of a zinc uptake system induced in an acid, zinc-depleted environment.* Eukaryotic Cell, 2005. **4**(5): p. 837-848.
8. Li, L.T. and J. Kaplan, *Defects in the yeast high affinity iron transport system result in increased metal sensitivity because of the increased expression of transporters with a broad transition metal specificity.* Journal of Biological Chemistry, 1998. **273**(35): p. 22181-22187.
9. Pagani, M.A., et al., *Disruption of iron homeostasis in Saccharomyces cerevisiae by high zinc levels: a genome-wide study.* Molecular Microbiology, 2007. **65**(2): p. 521-537.
10. Fahrni, C.J., *Biological applications of X-ray fluorescence microscopy: exploring the subcellular topography and speciation of transition metals.* Curr. Opin. Chem. Biol., 2007. **11**: p. 121-127.
11. Madsen, E. and J.D. Gitlin, *Copper and Iron Disorders of the Brain.* Annu. Rev. Neurosci., 2007. **30**: p. 317-337.
12. Brehm-Stecher, B.F. and E.A. Johnson, *Single-Cell Microbiology: Tools, Technologies, and Applications.* Microbiology and Molecular Biology Reviews, 2004. **68**(3): p. 538-559.
13. Davey, H.M. and D.B. Kell, *Flow Cytometry and Cell Sorting of Heterogeneous Microbial Populations: The Importance of Single-Cell Analyses.* Microbiological Reviews, 1996. **60**(4): p. 641-696.
14. Leslie, M., *The Power Of One*, in *Science*. 2011. p. 24-26.
15. Kikuchi, K., K. Komatsu, and T. Nagano, *Zinc sensing for cellular application.* Curr Opin Chem Biol, 2004. **8**: p. 182-191.
16. Yang, L.C., et al., *Imaging of the intracellular topography of copper with a fluorescent sensor and by synchrotron X-ray fluorescence microscopy.* Proc. Natl. Acad. Sci., 2005. **102**(32): p. 11179-11184.
17. Kirkpatrick, P. and A.V. Baez, *FORMATION OF OPTICAL IMAGES BY X-RAYS.* Journal of the Optical Society of America, 1948. **38**(9): p. 766-774.
18. Eide, D.J., *Zinc transporters and the cellular trafficking of zinc.* Biochimica Et Biophysica Acta-Molecular Cell Research, 2006. **1763**(7): p. 711-722.

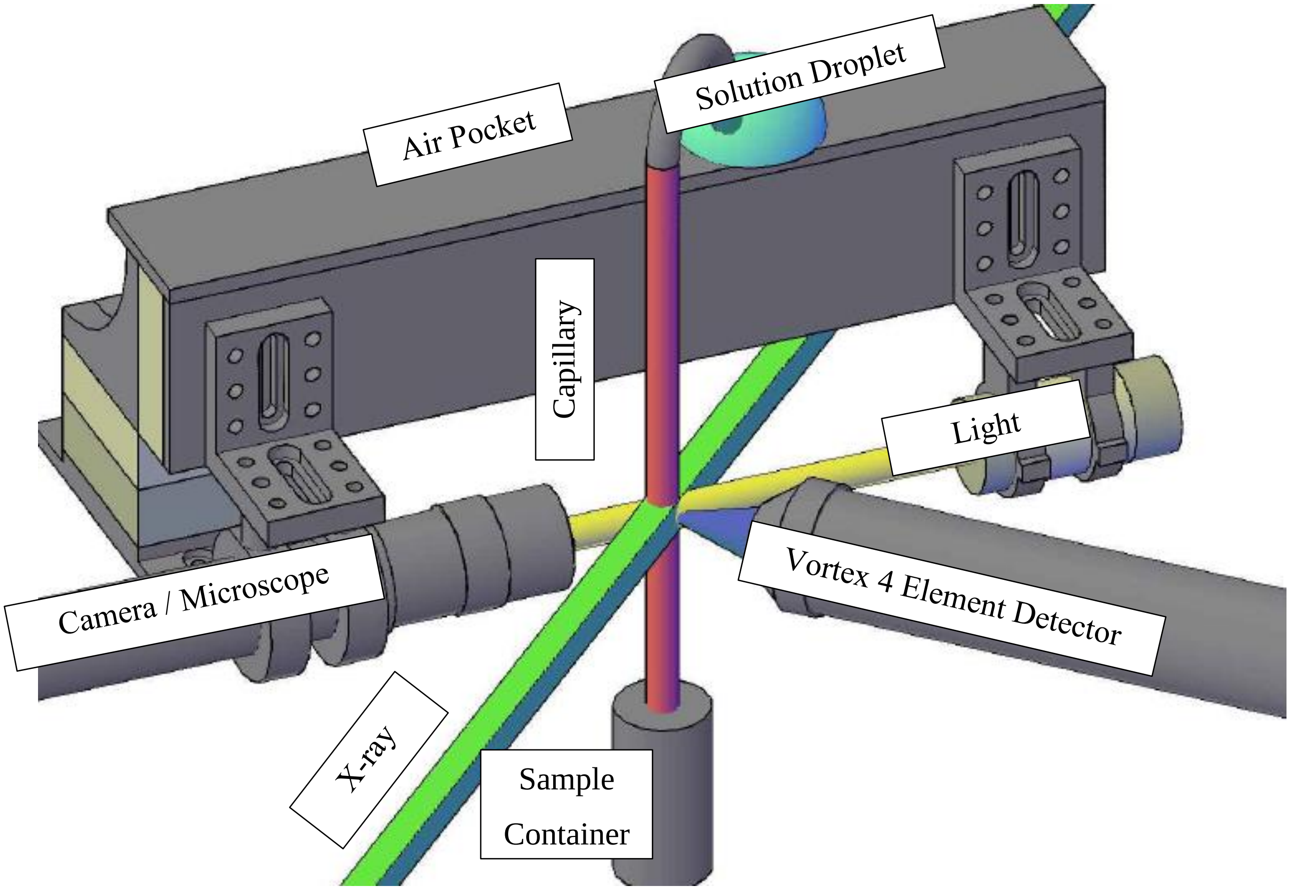

Figure II.1 Schematic illustration of the apparatus: The initial flow rate, from capillary action, was reduced dramatically by placing a droplet of solution at the end of the capillary. This traps an air pocket in the fold at the top of the capillary. As the droplet slowly evaporates, the air pocket is allowed to rise. The velocities of the cells were measured to be on the order of ~0.5 mm s^{-1} and a 20 cm capillary takes ~10 minutes to fill. Based on this, capillary action was used to load the sample capillary. The addition of a curve at the top of the capillary above the terminal end, allows for an air pocket to be trapped when a droplet is placed at the terminal end. This causes a dramatic decrease of cellular velocity to ~ 5 µm s^{-1}. As the droplet slowly evaporates, the air pocket is allowed to rise and with it the cells.

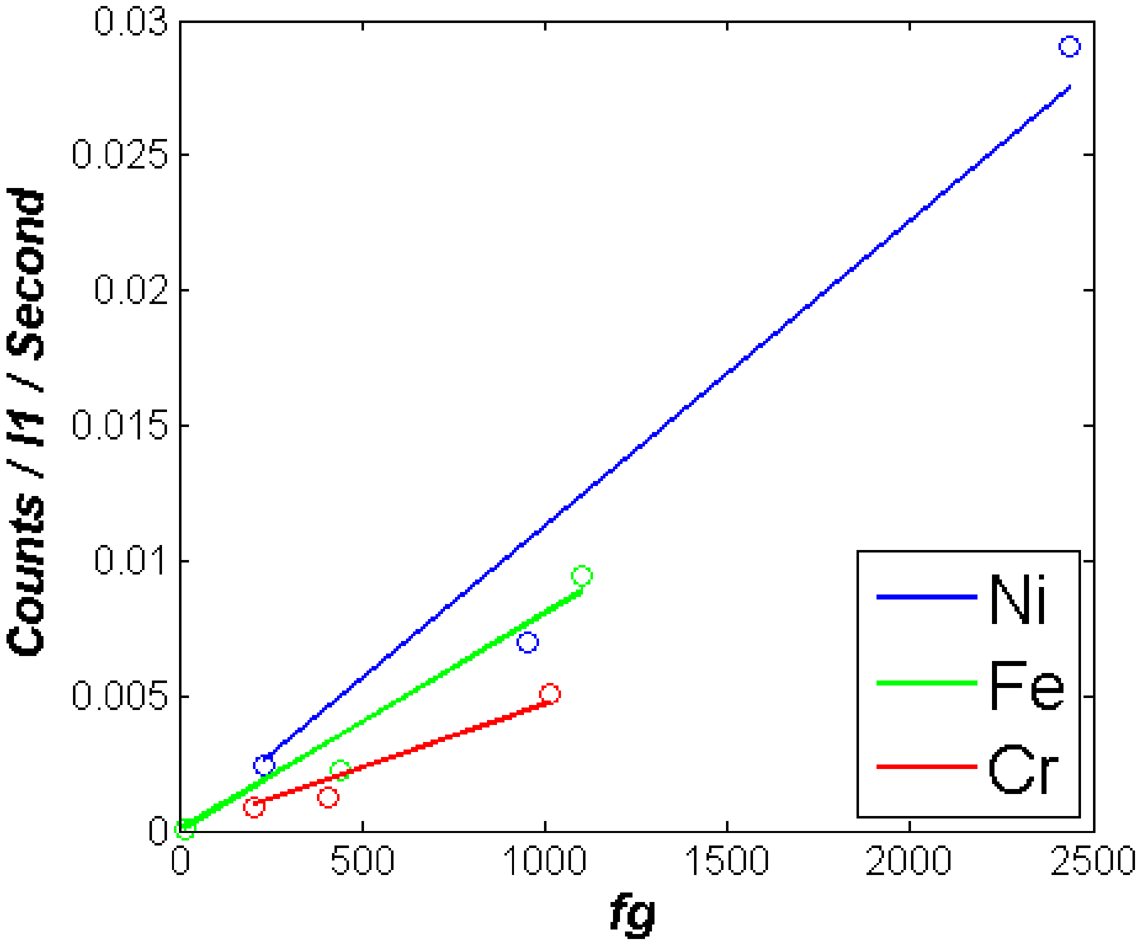

Figure II.2 Calibration Graph: Instrument sensitivity (normalized counts/fg metal/second) was determined from the slope of the resulting calibration curves. The calibrated sensitivities in units of $\frac{counts}{I0\ s\ fg}$ for Cr, Fe, and Ni were $\mathbf{4.7\ \times 10^{-6}}$, $\mathbf{8\ \times 10^{-6}}$, and $\mathbf{1.1\ \times 10^{-5}}$, respectively.

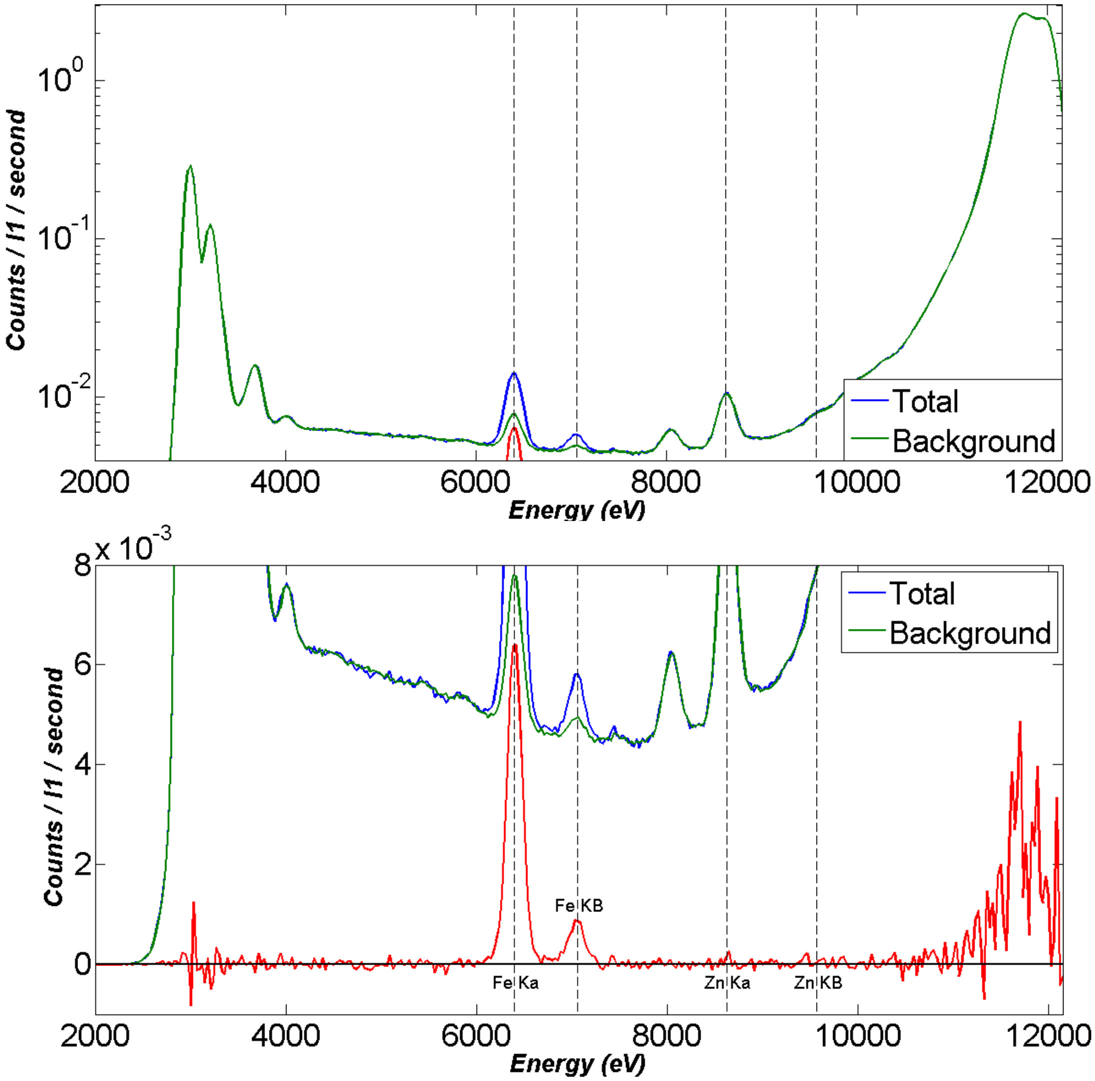

Figure II.3 Total XRF from all RBC Scans: A) Logarithmic and B) Linear scale plots of combined signal from all cells. Vertical dashed lines mark the energy of the Fe and Zn Kα and Kβ peaks

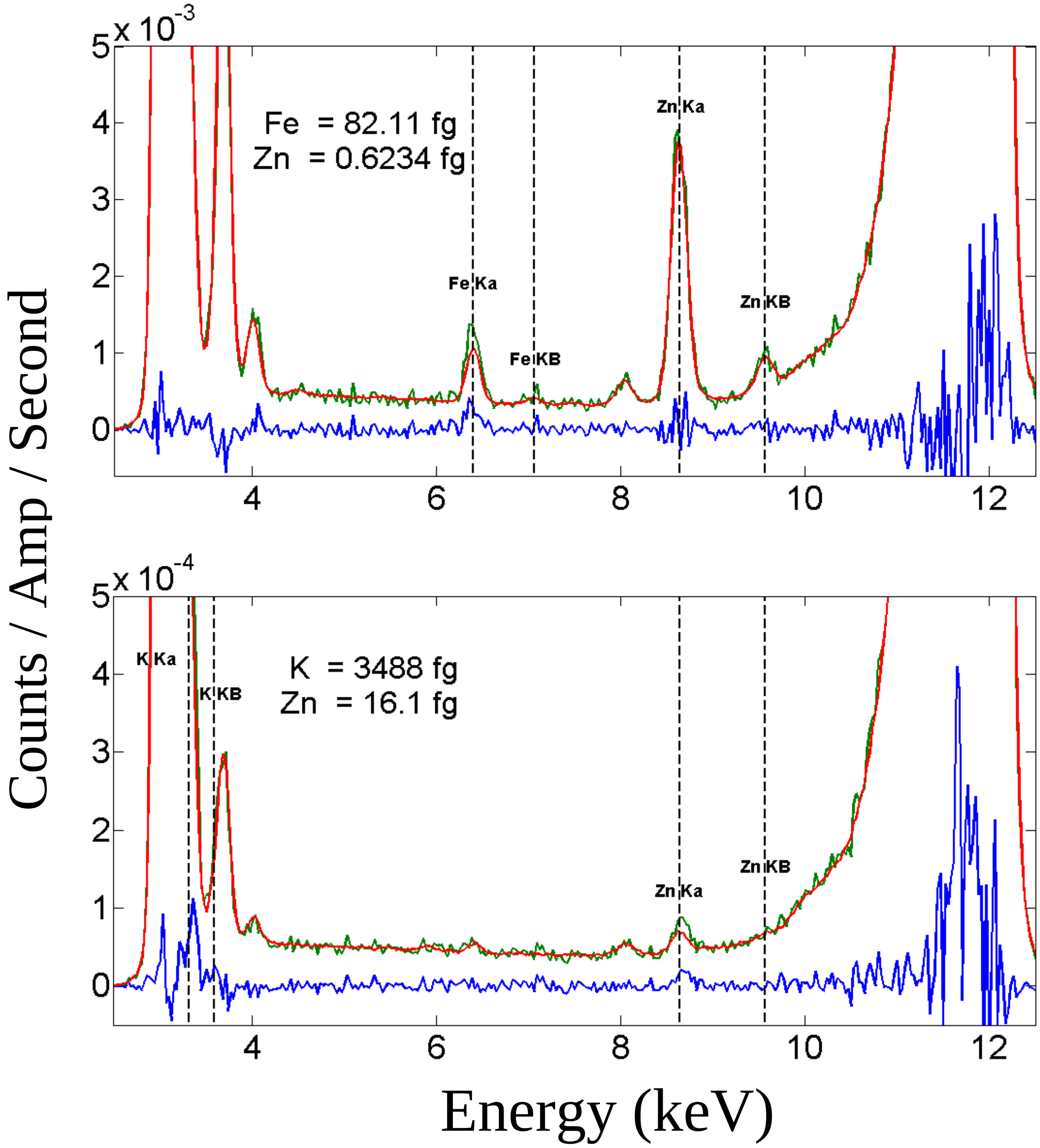

Figure II.4 Single Cell Spectra: XRF spectra for a single bRBC (top) and 3T3 (bottom): Both spectra contain the total fluorescence, the background fluorescence and the cellular fluorescence (total – background). The units are counts per second normalized by the upstream ion chamber. For bRBC, the quantified masses for Fe (82 fg) and Zn (0.62 fg), correspond to ~15 mM and ~100 µM, respectively [1, 3, 4]. For NIH3T3 cells, the masses for K (3480 fg) and Zn (16.1 fg) correspond to ~50 and ~140 µM, respectively. The peak height of the RBC Fe is ~4.2 x 10^{-4} with the peak height of the baseline being 1.3 x 10 $^{-4}$ giving a S/N ratio of ~3.4. Similarly, for the NIH3T3 cell the associated S/N is ~11 and ~2 for K and Zn, respectively.

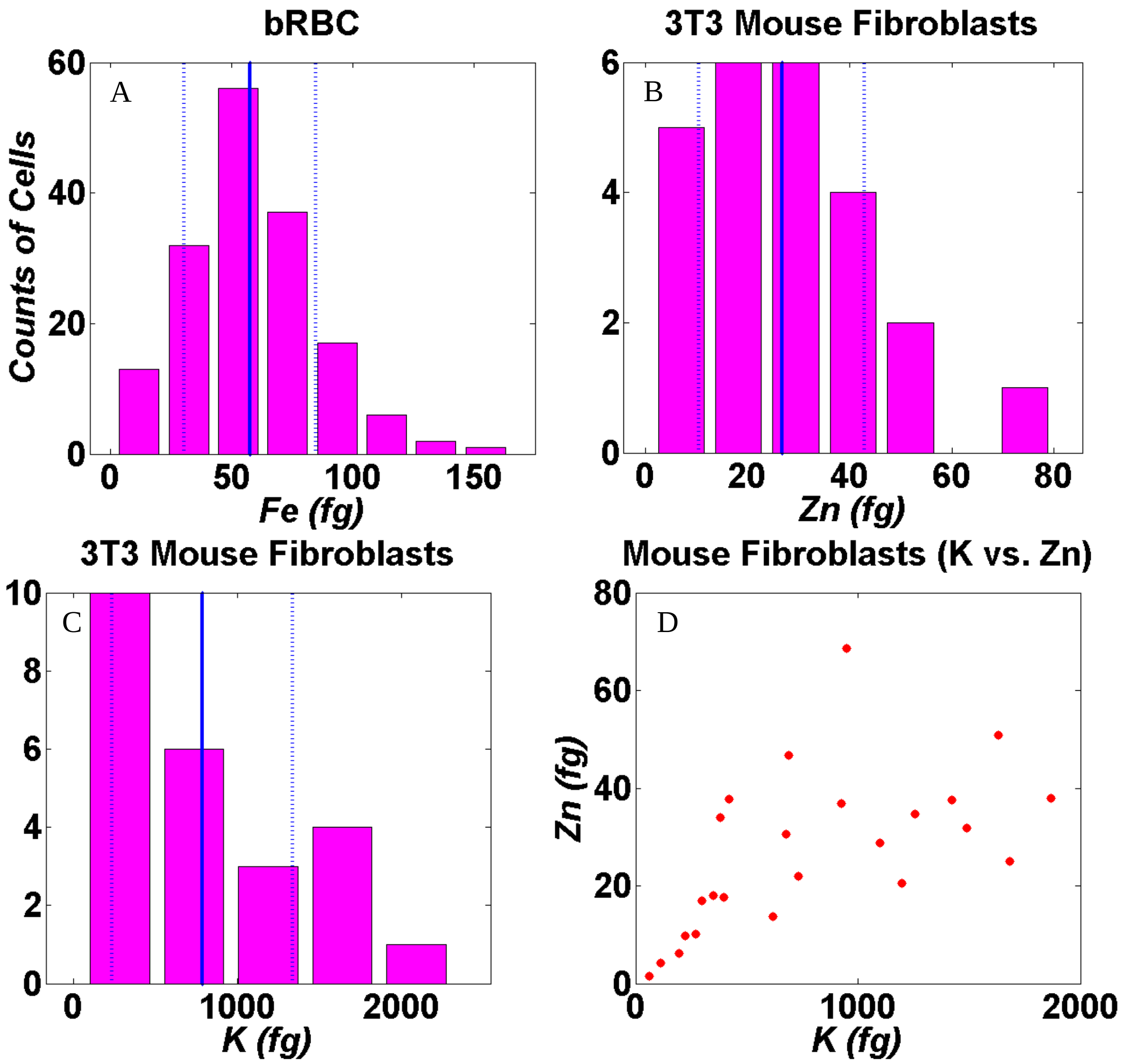

Figure II.5 Distributions and Correlations: (A) a cell-mass histogram for Fe in bovine RBCs; (B) a cell-mass histogram of Zn in NIH3T3 mouse fibroblasts; (C) a cell-mass histogram for K in NIH3T3 mouse fibroblasts; and (D) a correlation plot of K vs. Zn for NIH3T3 mouse fibroblasts.

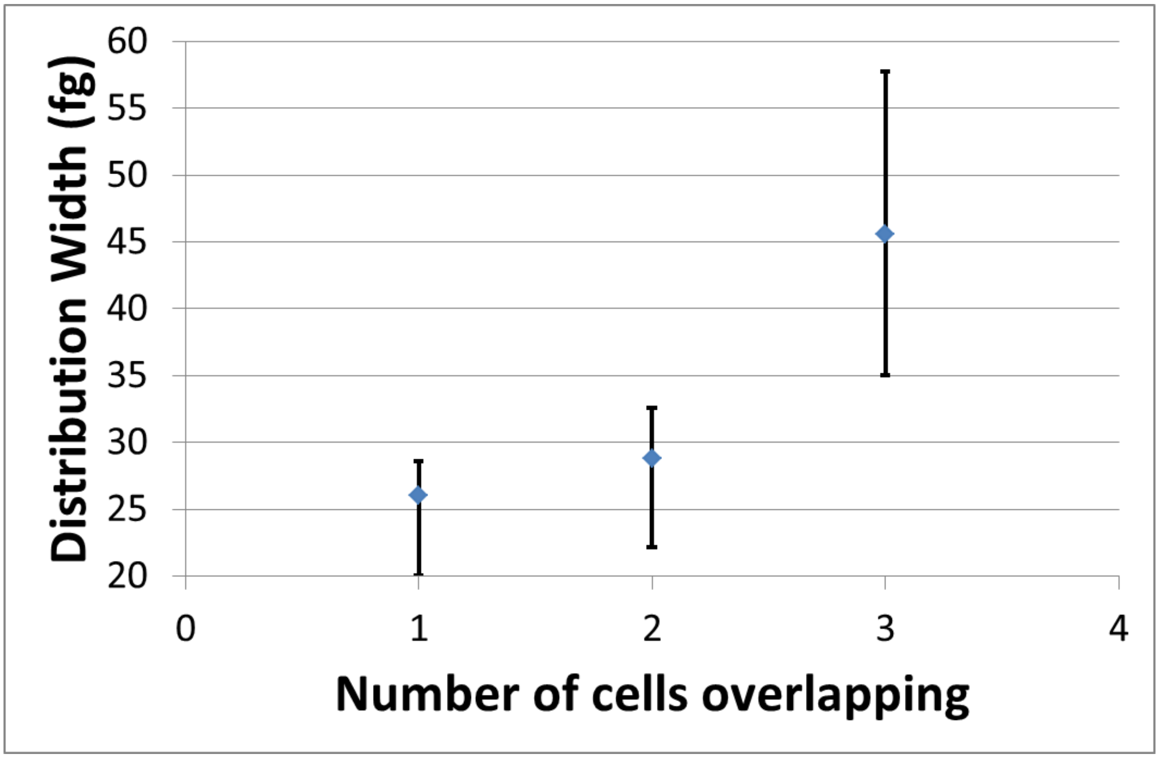

Figure II.6 Overlapping residence versus the associated distribution width: Using a two tailed F-Test, with 80% certainty, we can state that the population distribution obtained from three cells sharing residence through the beam is statistically different from that obtained from two cells overlapping or that of lone cells.

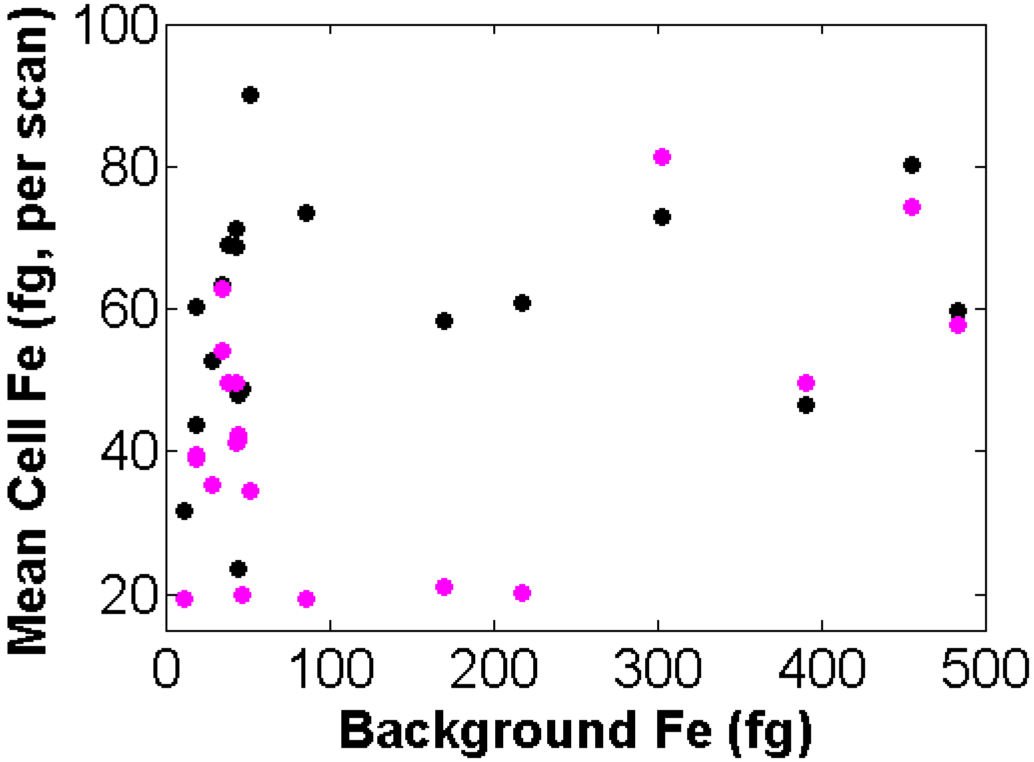

Figure II.7 Mean Quantitation vs. Background Contamination: The effect of the background Fe contamination on the apparent RBC Fe concentration. The mean (black) and std. deviation (red) of Fe concentration for each scan is plotted vs the background Fe contamination

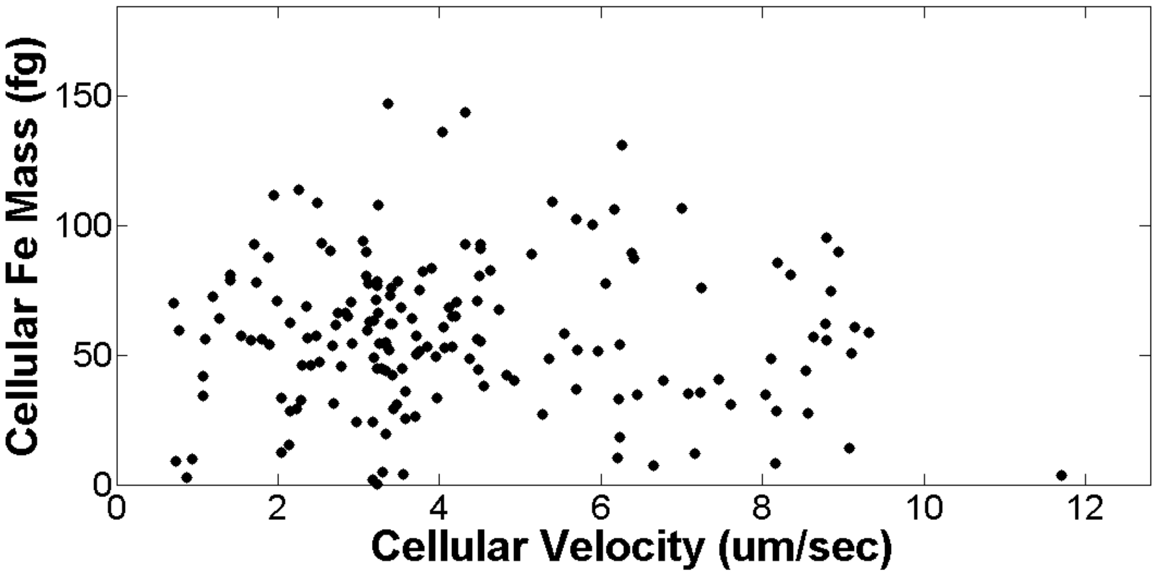

Figure II.8 Velocity vs. bRBC Fe Content: Comparison of the mean cellular velocity of a particular cell during its residence time with its calculated Fe content. Expectedly, there is a slope of zero indicating no relation between the two variables.

CHAPTER III: DATA ANALYSIS AND PROCESSING[2]

III.1 INTRODUCTION

Although the fitting of x-ray fluorescence (XRF) data [1-5] and the tracking of cells [6] are not new concepts, both the measuring of time-course XRF data (as opposed to position-course data of imaging) and the pairing of that data with cell "tracks" from video data to deconvolve the total integrated per cell signal from overlapping cells with variable x-, y-, and z-, coordinates and velocities has never been done before. As such, the cytometry methodologies presented in this thesis required the development of software to address four key research requirements of data analysis: instrument calibration, signal calibration, signal identification, and signal quantification. The following chapter and its associated units outline the rationale for each piece of software and make reference to particular software code and comparisons when necessary.

Due to the underlying physics, incorporation of video data was paramount to being able to extract quantified values of the various elements of each cell from the time dependent XRF traces. Because of this, the second portion of this chapter will discuss the additional treatment of the video data.

---

[2] Aniruddha Deb provided project guidance. Jim Penner-Hahn provided invaluable collaboration towards the developed methodologies.

III.2 INSTRUMENT CALIBRATION

There are two variables from the beam line that must be calibrated: the x-ray beam profile (or shape) and the detector (the digital binning of energies and the associated energy dependent full width half max (FWHM) of its resolution). The use of the beam profile is unlike XRF imaging where the profile is used to deconvolve the signals as a function of position; rather the calibrated beam profile is used in conjunction with video to build an array that is necessary to deconvolve the time-dependent signal of each cell. Both the profile and array are necessary to align the different time frames of the video and XRF data sets (see section III.4.2.3). As with imaging, calibration of the energy terms for detector binning and resolution are needed to convert the digital signal from the detector into fluorescence counts per element (see section III.2.3.3).

III.2.1 BEAM PROFILE

The profile of the incident x-ray beam was measured along the horizontal and vertical directions using a knife edge scan. A sample of uniform thickness with a very straight and clean edge (analogous to a knife's edge) was moved across the beam with its edge perpendicular to the direction of travel. As the sample moved through the beam, the fluorescence intensity was recorded. The measured signal, S when the edge is at x=b is $S(b) = \int_{-\infty}^{b} I(x)dx$, where I is the intensity of the x-ray beam. The beam profile was then calculated by taking the numerical first derivative of the knife edge scan and then normalizing it to a maximum value of 1.

III.2.2 DETECTOR PARAMETERS

The energy of each x-ray pulse is assigned to one of 2048 bins. The two parameters governing the fitting of XRF data are 1) the energy calibration of the detector's energy binning, and 2) the energy dependence of peak resolution. Bin number is fitted to energy using a second order polynomial, and peak resolution (FWHM of the detected X-ray peaks) is modelled by the expected detector response function, $FWHM = s_0 + s_1\sqrt{E}$; where E is the energy of the associated atomic transition, s_0 is the contribution from limitations in electric pulse processing, and s_1 includes combinations from Poisson statistics of the electron-hole pairs produced when each photon strikes the detector [7, 8].

Although x-ray emission lines have an intrinsic Lorentzian shape with a FWHM of ~10 eV [9], the experimental peak shape for most XRF detectors is much broader, with an approximately Gaussian shape and a FWHM of ~120 eV. Each XRF emission line was fit to the equation $Ae^{-\left(\frac{E-\bar{E}}{\sigma}\right)^2}$; where A is the amplitude of the emission line at energy, $\bar{E}$, and σ is the FWHM of the detectors response function at energy, $\bar{E}$. Since the FWHM of each line is governed by the detector response function, the Gaussian σ-values are energy dependent.

III.2.2.1 ALL OTHER PARAMETERS

All other fitting parameters are either referenced from known values or extracted directly from the sample scan itself. These parameters include the branching ratios [10-13] of the various elemental emission lines (e.g., Kα and Kβ), the fluorescence yield ratios (e.g., the ratio of Zn-K to Zn-L lines)[10-13], an estimation of the background/blank/baseline and an estimation of the scatter, both Compton and Elastic. Both the Compton and elastic scatter need to be accounted for during parameterization. This is because the Zn K-Lines rest on the scattering shoulder when excitation is at 10 keV; and failure to account for the scattering interferes with Zn quantitation. In all cases it was possible to obtain or extract an actual blank from the scan. In these cases, parameterization was significantly simplified as doing so, in many instances, removed the need to estimate any background or scatter.

III.2.2.2 PARAMETERIZATION OF ENERGY BINNING AND 4-ELEMENT DETECTOR ALIGNMENT

Each detector element can have a slightly different calibration. As such, each element was calibrated independently. The resulting calibrations were then used to align the signals from all four elements for summation. After summation, the existing set of calibration parameters was refined using the summation to create a single final set of calibrated parameters.

III.2.3 DETECTOR CALIBRATION

Depending on the specific experiment, detector calibration was achieved using either a standard or a sample. The difference between the two, being that sample scans can be blank corrected (Section III.3.2) and standards have to be baseline corrected. For sample scans, the ability to correct with a blank allows for the removal of all contributory background fluorescence leaving only the cellular emissions. This makes the determination of the energy dependent variables associated with detector calibration very simple. The inability to do this with standards makes detector calibration more difficult, as an accounting needs to be made of the contributing continuum of background signals (e.g., Compton scatter).

III.2.3.1 DETECTOR CALIBRATION USING STANDARD SCANS

For flow cytometry experiments, the standard solutions were not initially contained in the capillary that holds them and this allows for an *in situ* blank of the capillary to be taken prior to the loading of the standard solution.

III.2.3.2 DETECTOR CALIBRATION USING SAMPLE SCANS

Whenever possible, the determination of the detector's energy calibration and energy dependent parameters should be performed using sample scans even if standard scans are available. This is because it is not possible to treat the background properly for the standards because there isn't a blank region to subtract; even the blanks taken from the empty capillaries weren't perfect. Essentially, increased scatter from the standard solution causes baseline elevation making it very difficult to use in situ blanks. This is discussed further in Chapter 5.

Importantly, with sample scans (both 1D time-course and 2D image data), correction by a blank allows for an increased energy range for determining detector parameters as it provides an accounting of the background continuum of XRF without having to fit it. This is new and completely different from the current approach of the field which calibrates using standards. Unfortunately, this development wasn't incorporated until late in software development and was not actually implemented for the flow cytometer data. However, this approach was applied to the fitting of images discussed later in chapters 5 and 6.

III.2.3.3 PARAMETRIC EQUATIONS AND PARAMETER FITTING

The goal of detector calibration is to determine 5 key variables which govern 1) the FWHM as an energy dependent function of detector response, and 2) the energy binning associated with the detector channels.

$$FWHM = s_0 + s_1\sqrt{E};$$

Equation III-1

$$Energy\ of\ Detector\ Channels\ (E) = e_0 + e_1 \times (Channel) + e_2 \times (Channel)^2$$

Equation III-2

Where e_0, e_1, and e_2 are the intercept, slope and quadratic of the energy calibration, respectively, and where s_0 corresponds to limitations in electric pulse processing and s_1 is a combination of factors related to the electron-hole pairs produced in the detector [7, 8] when a photon of energy, E, strikes it, the overall equation for the fitting of the data is as follows:

$$Fluorescence\ Intensity$$

$$= C_{Blank} + \sum_{i=1}^{m} \sum_{j=1}^{n} A_i{}^{j} \sum_{k=1}^{p} \left(\frac{e^{-\left(\frac{(e_0 + e_1 \times (Channel) + e_2 \times (Channel)^2) - \bar{\mathrm{E}}_i{}^{j_k}}{s_0 + s_1 \sqrt{\bar{\mathrm{E}}_i{}^{j_k}}} \right)^2}}{(Branching\ Ratio)_i{}^{j_k}} \right)$$

Equation III-3

where the scan is over ***i*** elements with ***j*** series and ***k*** lines. The elements chosen for detector calibration were based on visual inspection of the blank corrected signal. The blank term at the beginning is extracted from the sample itself and can be considered a constant. Nonlinear fitting was performed in Matlab® using the Levenberg-Marquadt algorithm.

When a blank is not able to be extracted, the leading term C_{Blank} is replaced by a term for a baseline supplied by a snipping function (see section III.3.2) plus a term for both Compton and elastic scatter.

$$Elastic\ Scatter = A_{Elastic} \times e^{-\left(\frac{E - Excitation\ Energy}{s_0 + s_1 \sqrt{Excitation\ Energy}} \right)^2}$$

Equation III-4

$$Compton\ Scatter$$

$$= \begin{cases} A_{Lorentz} \left(\frac{2}{\pi \left(s_0 + s_1 \sqrt{\bar{\mathrm{E}}} \right)} \right) e^{-\left(\frac{E - \bar{\mathrm{E}}}{\left(\frac{\left(s_0 + s_1 \sqrt{\bar{\mathrm{E}}} \right)}{2} \right)} \right)}, E > \bar{\mathrm{E}} \\ \left(\frac{A_{Lorentz} \left(s_0 + s_1 \sqrt{\bar{\mathrm{E}}} \right)}{2\pi} \right) \bigg/ \left((E - \bar{\mathrm{E}})^2 + \left(\frac{\left(s_0 + s_1 \sqrt{\bar{\mathrm{E}}} \right)}{2} \right)^2 \right), \quad E \leq \bar{\mathrm{E}} \end{cases}$$

Equation III-5

The elastic and Compton scattering are discussed in this section because accounting for them during calibration (especially in the absence of a blank) is necessary for accurate fitting. The elastic scatter is modelled as a Gaussian and the Compton scattering is modelled as Gaussian with a left-sided (lower energy) Lorentzian. This approximation is imperfect but appears visually to be an adequate approximation of the scattering. The FWHM of the elastic Gaussian and the right-side Gaussian half of the Compton are determined by the FWHM equation of the detector response function from Equation III-1. For the Compton peak the amplitude of the left-sided Lorentzian is set to be identical to the right-sided Gaussian and the Lorentzian width is set to twice that of its Gaussian counterpart.

III.2.4 VECTORS AND MATRICES USED FOR DATA FITTING

After the parameters have been extracted, the coefficients of the detector response function and the coefficients of the detector binning energy dependence are held constant. These fixed parameters are then used to calculate vectors and arrays which are also held constant and used in linear least squares fitting of the XRF data. The vectors and arrays generated are the normalized fluorescence vectors (the summation of all the contributing equations for a particular emission normalized to a maximum value of 1), the scatter arrays (Compton and elastic), and the background array (which is variable depending on whether it is a blank/baseline or a polynomial and whether it is held constant across all pixels or scaled by a coefficient). These arrays are used to calculate the signal in linear least squares fitting.

III.2.4.1 FLUORESCENCE, BACKGROUND AND SCATTER ARRAYS

An array of intensity vs channel number was calculated for each fluorescence element using Equation III-3 and setting the blank contribution to zero. The background term is an M x 1 vector representing the first term in Equation III-3. The scatter is calculated using Equations 4 and 5.

1.1.1.1 FITTING OF XRF WITH EXTRACTED PARAMETERS

The XRF data, F, was fit as a series of linear equations

$$Ac = F$$

Equation III-6

where A is the array from III.2.4.1 containing the fluorescence, background, and scatter functions,

$$A = \begin{bmatrix} Element_{1,1} & Element_{1,2} & \cdots & Element_{1,n} & B_1 & Compton_1 & Elastic_1 \\ Element_{2,1} & \ddots \quad \ddots & & Element_{2,n} & B_2 & Compton_2 & Elastic_2 \\ \vdots & \ddots \quad \ddots & & \vdots & \vdots & \vdots & \vdots \\ Element_{m,1} & Element_{m,2} & \dots & Element_{m,n} & B_m & Compton_m & Elastic_m \end{bmatrix}$$

Equation III-7

and C is a vector containing the coefficients solved for using linear least squares.

III.2.4.2 CALIBRATION OF STANDARD MASSES

Solid standards have a uniform thickness, making it easy to determine metal concentrations in g/cm^2, and giving the total illuminated mass when multiplied by the beam size. This is the dominant practice in the field. However, for the flow cytometer we developed and used solution standards of dissolved metal ions as doing so more closely resembled the experimental set up. For solutions, metal content (mg/L) was determined using ICP and the volume illuminated by the beam was calculated from the capillary inner diameter and the beam height. These data allowed determination of counts per gram of metal illuminated.

III.2.4.3 SENSITIVITY CALIBRATION SLOPES

For solution standards, multiple concentrations were measured. Since the current approach is to use single point calibrations from highly concentrated standards, this is very different. The sensitivity is the slope of the straight line fit of intensity vs mass. In order to estimate the sensitivity for elements where we didn't have a calibration, we corrected the measured sensitivities for absorption (due to air [14], capillary [15], and solution), the fluorescence yields [16, 17] of the element, and the associated photoionization cross sections [18]. In principle, the corrected sensitivities should be the same for all elements. Because our corrections aren't perfect, the corrected sensitivity was modelled as a linear function of Z, and this fit was used to estimate the sensitivity of the other elements. These estimated values were then multiplied by their associated absorption (due to air, capillary, and solution), fluorescence yields, and photoionization cross sections (associated with the given excitation energy) to give expected sensitivity in $\frac{counts}{fg \times I_0}$. **Figure III.1** is a representative calibration curve.

III.3 XRF DATA

III.3.1 DIFFERENCES BETWEEN TIME-COURSE AND POSITIONAL XRF DATA

Although XRF time-course data and XRF imaging data represent different things, they have the same functional form (detector output, ion chamber values, etc) and can be analyzed the same way. For instance, although time-course measurements are recorded across time, not space, time-course measurements are functionally identical to an image of size M x 1, where M is the number of time points collected and the integration time (or live time) is the step size between the time points in temporal space.

III.3.2 BACKGROUNDS, BLANKS, AND SCATTER

The concept of a background can be understood as the experimentally measured signal when no sample is present and baseline – an attempt to model the signal that should be observed if there were no fluorescence from the sample. Depending on the method applied, a background can be fitted or measured.

A fitted background, or baseline, can be derived in many different ways. It can be assigned manually, calculated with a snipping function, or fitted, for example with a polynomial. In the two cases where it isn't assigned manually, the background can be calculated for the spectrum sum (the sum of each channel across all pixels of the dataset), or can be calculated separately for each individual pixel. If the background is calculated for the spectrum sum, it can be held constant for all pixels or can be scaled in order to best model each individual pixel.

The most common approach to determining a baseline background utilizes what is called a snipping function [9]. A snipping function compares each channel n, of a spectrum, to its two neighbouring channels, $n \pm 1$; if the intensity at channel n is greater than the mean intensity of channels $n \pm 1$ then the output intensity at channel n is set to the mean intensity value of its two neighbours. This function is sensitive to local minima and performing it iteratively has the effect of peak stripping.

In contrast to baseline modelling, it is sometimes possible to segregate the data into two distinct sets of signal (or cell) and non-signal (or blank). This allows for the removal of all contributing fluorescence that does not arise from the cells. This correction should give spectra which consist solely of signals from the cell. This is what was done for detector calibration in section III.2.3.2. After the background pixels have been identified, a blank can be calculated in two different ways: 1) by taking the mean spectra of all non-cell pixels, or 2) fitting of an interpolative function to allow for fluctuating background ratios of elements across the image or time trace. For the latter, (**Figure III.2**) an independent spline or polynomial interpolation is fit for each channel of the data set using the non-cell pixels' spectra as the seed values. Spline interpolation is done by using the center of each group of non-cell pixels as the break points between each constituent third-order polynomials of the spline. For polynomial interpolation, a tenth-order polynomial is used. For 2D images, two separate interpolations are performed; one across the rows of the image, and another down the columns. The mean of the two is taken as the value for the blank at that position.

III.3.3 FITTING XRF SAMPLE DATA

The dominant approach when fitting XRF data is to employ positivity constraints when fitting the fluorescence lines, and when fitting baseline corrected data this does not decrease the accuracy of the answer. However, nonlinear fitting is computationally taxing and decreases computational efficiency; and most importantly, isn't necessary as it has a negligible impact on the data (**Table III.1**B). In contrast, *blank corrected* XRF data must be fit as true linear least squares without the imposition of non-negativity constraints. Though it may seem intuitive to constrict the fitting of fluorescence to ≥ 0 as it is impossible to have negative fluorescence, doing so for blank corrected XRF data will artificially inflate the amount of fitted XRF in the presence of noise (see **Table III.1**A). This happens because the percentage change in the mean counts of blank corrected cellular pixels increases when the fit is positively constrained. Rather than being randomly distributed around zero, only non-negative values are possible. The increase occurs more for background pixels than for cell pixels since, in principle, the cell pixels have values that are randomly distributed around a positive value, and are not affected by the non-negativity constraints. This is demonstrated by the fifth column in **Table III.1**A, which shows that additional correction of the inflated values by subtraction of the background mean overcompensates and causes the resultant values to be less than those fit without positivity constraints.

An example of how noisy a single pixel can be is shown in **Figure III.3**. In terms of noise, whenever a signal arises from a small difference between two large numbers, as is the case with blank subtracted XRF, random fluctuations around a mean of zero - with a standard deviation of the square root of the number of counts of the original (non-blank subtracted) signal - are to be expected. Ignoring the negative contribution while fitting the positive fluorescence of that baseline will cause an artificial increase in reported background. When the signal is close to the baseline, random fluctuations in the signal are even more important. Solving for the positive fluorescence while artificially setting all the negative values to zero will always fail to compensate for this artificial increase and result in a reported amount of metal that is less than the true value following subtraction of the background mean.

III.4 FLOW CYTOMETER SIGNAL IDENTIFICATION – VIDEO DATA

Cells have variable sizes, metal content, velocities, and in some cases overlapping beam residence times, making single cell quantification of metal content impossible from XRF alone. In order to deconvolve the signal from overlapping cells one needs to know, at a minimum, when each cell enters and exits the beam. Cellular paths in the beam are not uniform, therefore the position of each cell at every point in time when it's in the beam must be known. Most importantly, without some manner of visualizing capillary flow, it is impossible to know whether a peak in the XRF corresponds to a single cell or multiple overlapping cells. For these reasons, the capillaries, and the cells flowing through them, were imaged with video data collected synchronously with XRF, using a horizontal visible-light microscope, (Mitutoyo, M Plan Apo 5x

/ 10 x objective; Infinitube Standard with Iris diaphragm; Edmund Optics 5012C, Color GigE Camera).

In order to align the video and XRF data, we first estimated the beam's location in the video. As the beam irradiates the capillary it also slowly (5-10 minutes) discolors the capillary, providing a visual estimate of beam position.

III.4.1 PROCESSING OF THE VIDEO DATA

Post collection processing of the video data (to track the cells as they traversed the capillaries) required four separate operations:

1. Each frame of the video was parsed into cell and non-cell.
2. The cells of each frame were connected across frames to construct the path of each cell.
3. The beam profile was interpolated from a profile with pixel increments equal to the step size of the native knife edge scan to increments equal to the pixel size of the video. This was done so that the step size (the spacing in y) aligns with the pixel size of the recorded video. This is necessary to align the video and XRF data sets. Following this, an initial best guess of its vertical position in the video was assigned.
4. The individual tracks of each cell were then convolved with the aligned beam profile to yield a pseudo-fluorescence trace, that is, the predicted fluorescence for the cell as a function of time (video frame number).

III.4.1.1 SEPARATION OF CELL FROM NON-CELL IN THE VIDEO DATA

First, the user selects specific frames as "seeds" for manual video parameter optimization. These "seeds" are then analyzed manually to identify cells. This is done by first calculating a frame dependent blank that gets subtracted from each video frame. Following the blank subtraction, the residuals (pixels) of the video frame are then processed with an intensity threshold and then filtered to create a binary mask that represents cell (1) and non-cell (0). Following this, each independent grouping of 8-connected '1's can be directly fit with an ellipse, or a Circular Hough Algorithm can be performed on the total binary image to identify overlapping cells. This binary mask is processed to extract the x, y, r_{minor}, r_{major}, angle of the associated ellipse, for each cell, in each frame.

III.4.1.2 CONNECTING THE CENTROIDS TO CREATE TRACKS

At this point, the actual path of each cell can be determined from the centroids. This is done by connecting the centroids across frames to identify the exact path of each specific cell. The GUI that performs this process applies three user designated parameters to discriminate and determine the tracks: 1) the maximum displacement between connected points, 2) the minimum number of points to make a track eligible, and 3) the maximum number of frames that can separate two connected points of a track. These parameters are chosen by the user and are primarily governed by how well "cell' was separated from "non-cell" during the video processing. Manual intervention can be necessary when the video is blurry or when the cell concentration is sufficiently high enough to cause cells to overlap; for this reason, tracks were verified visually.

III.4.2 CAIBT, XRF, AND ALIGNMENT

Both the identification and tracking of objects in video data and the fitting of XRF data are well established techniques [19]. However, combining XRF fitted time traces of elements with cellular "tracks" to deconvolve single cell total integrated fluorescence counts is new. Furthermore, the development of the associated methodologies was integral to the analysis of XRF flow cytometry data and without them the data from the XRF flow cytometer are meaningless.

III.4.2.1 INITIAL VIDEO ROTATION AND PLACEMENT OF THE VERTICAL BEAM PROFILE

The pixel size of the video was calculated from the pixel size of the CCD (2.2 µm, Edmund Optics 5012C, Color GigE Camera) and the magnification of the objective. For a CCD with a pixel resolution of 2.2 µm, using a 5X objective, this gives a pixel spacing of 0.44 µm. The calculated beam profile was interpolated onto this grid. There are two parameters with respect to the beam profile position on the grid: its vertical position and the angle of rotation between the apparent normal vector of the video grid and the true normal vector associated with the profile. For ease of visualization, the GUI displays a semi-transparent beam profile on top of the video image. This projection can be adjusted vertically to align it with the discolored portion of the capillary in order to set the initial guess. Likewise, to address any difference in the angle between the projection and the discolored portion of the capillary, the rotation of the video data can be adjusted.

III.4.2.2 CAIBT

The track information was combined with the beam profile to give an output array containing the normalized convolution of each cell's vertical profile (the summation of its area along each row of pixels) with the vertical beam profile. This is the "cell-area-in-beam-trace" or CAIBT. The CAIBT is an M x N array where, M is the frame number of the video and N is cell number. Later, after alignment of the video and XRF data, each column is interpolated from the time basis of the video into the time basis of the XRF data and M becomes the integration number of the XRF data. The columns of this array are each normalized to a maximum of one.

The CAIBT is the theoretical array of fluorescence counts for each cell that would be detected if all cells had the same amount of elemental mass, regardless of cell size, homogenously distributed throughout the cell. Summation along each row of the CAIBT would yield the theoretical fitted XRF signal for a given element. Summation down each column of the CAIBT would yield the theoretical total integrated counts for each cell in units of counts x integrations x I_0^{-1}. Interpolation of the CAIBT's timeframe into the time frame of the XRF data allows for the deconvolution of the amplitudes for each column. This allows for the total integrated counts of each cell to be calculated using the entirety of the dataset. Interpolation and alignment of the CAIBT with the XRF data is discussed in Section III.4.2.3. Deconvolution of the amplitude for each cell represented in the CAIBT is discussed in Section III.6 . Calculation of the total integrated counts for each cell is discussed in Section III.6.

The calculated CAIBT depends on the vertical positioning of the beam profile and the rotation of the video image, both of which may change from scan to scan. These values were refined iteratively.

Calculation of the CAIBT involves a separate calculation for each cell. Each calculation starts with a 2D binary image (**Figure III.4**A) of the cell calculated from the fitted r_{minor}, r_{major}, and phi for a cell. The binary image is summed along the horizontal axis to give a column vector which is the vertical profile of the ellipse (**Figure III.4**B). The next array is referred to as a *positioned ellipse profile array* (**Figure III.4**C). This is an M x N array where M is the total number of vertical pixels in a frame and N is the total number of video frames containing the cell. Each (m, n) value is the amplitude of the cell's vertical profile at m, n. Multiplication of the transpose of the *positioned vertical ellipse profile array* by the *vertical beam profile* (**Figure III.4**D) yields the convolution (**Figure III.4**E) of the *ellipse profile* with the *vertical beam profile* giving the theoretical integrated fluorescence counts of a cell as a function of time.

$$Convolution_{N\times 1} = (Positioned\ Elipse\ Vertical\ Profile_{M\times N})^T \times (Beam\ Profile)_{M\times 1}$$

$$CAIBT_{N\times C} = [Convolution(1)_{N\times 1} \quad Convolution(2)_{N\times 1} \quad \ldots \quad Convolution(C)_{N\times 1}]$$

III.4.2.3 ALIGNING VIDEO DATA WITH XRF DATA

The sampling rate of the detector was 4 Hz. The frame rate of the video was much higher, typically 20 Hz. Therefore, aligning the video data with the XRF data required the video frame rate to be down-sampled to 4Hz.

In addition to video rotation and the vertical position of the beam profile, two more parameters were optimized: a slope for converting the video time frame to the XRF time frame, and a time offset between the video and XRF. These are solved for by a grid search of possible rotation and beam position values (the initial beam position ± the distance of 10 video pixels and the initial video rotation ± 1˚ at steps of 0.2˚). At each point on this grid, the time offset and the relative frame rate were optimized. This optimization is represented in **Figure III.5**. **Figure III.6** displays the energy well associated with refinement of profile shift and video rotation; **Figure III.7** is a schematic of the program flow.

To align the XRF with the CAIBT, an XRF channel (e.g., Fe) as a function of time is compared with the CAIBT and the offset and relative frame rate are optimized iteratively. At this point a linear least squares fit is used to determine the elemental concentrations that give the best fit for this alignment. This process is then repeated for the next point in the grid.

III.5 DECONVOLUTION PROCESSES

III.5.1 PRIOR TO DECONVOLUTION

The two traces - the XRF element time trace and the aligned CAIBT - are 'cleaned'. For the XRF trace this consists of setting to zero 1) all XRF time pixels that were not aligned with video, and 2) all XRF recorded when the shutter was closed. For the CAIBT this consists of, 1) removing all cells that have no overlap with the beam (either because they never crossed the beam region or the shutter was closed), 2) setting to zero all video frame indices corresponding to the absence of XRF data (i.e., they were collected outside the purview of the associated XRF data collection).

Once this is done, the fitting can be performed either as a linear least squares which allows for negative concentrations, or as a constrained non-linear least squares with non-negativity constraints.

III.5.2 DECONVOLUTION OF THE XRF FROM EACH CELL

For the data in this thesis, each cell's contribution to the total fitted XRF time trace of each element was solved using a positively constrained nonlinear least squares variant of Equation III-6. Following this fit, any cells that were solved to have a zero trace (a trace that has zero amplitude) are thrown out. Any cells that overlapped with the 'zero' cells were also thrown out. After each cell's total time dependent fluorescence trace had been solved, the counts were integrated and converted to mass using Equation III-8.

III.5.3 ACCOUNTING FOR CELL LEAKAGE

At times it is necessary to allow for time dependent decreases in concentration that arise from prolonged exposure to the beam. For most scans, time dependent decreases were negligible. However, if a cell gets stuck in the beam it appears to slowly leak metal. This can be modelled by a first order decay. A graphical representation of a scan that suffers from a cell being stuck in the beam, along with the fits both accounting and not accounting for cell leakage are presented in **Figure III.8**. As can be seen in **Figure III.8**A, inclusion of leakage improves the fit quality by nearly 40% (0.000730 vs. 0.00102). There are noticeable time-dependent errors in the residual, **Figure III.8**C, if leakage is omitted. The dashed red line and blue line in **Figure**

III.8C are the fits that neglect and account for cell leakage, respectively. Notice the time dependent change in the difference between the two fits from left to right. **Figure III.8**B, the fit to the data for all the cells accounting for the cell leakage, shows that this is caused by a single cell; the trace of that cell is the blue line in that figure. **Figure III.8**D corresponds to snap shots of a cell at 0, 3, and 6 minutes ($*_1$, $*_2$, and $*_3$ in **Figure III.8**B) after it has been stuck in the beam. Like the capillary, the cell begins to char, and additionally it also appears to shrink. Importantly, the impact of the time dependent error, demonstrated in **Figure III.8**C, (that occur when a cell is stuck in the beam and leaking) is an increased distribution of masses which can be seen **Figure III.9**.

III.6 METHODS OF INTEGRATION

For each cell, the total fitted counts for each element depend on both the cell velocity and the beam height. Assuming a constant Δy displacement from each integration to the next (i.e., assuming constant velocity), Equation III-8 below accounts for both cell velocity and beam height and is used to calculate the total mass of each element in each cell.

$$Cell\ Mass\ (fg) = \frac{XRF\left(\frac{integrated\ counts\ \times integrations}{I_0}\right) \times IntegrationTime\left(\frac{seconds}{integration}\right) \times\ Cell\ Velocity\left(\frac{\mu\mathrm{m}}{second}\right)}{Calibration\ Slope\ \left(\frac{integrated\ counts}{fg\ \times\ I_0}\right) \times\ Beam\ Height\ (\mu\mathrm{m})}$$

Equation III-8

The total integrated counts for each cell (XRF in Equation III-8) can be calculated via temporal integration or positional integration.

III.6.1 INTEGRATING WITH RESPECT TO TIME

As the cell passes through the beam, its position (x, y) is determined as a function of time from the video. The data analysis (above) allows pairing these with fluorescence as a function of time. Taking the measured counts (counts/I_0) as a function of the frame number and integrating with respect to frames, gives the total fluorescence counts of the fitted XRF data in units of (counts * frames)/I_0. Since a frame is equal in length to the integration time of the XRF data, this unit is identical to units of (counts * integrations)/I_0.

When integrating with respect to time, the velocity was a 2-point average calculated by taking the difference of the vertical positions and the associated time between the first and last time point of fluorescence for the associated cell. However, this neglects non-ideal paths through the beam. Because the velocities of the cells had to be slow enough to allow for statistically meaningful fluorescence counts, the cells are able to rock back and forth and display fluctuating velocities while traveling through the interrogation zone of the beam. These non-ideal paths change the amount of fluorescence that is detected, and ultimately made integrating with respect to time an inadequate method for calculating total counts

III.6.2 INTEGRATING WITH RESPECT TO POSITION

Figure III.10 is a graphical representation of non-ideal behavior of the cell as it travels through the beam. Note the deviation of the cell as it spends a far greater proportion of its time outside the bright spot of the beam. This would cause the cell's calculated total counts to be less than what would be calculated if the cell had a uniform path through the beam. Conversely, the second plot demonstrates a cell that gets stuck in the beam's hot spot for some time. In this scenario, the cell's calculated total counts will be much greater than were the path ideal. Essentially, a cell can spend as much time going back and forth in the beam, so long as every part of that cell equally samples the vertical profile of the beam. If this is not the case, integrating with respect to time will either over-estimate or under-estimate the value.

Alternatively, the convolution of the cell traces can be converted from the time domain to the space domain. At each centroid position (x, y) the cell will give a specific number of integrated counts. The y-points are sorted in increasing order and the corresponding integrated photon counts are reorganized to match the resorting of the y-points. These points are then used to interpolate integrated photon counts that would be associated with every cellular integer y-position through the beam. A trapezoidal approximation of the integral is used to calculate the total integrated counts corresponding to the convolution of the beam with a point separation equivalent to the pixel resolution of the camera (e.g., 2.2 microns/pixel) divided by the objective magnification (e.g., 5x). This convolution is now equivalent to the convolution seen for a cell traveling at a velocity of one pixel (distance) per integration (time). This gives a pixel separation of 0.44 microns/pixel and hardsets the velocity (or the apparent velocity associated with the integration) to 1.76 µm/sec (for an integration time of 0.25 seconds with an objective magnification of 5X).

$$\frac{1\ Pixel}{Integration} \times \frac{1\ Integration}{n\ Seconds} \times \frac{y\ Microns}{Pixel} = \frac{y}{n}\ microns/second$$

Equation III-9

The above equation gives the velocity of the cell corresponding to the interpolated convolution. This velocity is equivalent to the camera resolution (y-Microns/Pixel) divided by the integration time (n-Seconds/Integration).

The resulting values for integrated counts and velocity are inserted into Equation III-8 (page 64) to yield the total mass in fg for each element detected for each cell.

III.7 SUMMARY

An overview of the processes involved in the fitting and analysis of the raw XRF flow cytometer data is presented in **Figure III.11**. Part A encompasses discussions from section III.2 and handles the calibration of the detector parameters (section III.2.3.2), beam calibration (section III.2.1), and sensitivity calibration (section III.2.4.3). Part B deals with combining the XRF sample data (section III.3.3), the beam profile (section III.2.1), and the cell size and positions from the video data processing (section III.4.1) to deconvolute the total integrated counts from each cell (section III.6) for each element. Part C combines the output from the sensitivity calibrations (section III.2.4.3), the calibrated beam parameters, (section III.2.1), the total integrated counts (section III.6.2) and the cellular velocities (section III.6) to calculate the total mass of each element in each cell using Equation III-8.

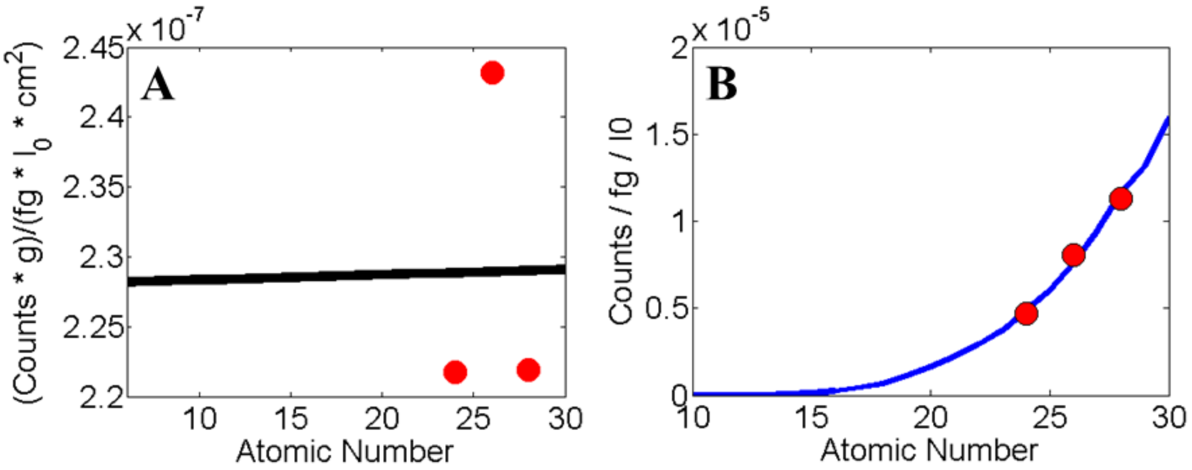

Figure III.1 Accounting for the sensitivities of the other elements: (A) modelling of the corrected sensitivities as a linear function of Z. (B) The line representing the estimated values obtained by taking the corrected sensitivities from the linear function of Z, for atomic numbers $9 < Z < 31$, and multiplying them by their associated absorption (due to air, capillary, and solution), fluorescence yields, and photoionization cross sections (associated with the given excitation energy) to give expected sensitivity in $\frac{counts}{fg \times I_0}$.

A	***BLANK CORRECTED DATA***				
	REGULAR	**POSITIVELY CONSTRAINED**		**PERCENT CHANGE**	
Element:	***(a)*** **CELL**	***(b)*** **CELL**	***(c)*** **CELL - BKGD**	***(d = [b-a]/a)*** **BLANK CORR.**	***(e = [c-a]/a)*** **2X BKGD CORR.**
Si	1.41E-05	2.25E-05	1.18E-05	60%	-16%
Fe	1.27E-06	1.38E-06	1.14E-06	9%	-11%
Cu	1.43E-06	1.53E-06	1.32E-06	7%	-8%
Cl	1.80E-05	1.90E-05	1.67E-05	6%	-7%
Mn	8.61E-07	9.22E-07	8.24E-07	7%	-4%
Ar	1.85E-05	1.87E-05	1.81E-05	1%	-2%
S	2.98E-05	2.99E-05	2.93E-05	0%	-2%
Ca	2.06E-05	2.07E-05	2.03E-05	0%	-2%
Zn	1.84E-05	1.85E-05	1.82E-05	0%	-1%
P	1.42E-04	1.42E-04	1.41E-04	0%	0%
K	7.42E-04	7.42E-04	7.40E-04	0%	0%

B	***BASELINE CORRECTED DATA***		
	REGULAR	**POSITIVELY CONSTRAINED**	**PERCENT CHANGE**
Element:	***(f)*** **CELL - BKGD**	***(g)*** **CELL - BKGD**	**(h = [f-g]/f)** **BKGD CORRECTED**
Si	-1.38E-06	-1.38E-06	0%
Fe	1.75E-06	1.74E-06	0%
Cu	2.17E-06	2.17E-06	0%
Cl	2.03E-05	2.03E-05	0%
Mn	1.16E-06	1.15E-06	0%
Ar	1.42E-05	1.42E-05	0%
S	3.23E-05	3.23E-05	0%
Ca	1.92E-05	1.92E-05	0%
Zn	2.77E-05	2.77E-05	0%
P	1.67E-04	1.67E-04	0%
K	9.51E-04	9.51E-04	0%

Table III.1 Use of Positivity Constraints: Comparison of mean cellular counts per second normalized by the upstream ion chamber solved with and without positive constraints. (A) The first two columns of data from the left correspond to the mean cellular counts per second fit without positive constraints and with positive constraints, respectively. The third column corresponds to the fitted data using positivity constraints and is reflective of the mean counts per second for cell pixels minus the mean counts per second for background pixels; since the data is already corrected for with a blank, this should not be necessary. The fourth and fifth columns show the difference in quantitation between columns 2 and 1 and columns 3 and 1, respectively. (B) The same comparison as in A except the data was baseline corrected using a snipping function (Section III.3.2).

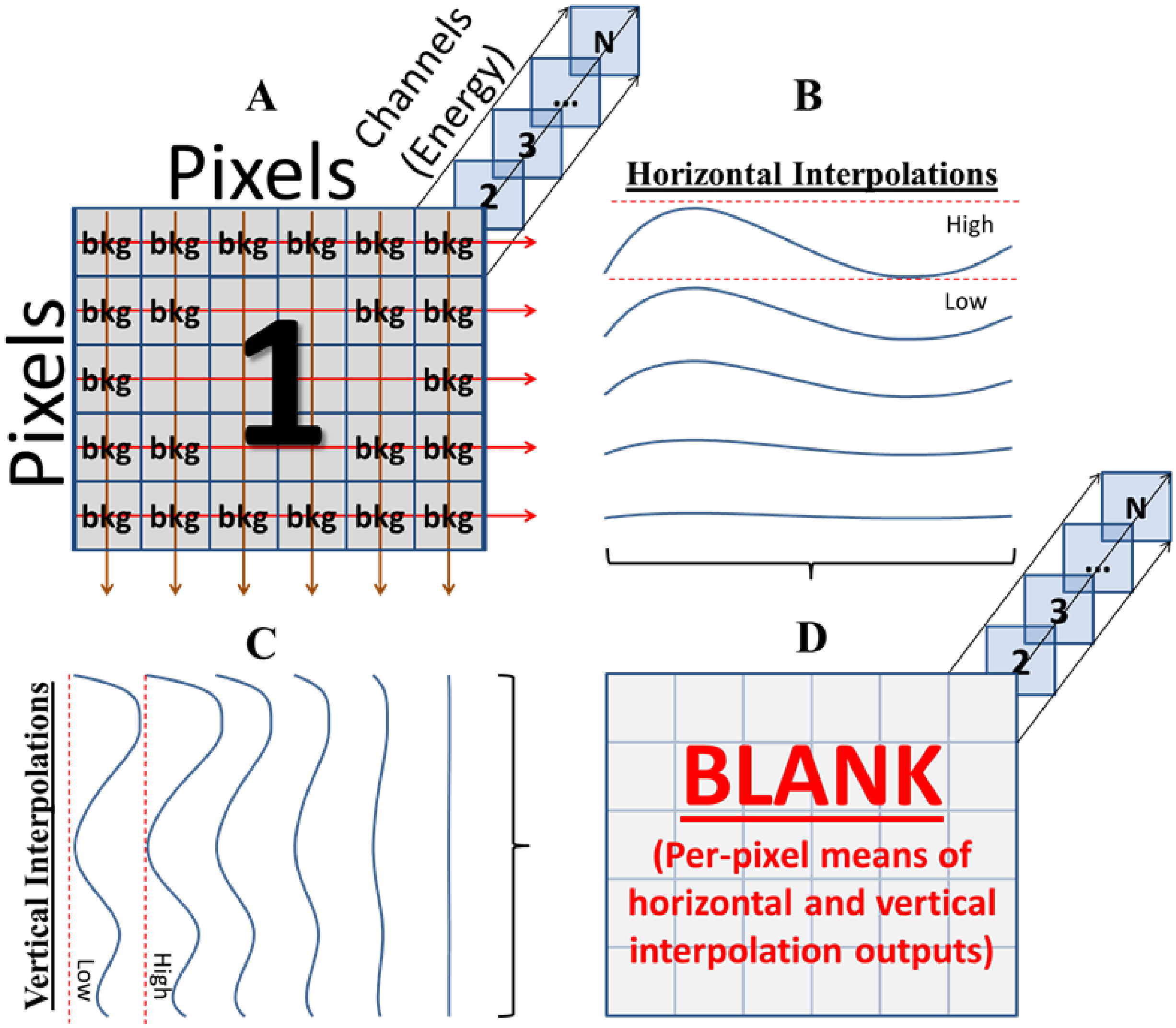

Figure III.2 Interpolation of 2D Blanks: Interpolation is performed using each channel of the raw data (A) to create horizontal (B) and vertical (C) interpolations of the values for the associated channel across the image. The value for each pixel of the blank (D) is calculated from the mean of the corresponding indices from the horizontal (B) and vertical (C) interpolations.

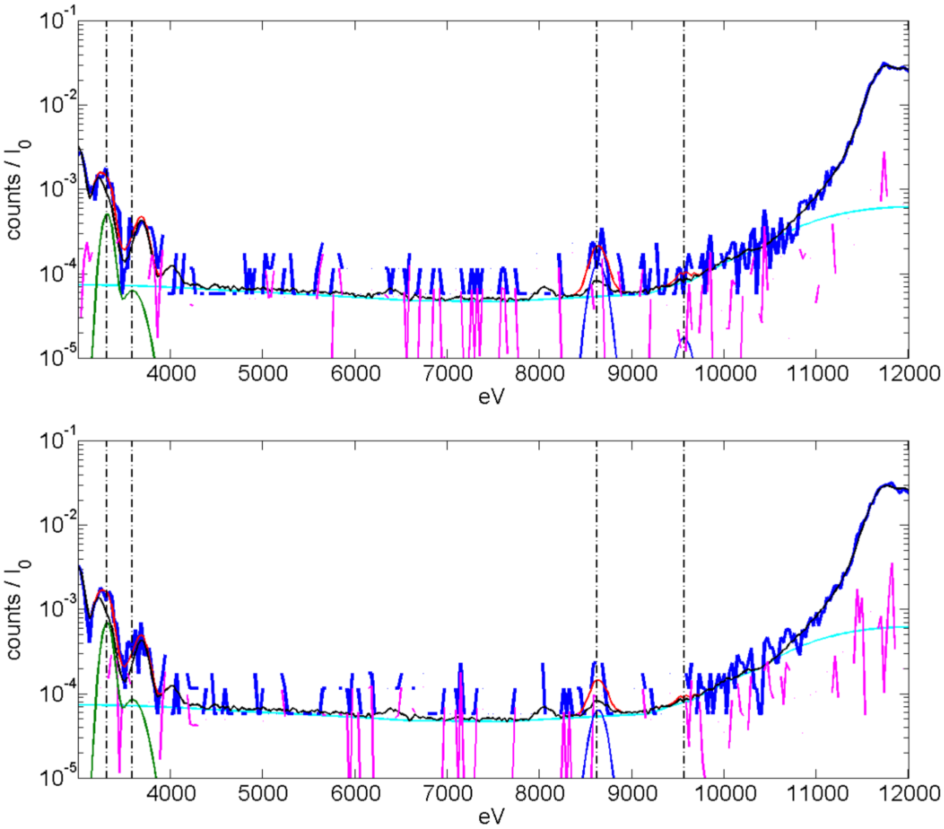

Figure III.3 Inherent Noise at the Individual Pixel Level: Sample spectra from individual pixels from the first flow cytometer data set. The dark blue lines with gaps are the normalized fluorescence counts; the gaps are caused by zero counts due to the log scale of the images. The red line is the fit to the data. The black line is the calculated blank. The cyan is a baseline from a modified snipping function and the magenta is the residual. The dark green and dark blue lines coming from the bottom of the images are the fitted peaks for K and Zn, respectively.

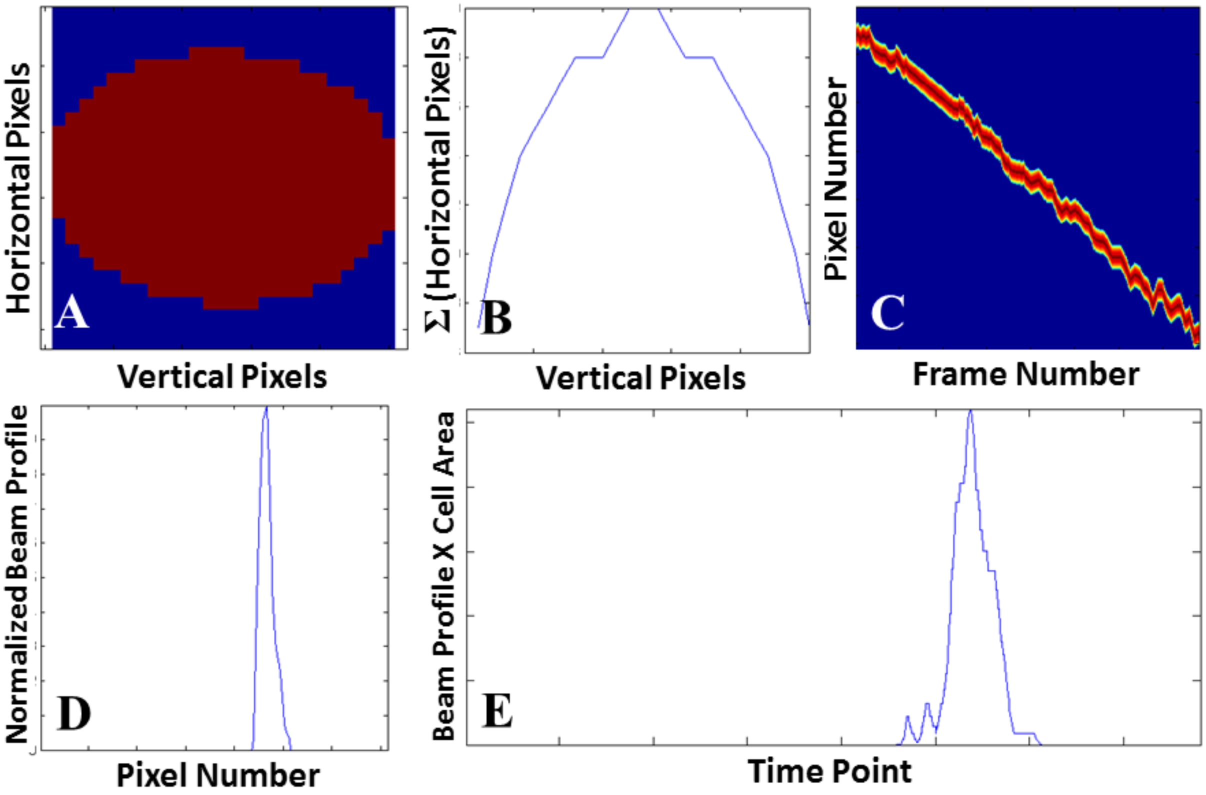

Figure III.4 Construction of an Ellipse Based CAIBT: (A) The binary mask of an ellipse. (B) The vertical profile of the ellipse obtained by summing horizontally across the mask of the ellipse. (C) Positioned ellipse profile array – this array has the profile placed along the path of the capillary. The profile's placement is determined by the reported centroid of the associated cell for the associated frame. The x axis corresponds to frame number and the y-axis corresponds to the vertical coordinates of the capillary. (D) The vertical beam profile. (E) The convolution obtained by multiplying the transpose of C [MxN] by D [Mx1].

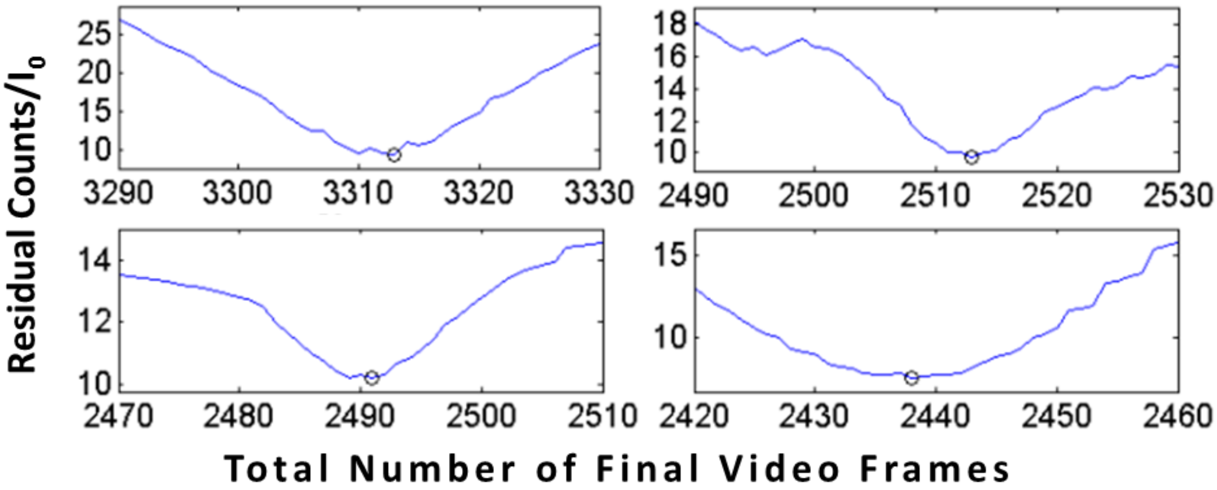

Figure III.5 Refinement of frame rate and offset during alignment of the video data with the XRF: The refinement of frame rate and offset done iteratively for each tested video rotation and beam profile shift when pairing the CAIBT with the XRF data. The y-axis is the summed residual of each alignment, and the x-axis is the final number of video frames to which the original video data was contracted.

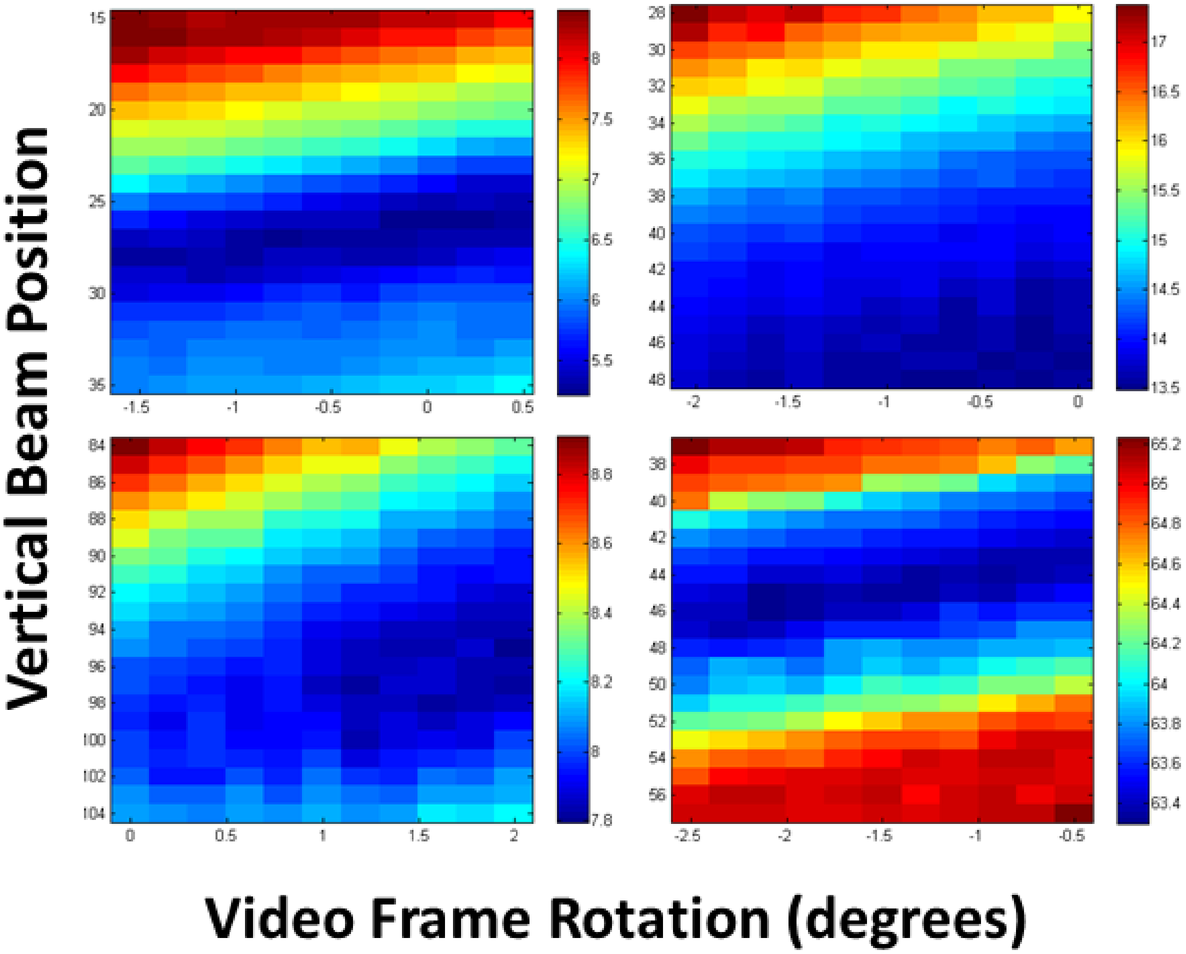

Figure III.6 Optimizing Beam Position and Video Rotation: The four images above are representative alignment grids resulting from the refinement of the beam profile position and the video rotation obtained while aligning the video data with XRF.

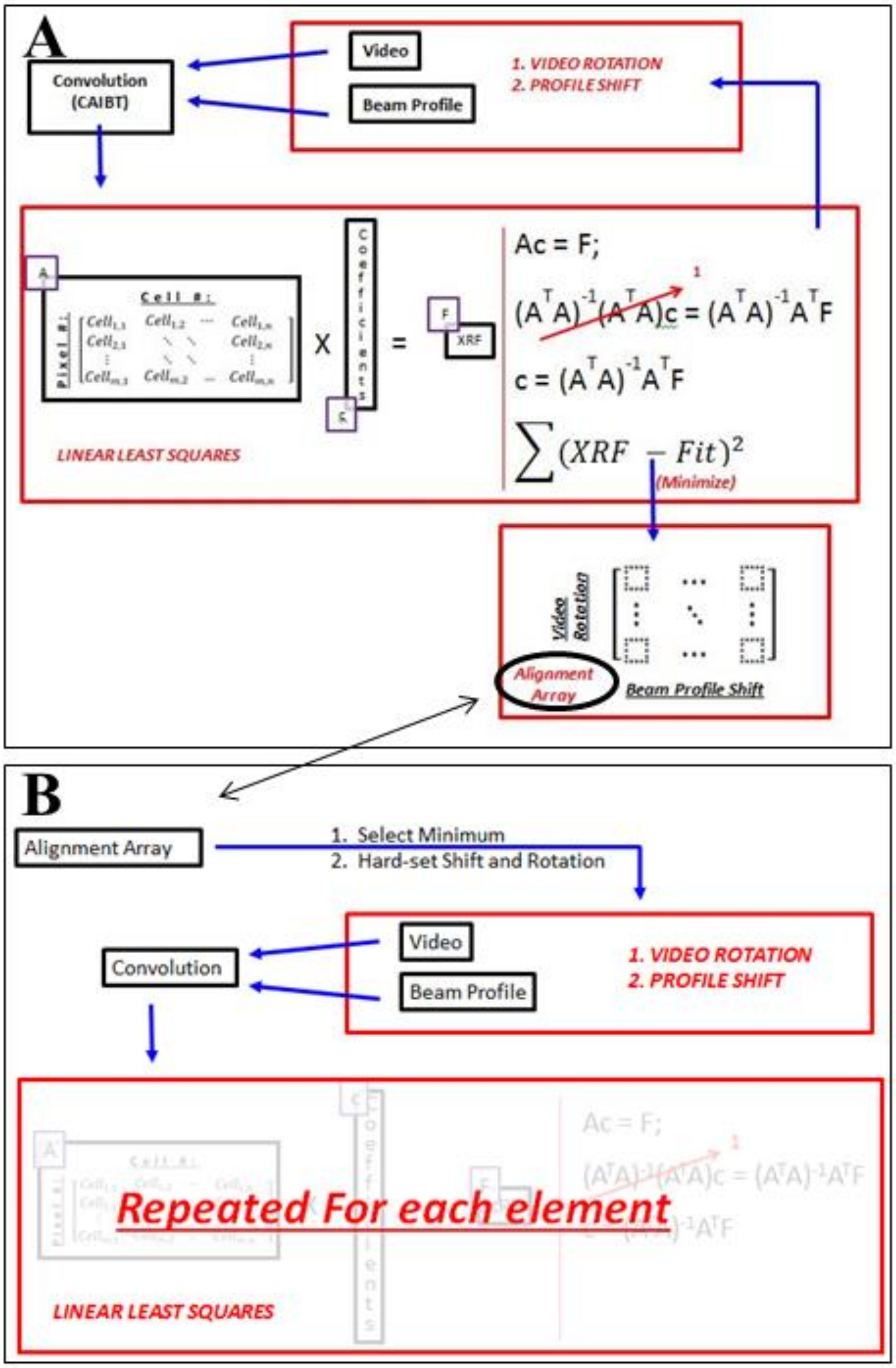

Figure III.7 Iterative refinement of aligning the XRF and video data: After the alignment grid of (A) is completed, the values for the rotation and shift are set to the grid values that correspond to the smallest residual. These are then used to solve for each element of the cells from the flow cytometer data set. The Alignment grid is graphically represented in Figure III.6.

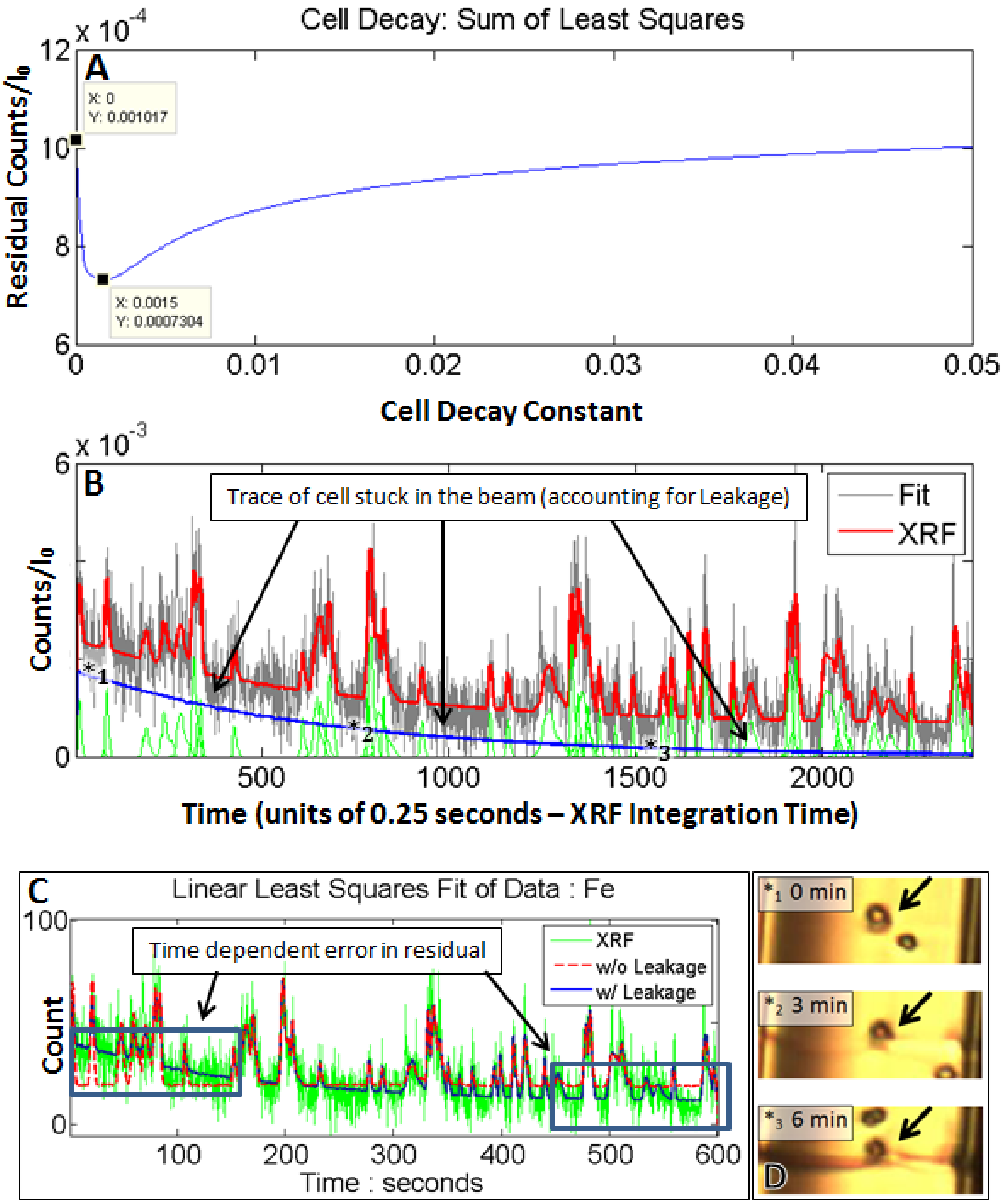

Figure III.8 Accounting for Cell Leakage: (A) The sum of the least squares associated with the different values for cell leakage. (B) The resultant fit based on the minimum of A. (C) An overlay of the total fits to the raw XRF when leakage is and is not accounted for. (D) Snapshots of the cell in the beam at the time points corresponding to the asterisks in B.

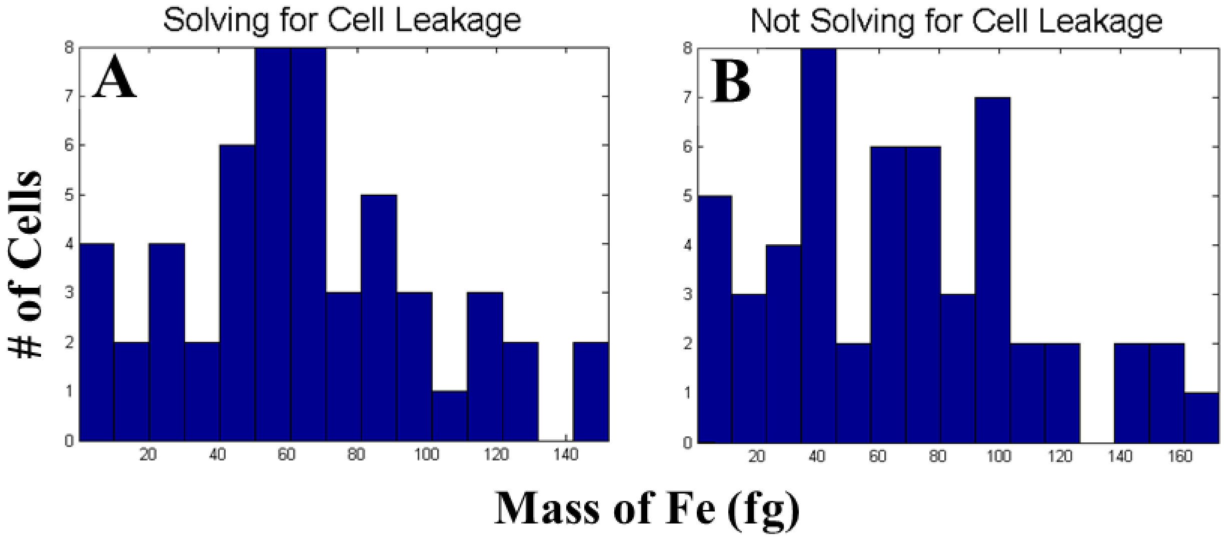

Figure III.9 Histograms: The histograms of solved RBC Fe masses (A) solving for Cell Leakage and (B) neglecting Cell Leakage. These show the expected increase in the distribution width of the masses that occurs with the time dependent variations in the residuals (Figure III.8) when cell leakage is not accounted for.

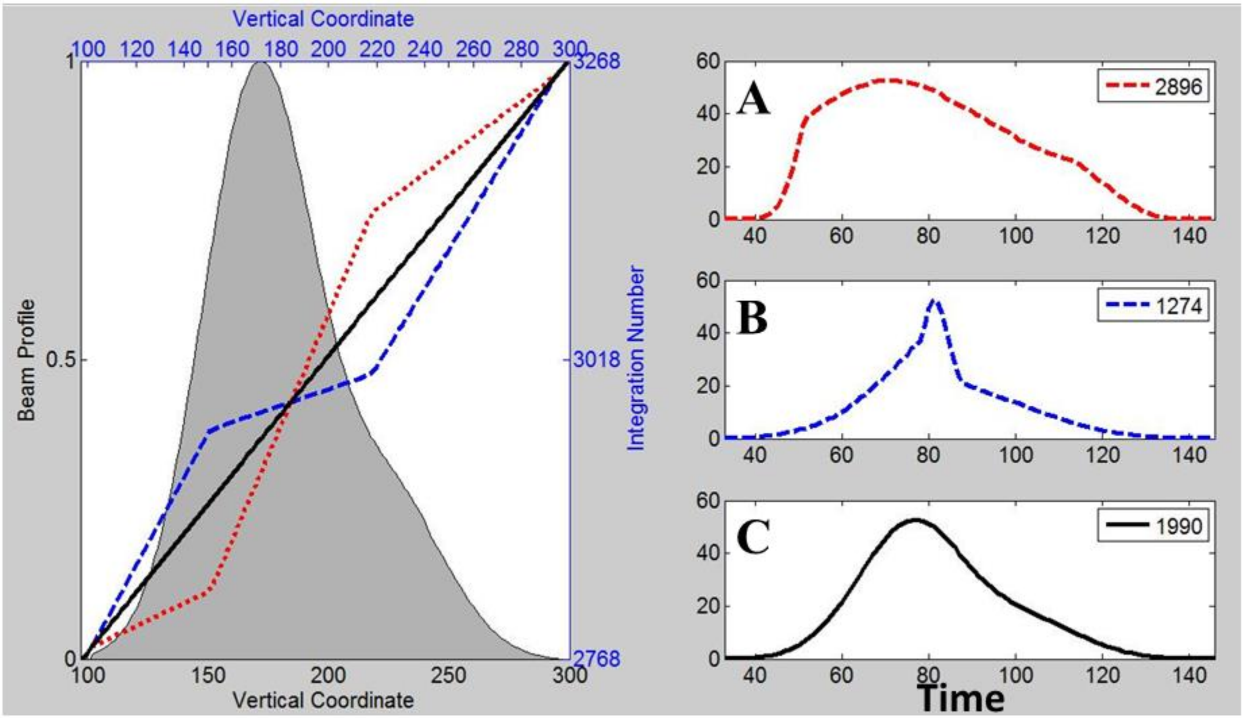

Figure III.10 Schematic illustration of the effect of non-ideal cell travel through the beam: (Left) The beam profile is plotted with 3 representative cell paths through the beam. The axes are the normalized beam profile (left-y), the vertical coordinates along the cells path through the beam (top/bottom-x), and the integration/time (right-y). The black path corresponds to an ideal path in which the velocity of the cell remains constant. The blue path corresponds to a path in which the cell speeds though the hotspot of the beam; the red trace corresponds to a path in which the cell slows down in the hotspot of the beam. Plots A, B, and C are the corresponding traces obtained by convolving the cell profile with the beam profile. Note that the total integrated counts (listed in the upper right corners of A, B, and C) vary between 65% and 145% the true value.

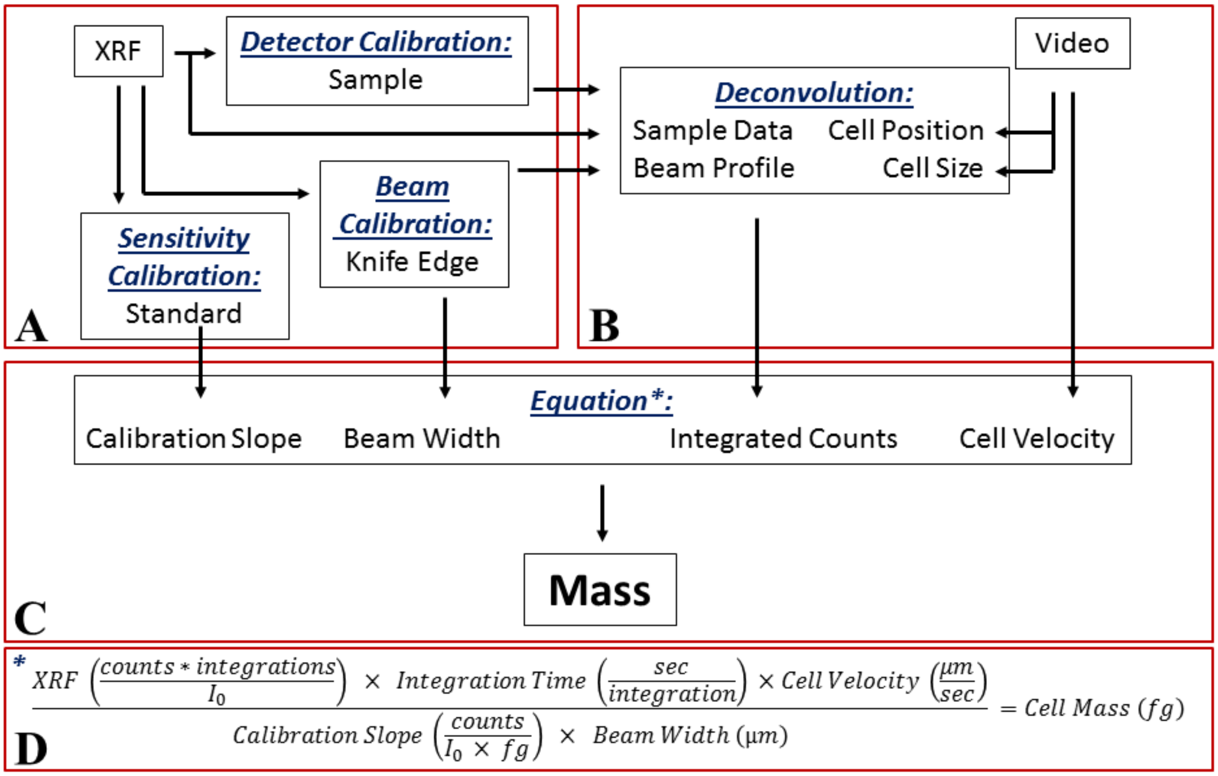

Figure III.11 The complete flow for processing and quantifying XRF flow cytometer data: Initial parameters are calibrated directly from a blank corrected sample scan. This yields better results.

III.8 REFERENCES

1. Janssens, K., et al., *Accurate evaluation of μ-PIXE and μ-XRF spectral data through iterative least squares fitting.* Nuclear Instruments and Methods in Physics Research Section B: Beam Interactions with Materials and Atoms, 1996. **109–110**(0): p. 179-185.
2. Brunetti, A. and T.J. Steger, *X-Ray spectra background fitting by projection onto convex sets.* Nuclear Instruments & Methods in Physics Research Section a-Accelerators Spectrometers Detectors and Associated Equipment, 2000. **441**(3): p. 504-509.
3. McClanahan, T., J. Trombka, and M. Loew, *Automated spectroscopy of X-ray and gamma-ray pulse height spectra using energy space subdivision.* Nuclear Instruments & Methods in Physics Research Section a-Accelerators Spectrometers Detectors and Associated Equipment, 2005. **546**(1-2): p. 176-179.
4. Brunetti, A., *A fast fine-grained genetic algorithm for spectrum fitting: An application to X-ray spectra.* Computer Physics Communications, 2013. **184**(3): p. 573-578.
5. Yi, L.T., et al., *A new background subtraction method for energy dispersive X-ray fluorescence spectra using a cubic spline interpolation.* Nuclear Instruments & Methods in Physics Research Section a-Accelerators Spectrometers Detectors and Associated Equipment, 2015. **775**: p. 12-14.
6. Meijering, E., et al., *Tracking in cell and developmental biology.* Seminars in Cell & Developmental Biology, 2009. **20**(8): p. 894-902.
7. Bounakhla, M. and M. Tahri, *X-Ray Fluorescence Analytical Techniques*.
8. Verma, H.R., *Atomic and Nuclear Analytical Methods XRF, Mossbauer, XPS, NAA and Ion-Beam Spectroscopic Techniques*. 2007.
9. Van Grieken, R.E. and A.A. Markowicz, *Handbook of X-Ray Spectrometry*. 2 ed. Practical Spectroscopy. 2002: Marcel Dekker.
10. Krause, M.O., *Atomic Radiative and Radiationless Yields for K and L Shells.* Phys. Chem. Ref. Data, 1979. **8**(2): p. 307-327.
11. Thompson, A., et al., *Center for X-Ray Optics and Advanced Light Source: X-Ray Data Booklet*. 3 ed. 2009.
12. Krause, M.O. and J.H. Oliver, *Natural Widths of Atomic K and L Levels, Kα X-Ray Lines and Several KLL Auger Lines.* J. Phys. Chem. Ref. Data, 1979. **8**(329).
13. Hubbell, J.H., et al., *A Review, Bibliography, and Tabulation of K, L, and Higher Atomic Shell X-Ray Fluorescence Yields.* J. Phys. Chem. Ref. Data, 1994. **23**(339).
14. 2015; X-ray transmission of a gas]. Available from: http://henke.lbl.gov/optical_constants/gastrn2.html.
15. *Chemical Composition of Zeonor*. Available from: http://www.matweb.com/search/datasheet.aspx?matguid=40352960137649239cf299bb62289a63&ckck=1.
16. Kahoul, A., et al., *K-shell fluorescence yields for elements with 6 <= Z <= 99.* Rad. Phys. and Chem., 2011. **80**: p. 369–377.
17. *Mucal Program by P. Bandyopadhyay and C.U. Segre*. 19-Dec-2014]; Available from: www.csrri.iit.edu/mucal.html.
18. *Photoionization Cross Sections*. Available from: http://www.pa.uky.edu/~verner/photo.html.
19. Herrero , S. and J. Bescós, *Background Subtraction Techniques: Systematic Evaluation and Comparative Analysis*. Vol. 5807. 2009.

CHAPTER IV: X-RAY FLUORESCENCE FLOW CYTOMETER: REDESIGN AND IMPROVEMENTS[3]

IV.1 INTRODUCTION

Cells have complex homeostatic mechanisms that maintain elemental concentrations of bulk, trace and ultra-trace elements. Certain elemental concentrations are perturbed under various conditions and disease states. Since homeostatic deviations can be clinically diagnostic

---

[3] The staff of the LSA Scientific Instruments Shop provided valuable collaboration on the redesign of the sample older design. Aniruddha Deb provided project guidance. Jim Penner-Hahn provided invaluable collaboration towards the developed methodologies. Tsz Kwan Yim and Claire Kozemchek both participated in capillary experiments and with data collection at APS. Erik Guetschow provided invaluable collaboration for capillary flow manipulation and conceptual development of the syphon pump. Lubomir Dostal cultured *Saccharomyces cerevisiae* cells for analysis at APS. This research was supported by NSF IDBR-0852802. This research used resources of the Advanced Photon Source, a U.S. Department of Energy (DOE) Office of Science User Facility operated for the DOE Office of Science by Argonne National Laboratory under Contract No. DE-AC02-06CH11357. "This project was supported by grant 9 P41 GM103622 from the National Institute of General Medical Sciences of the National Institutes of Health." The content is solely the responsibility of the authors and does not necessarily reflect the official views of the National Institute of General Medical Sciences or the National Institutes of Health.

for disease states, knowledge of cellular concentrations under different conditions is very important. Furthermore, homeostatic mechanisms governing the metallome are interconnected and a change in one regulatory process can impact others [1-8]. As such, characterization of the "metallome" is very important. However, due to the immense amount of heterogeneity across a population of cells [6, 9-13], to truly understand homeostatic responses of the metallome it must be characterized at the single cell level. As such, there is a pressing need for a high through-put technique capable of elemental analysis of single cells as discussed in Chapter 1.

Chapter 2 described the first generation of an XRF flow cytometer to address that need. Capillary action was used to load cells into an (100 µm o.d., 50 µm i.d.) acrylic capillary and a trapped air pocket is then used to control the transport of cells at a fixed vertical velocity past a focused (50 µm horizontal × 20 µm vertical) x-ray beam. X-ray fluorescence was used to determine the mass of metal in each cell, and single-cell measurements were used to directly measure population heterogeneity for metals in the µM to mM concentration range.

While those results were promising, they did not have sufficient sensitivity for most elements. This chapter describes a redesigned and improved instrument. In this work, I have increased the solid angle of detection, decreased the background, changed the capillary to reduce scatter and contaminant levels, and addressed the effect of the horizontal beam profile on the observed population distribution of elemental masses. Increasing the solid angle of detection increases the strength of the detected fluorescence signals, allowing for data collection at greater count rates, and thus permitting lower detection limits [14, 15]. Increasing the solid angle while decreasing the size of the capillary will increase the total collected counts while decreasing the portion of those counts from the background.

In the initial instrument, the beam was treated as horizontally homogenous. In practice it is difficult to prepare a perfectly uniform beam due to the X-ray optical components (monochromator crystals, X-ray mirrors, absorbing filters). Even if perfectly aligned, these will give some structure to the beam, and any misalignment can give significant asymmetry [16]. In order to address non-uniformity in the horizontal profile, we added a second camera, allowing cells to be localized in two dimensions.

IV.2 EXPERIMENTAL

IV.2.1 SAMPLE PREPARATION AND HANDLING

Red blood cell experiments were performed using trypsinized bovine red blood cells (bRBCs, 0.1 hematocrit, obtained from Lampire), diluted 1:20 using phosphate buffered saline (PBS – obtained from Fisher Scientific). When not used, the stock and the diluted aliquots were kept at 4˚C. Yeast experiments were performed using the *Saccharomyces cerevisiae* yeast strain BY4741, grown in YPD rich media at 30 C˚ overnight. Cells were transported to APS in YPD media, stored at 4 C˚ and washed with PBS prior to measurement.

IV.2.2 IMPROVED INSTRUMENT DESIGN

The improved instrument is illustrated in Figure IV.**1**. A second camera and detector have been added to allow better determination of cell position. Each detector has been equipped with a Mo collimator to decrease detected scatter from the hutch [17]. The distance between each detector is 2.8 cm with a clearance for the sample holder of 1.4 cm. The detector to the capillary center-to-center distance was decreased from 25 mm to 14 mm giving ~2-fold increase in the solid angle.

If the only constraint was solid angle, the optimum sample-detector distance would be 7 mm (4-element detector, Vortex® model 267-VTX-ME4) or zero (1-element detector), as shown in **Figure IV.2**A. Given the constraints of the geometry along with the sterics of the instrument, we were unable to move each detector any closer than 14 mm if the detector remains perpendicular to the beam. Moving it closer would have blocked the cameras and caused an unacceptable increase in Compton scatter. Rotating the detector would allow the detector to be closer, but would significantly increase the scatter, which is proportional to φ where φ is the angle between the beam polarization and the detector. Moreover, when perpendicular, the distance that gives the greatest solid angle also gives a signal almost entirely dominated by Compton scatter due to the deviation from the polarization direction (Figures 0B, C). At 2.5 cm (the distance used for our first instrument) the range of cosφ is ~0.2-0.5; moving closer to a distance of 1.4 cm increases this to ~0.3-0.65 (**Figure IV.2**D) and increases solid angle ~ 2-fold (Figures 0A, C).

Additionally, the sample holder has also been modified and encases the capillary in a He shroud.

IV.2.3 CHANGES IN CAPILLARY SIZE AND MATERIAL

The capillary material used previously contained contaminants of Fe, K, Zn, and Cu. In an effort to decrease contamination, we explored a variety of capillary materials (see **Figure IV.3**). Unfortunately the hydrophilic material (polycarbonate and polymethylmethacrylate) both had high levels of biologically relevant metals. Fortunately, two hydrophobic polymers, Zeonor® and Zeonex®, had relatively low levels of contaminants. Zeonor® was chosen as our new capillary material.

IV.2.4 SYPHON PUMPING

Because of the switch to a hydrophobic capillary, we were no longer able to load the capillaries using capillary action. Instead, we used a syringe to initially load the cells and establish a syphon pump for final control of cellular velocity. To establish the syphon pump, pipette tips were filled with a PDMS mixture using a 10% crosslinking agent. After curing, an 18 gauge hypodermic needle was used to pierce the PDMS. The capillary was inserted into the hypodermic needle and the PDMS carefully slid down to seal the two together. The opposite end of the capillary was then placed into a cuvette holding our sample. The hypodermic needle was then attached to a 10 mL syringe and negative pressure was used to pull the sample through the capillary until the entire length of the capillary was filled. Once the full length of the capillary was loaded, the end attached to the syringe was brought to a relative height lower than the sample cuvette at the loading end of the capillary. The capillary was then cut using a fresh 0.09 mm razor blade and inserted into a second sample holder for receiving. This formed the syphon pump. It is important to make sure the end of the capillary is always at a lower relative height than the loading end until the syphon has been established to make sure no air enters into the capillary.

The syphon pump allows precise control of cell velocity as shown in Figure IV.**4**. As expected, velocity increased with Δh, due to hydrostatic pressure. Since capillary resistance scales as the inverse of the square of the radius, a capillary with 25 μm inner diameter shows approximately a 4-fold decrease in velocity compared to a 50 μm inner diameter.

Data were measured using capillaries with i.d. 25 μm and o.d. 50 μm and capillaries with i.d. 15.5 μm and o.d. 31 μm.

IV.2.5 XRF DATA

Though our design accommodates two detectors, only one detector was available. As such, XRF spectra were collected using a single 4-element energy resolved solid state detector (Vortex-ME4, SII NanoTechnology). Fluorescence counts were normalized to the intensity measured with a N_2 filled ion chamber. The x-ray beam was focused to 24.1 µm horizontal x 6 µm vertical (FWHM) using a pair of Kirkpatrick-Baez (KB) mirrors [18], with the precise beam profile determined by a knife edge scan.

Data were analyzed as described in Chapter 3.

IV.2.6 POSITIONING CELLS ALONG HORIZONTAL PROFILE OF THE BEAM

The influence of the horizontal profile of the beam on the observed distribution of Fe masses in RBCs was assessed by using the two cameras to determine the x-position of each cell. The two videos corresponding to each XRF data set were aligned separately with the XRF data. The masses of the associated elements were deconvolved yielding two mass answers for each element of each data set that were then averaged; the mean percent difference between the two values from each camera and the calculated mean masses was < 10%. For each aligned video and XRF, the x-position for each cell through the beam was calculated as the mean x-position of that cell's path through the beam. For 5 RBC scans, the two sets of x-positions were then used to calculate the x-coordinate of each cell (see Figures 1B, C).

IV.2.7 Mo COLLIMATOR

The Mo collimator presented a new problem that we were unable to address in this work. Due to it being a point source filter, precise positioning of both detectors is necessary. This may seem obvious; however, the set up at the beamline did not allow for this and we were forced to position the detectors by hand and then fix them in place to the optical table with clamps. This was hardly precise or accurate given the fact that the device schematics call specifically for a center-to-center detector-sample distance of 14 mm with a 90-degree angle to the incident beam.

IV.3 RESULTS

IV.3.1 RBC SCANS

In data set 1, twelve scans each of 10 minutes, were made on RBC samples with different cell densities. A total of 131 RBCs were detected. The measured masses for Fe, K, and Zn were 49.8 ± 29.7 fg (in agreement with data from the first instrument, Chapter 2), 15.7 ± 14.7 fg, and 0.37 ± 0.3 fg, respectively. At the highest cell densities, we were able to interrogate 73 cells in a single 10 minute scan. In that scan we were able to detect S with a mass of 22.5 ± 22.7 fg. The masses for Fe, K, and Zn from that single 10 minute scan were 46 ± 33.1 fg, 10.6 ± 13.4 fg, and 0.27 ± 0.27 fg, respectively. Importantly, the increased concentration of the sample (and therefore, increased overlap) doesn't appear to have affected the population distributions.

Figure IV.6 shows the blank corrected mean spectrum of all cell time points from the RBC scan analyzed in **Figure IV.7**. It clearly demonstrates that we see S, K, Fe, and Zn in RBCs. In **Figure IV.7**A, some of the peaks present across all four channels are boxed in red; the one containing the asterisk is represented by the blank subtracted XRF spectrum in **Figure IV.7**B.

As a statistical justification for **Figure IV.6** and **Figure IV.7** A, B, and C, a two-tailed t-test was performed. The cell and background time points were separated according to the methodologies discussed in chapter 3. The pixels of each group were then organized into a P x C array where P is pixel number and C is detector channel. A two-tailed t-test was performed, comparing each of the 1…C columns of the cell and background arrays against one another. A p-value of less than 0.001 was used as the statistical cut off with the additional constraint that channels presenting statistically significant p-values also needed to be contiguous with at least one other channel presenting a statistically significant p-value. The p-values were then subtracted from 1 and plotted as a function of energy (**Figure IV.7**D). If a peak appears in this plot in an energy range corresponding to a p-value less than 0.001, it is likely that we are able to see a corresponding fluorescence peak over that same energy range in blank corrected XRF spectrum in **Figure IV.7**B.

IV.3.2 YEAST SCANS

Two scans each of 10 minutes were attempted on yeast samples with different cell densities allowing us to interrogate 18 cells. These cells showed Zn, Fe, and K with mean content of 0.57 ± 0.61 fg, 0.62 ± 0.45 fg, and 37.1 ± 41.5 fg, respectively.

Figure IV.8 shows the blank corrected mean spectrum of all cell time points from one of the yeast scans analyzed in **Figure IV.9**. It clearly demonstrates that we see S, K, and Zn in yeast. In **Figure IV.9**A, some of the peaks present in both the Fe and Zn channels are boxed in red; the one containing the asterisk is represented by the blank subtracted XRF spectrum in **Figure IV.9**B. Similar to the RBC scans, the cell and background time points were separated, and a two-tailed t-test was performed comparing each of the 1…C columns using the same constraints and p-value cut off (**Figure IV.9**D).

IV.3.3 EFFECT OF HORIZONTAL POSITION

The Fe masses are plotted as a function of the x-coordinate of each cell in **Figure IV.10**, together with the experimentally determined horizontal beam profile. This shows that our positioning, and our ability to maintain the position, of the capillary in the beam were imperfect since the cells cover an x-range of ~40 μm, while the capillary i.d. was nominally 25 μm.

IV.3.4 HELIUM SHROUD

To test the He shroud we scanned an empty capillary both with and without the shroud in place. The spectra, normalized to I0, are presented in **Figure IV.11**. The total counts decreased by ~84% when using the He shroud, reflecting the decrease in the total scatter. Particularly striking is the decrease in Ar fluorescence.

IV.4 DISCUSSION

On a single cell basis, the improved instrument gives a much better determination of the distribution of masses for each element. Those distributions are presented in **Figure IV.12** with the various combinatorial correlation plots presented in Figure IV**.13**. Importantly, based solely on counting statistics, the mean absolute error for K, S, Zn, and Fe are 1.0 fg, 3.3 fg, 0.38 fg, and 0.86 fg, respectfully; this gives percent errors of 6.3% 14%, 10%, and 1.7%, respectfully. This shows almost a 4.5-fold improvement in signal quality over the first instrument (Chapter 2). The Fe:Zn ratio matches literature values [19-21]. The apparent Fe:K ratio is 100-fold higher than the literature value [22]; this may reflect an underestimation of K caused by the need to extrapolate the calibration factor from the elements measured all the way down to K. Unfortunately, we had not expected to be able to detect K and it was therefore not included in our standards.

With two cameras we were able to demonstrate that the apparent Fe concentration in bRBCs is not reliable. The impact of horizontal deviation of the capillaries/cells from the center of the profile on quantitation is uncertain; however, any impact will almost certainly register a population mean less than the true mean and a population distribution greater than the true distribution. This can be understood by analyzing cell 'a' in **Figure IV.10**. Cell 'a' at ~22 fg is positioned right on the line for the beam profile. What this means is that had cell 'a' been at an x-position of ~90 rather than ~66 it would have registered as having a mass closer to ~82 fg, the mass value of the left y-axis that corresponds to the beam profiles maximum value.

In addition to the data collected for the RBCs, we've also been able to measure the elemental composition of yeast. Although these data are less impressive, that's not surprising given the lower total content of metals in yeast. Additionally, if there is a horizontal dependence to apparent quantitation, this might explain the increased difficulty associated with obtaining a yeast signal as deviations from the maximum intensity at the center of the beam could, in theory, cause the signal to drop below detection limits.

Interestingly, comparison of data obtained from an empty capillary with and without the He shroud showed the disappearance of a very strong peak at Mn. Importantly, **Table IV.1** shows the removal of almost all background Al, Si, Ar, Mn, Ni, Cr, S, Cl, P, and K signals.

IV.5 Conclusions

The smaller capillaries (25 μm id, 50 μm od) allowed us to detect more elements. We have significantly improved the signal-to-noise ratio for Fe in bRBCs from 41 to 119 for a spectrum sum of all cells in a scan. Additionally, we are now able to see S, K, and Zn in bRBCs with associated signal-to-noise ratios of 3, 2, and 6.5, respectively. The agreement of both Fe and Zn with literature is very important as these elements were part of the calibration standards. Inclusion of K and S in future standards is paramount. In terms of yeast, we have been able to attain multielement (albeit, only two – K, and Zn) detection capabilities. Collectively, these results show promising potential for the future development of the cytometer to explore the cellular metallome.

With the benefit of two cameras, we were able to characterize the position of the capillary in the beam. This demonstrates that at least a portion of the apparent variability in Fe mass is due to variation in position. Future developments should correct for variable positioning of the capillary relative to the horizontal profile or widen the beam and insure a uniform profile. Future work should aim at encasing the entire instrument, including the detectors, inside a He chamber. Additionally, the Mo collimator should be defocused from a point source to a source slightly larger than the outer diameter of the capillary and each detector should be positioned using electronically controlled stages x-, y-, z-, and rotary stages.

IV.6 REFERENCES

1. Arino, J., J. Ramos, and H. Sychrova, *Alkali Metal Cation Transport and Homeostasis in Yeasts.* Microbiology and Molecular Biology Reviews, 2010. **74**(1): p. 95-+.
2. Bertinato, J. and M.R. L'Abbe, *Maintaining copper homeostasis: regulation of copper-trafficking proteins in response to copper deficiency or overload.* Journal of Nutritional Biochemistry, 2004. **15**(6): p. 316-322.
3. Chillappagari, S., et al., *Copper Stress Affects Iron Homeostasis by Destabilizing Iron-Sulfur Cluster Formation in Bacillus subtilis.* Journal of Bacteriology, 2010. **192**(10): p. 2512-2524.
4. Dann, C.E., et al., *Structure and mechanism of a metal-sensing regulatory RNA.* Cell, 2007. **130**(5): p. 878-892.
5. Dlouhy, A.C. and C.E. Outten, *The Iron Metallome in Eukaryotic Organisms*, in *Metallomics and the Cell*, L. Banci, Editor. 2013, Springer: Dordrecht. p. 241-278.
6. Eide, D.J., *Homeostatic and Adaptive Responses to Zinc Deficiency in Saccharomyces cerevisiae.* Journal of Biological Chemistry, 2009. **284**(28): p. 18565-18569.
7. Pagani, M.A., et al., *Disruption of iron homeostasis in Saccharomyces cerevisiae by high zinc levels: a genome-wide study.* Molecular Microbiology, 2007. **65**(2): p. 521-537.
8. Zhao, H., et al., *Regulation of zinc homeostasis in yeast by binding of the ZAP1 transcriptional activator to zinc-responsive promoter elements.* Journal of Biological Chemistry, 1998. **273**(44): p. 28713-28720.
9. Davey, H.M. and D.B. Kell, *Flow Cytometry and Cell Sorting of Heterogeneous Microbial Populations: The Importance of Single-Cell Analyses.* Microbiological Reviews, 1996. **60**(4): p. 641-696.
10. Kalisky, T. and S.R. Quake, *Single-cell genomics.* Nature Methods, 2011. **8**(4): p. 311-314.
11. Musat, N., et al., *A single-cell view on the ecophysiology of anaerobic phototrophic bacteria.* Proceedings of the National Academy of Sciences of the United States of America, 2008. **105**(46): p. 17861-17866.
12. Leslie, M., *The Power Of One*, in *Science*. 2011. p. 24-26.
13. Brehm-Stecher, B.F. and E.A. Johnson, *Single-Cell Microbiology: Tools, Technologies, and Applications.* Microbiology and Molecular Biology Reviews, 2004. **68**(3): p. 538-559.
14. Ryan, C.G., et al., *Elemental X-ray imaging using the Maia detector array: The benefits and challenges of large solid-angle.* Nuclear Instruments and Methods in Physics Research Section A: Accelerators, Spectrometers, Detectors and Associated Equipment, 2010. **619**(1-3): p. 37-43.
15. Sun, Y., et al., *Optimizing detector geometry for trace element mapping by X-ray fluorescence.* Ultramicroscopy, 2015. **152**: p. 44-56.

16. Bewer, B., *Quantification estimate methods for synchrotron radiation X-ray fluorescence spectroscopy.* Nucl. Instruments Methods Phys. Res. B 2015. **347**: p. 1-6.
17. Behne, E.A., et al., *A compact point focusing spatial filter for x-ray fluorescence and inelastic x-ray scattering studies.* Review of Scientific Intruments, 2001. **72**(3908).
18. Kirkpatrick, P. and A.V. Baez, *FORMATION OF OPTICAL IMAGES BY X-RAYS.* Journal of the Optical Society of America, 1948. **38**(9): p. 766-774.
19. Kakkar, N. and M. Makkar, *Red Cell Cytograms Generated by an ADVIA 120 Automated Hematology Analyzer: Characteristic Patterns in Common Hematological Conditions.* Lab Medicine, 2009. **40**(9): p. 549-555.
20. Herring, W.B., et al., *Trace Metals in Human Plasma and Rd Blood Cells: A Study of Magnesium, Chromium, Nickel, Copper, and Zinc I. Observations of Normal Subjects.* American Journal of Clinical Nutrition 1960. **8**: p. 846-854.
21. Herring, W.B., et al., *Trace Metals in Human Plasma and Rd Blood Cells: A Study of Magnesium, Chromium, Nickel, Copper, and Zinc II. Observations of Patients with Some Hematologic Diseases.* American Journal of Clinical Nutrition, 1960. **8**: p. 855-863.
22. Shamberger, R.J., *Calcium, Magnesium, and Other Elements in the Red Blood Cells and Hair of Normal Patients with Premenstrual Syndrome.* Biological Trace Element Research, 2003. **94**: p. 123-129.

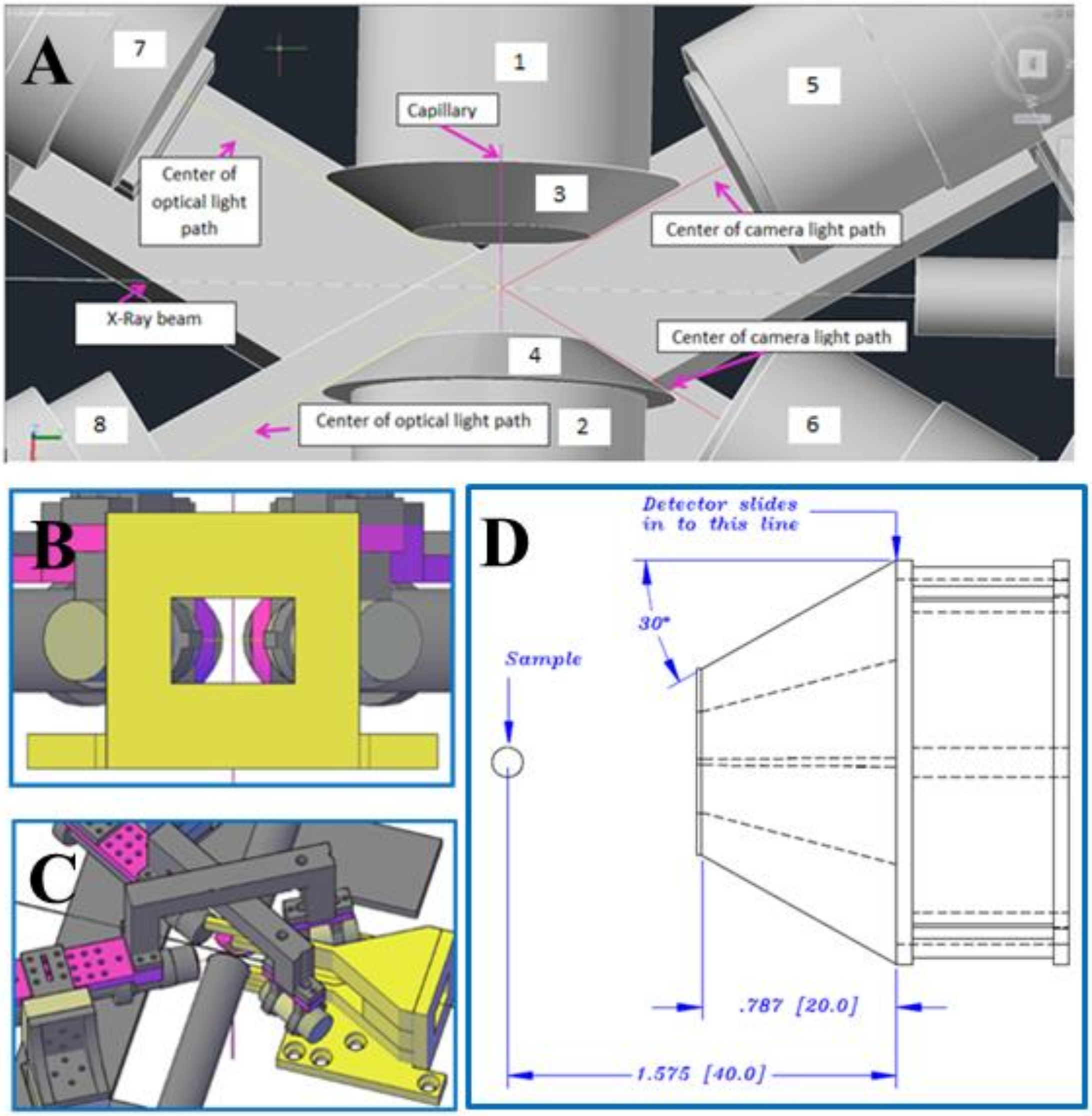

Figure IV.1 Instrument Schematics: (A) A close up of the center of the new instrument visualized in AutoCAD viewed from below. 1 & 2 are the detectors. 3 & 4 are Mo collimators attached at the end of each detector to restrict the amount of scattered photons that hit the detector element. 5 & 6 are either 5x or 10x Mitutoyo long working distance objectives. 7 & 8 are the focusing mounts for the fiber optic light guides that provide the bright field imagery of the microscopes. (B) A view of the capillary from downstream of the beam. The capillary is between the detectors and surrounded by the microscopes. (C) An eagle eye view of the instrument with the newly designed sample holder in place and He sheath attached. The Kapton® screen of the He sheath has been removed from the drawing for visual purposes. (D) A compact, 3D-printed point-focus spatial filter designed for use with the 4-element silicon-drift Vortex detector, similar in function to earlier prototypes as shown here. It was developed, in collaboration with Michael Pape of ANL/XSD.

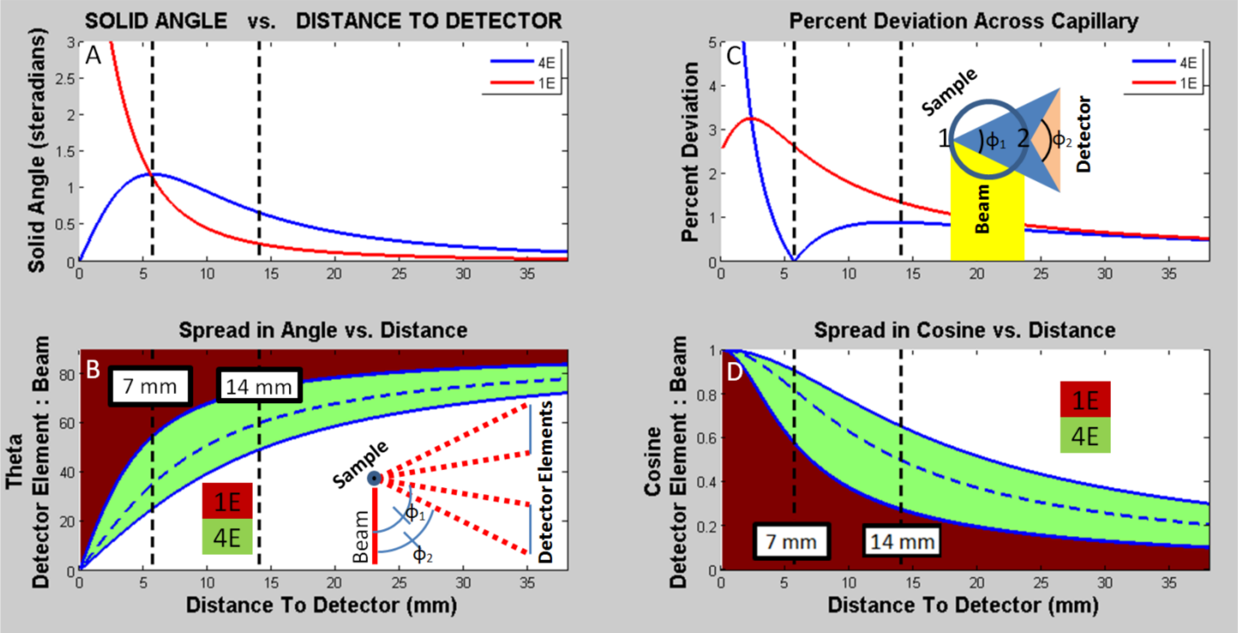

Figure IV.2 Scattering Considerations Pertaining to the Sample to Detector Center-to-Center Distance: (A) The solid angle of the detector as a function of the center-to-center distance between the capillary and the detector. (B) The spread in the solid angle between the beam and fluorescence from the capillary detected by the far edges of each detector element (φ_2 to φ_1). (C) The total percent change in solid angle between points 1 and 2 based on the representative angles φ_1 to φ_2. (D) The spread in the cosine of angles from B since Compton scatter is a function of cosine.

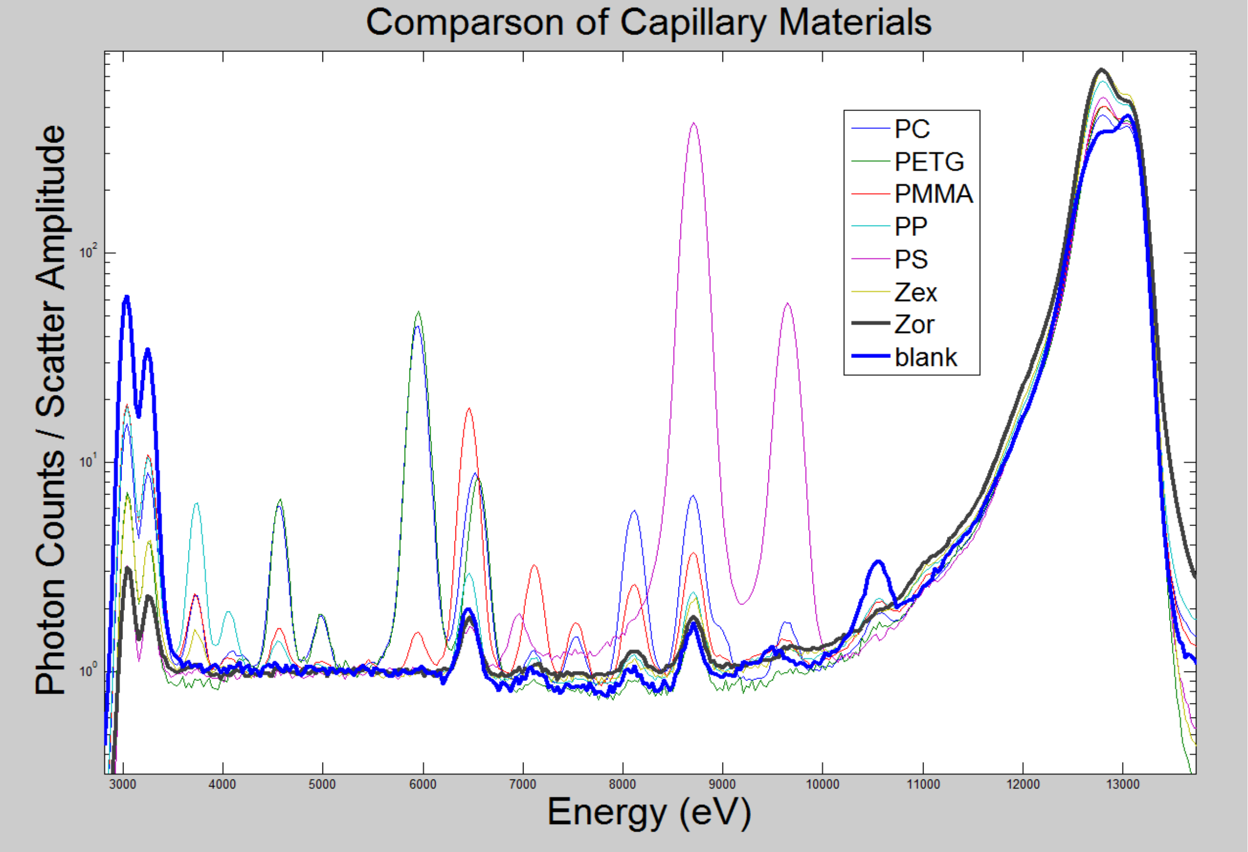

Figure IV.3 XRF Spectra of Capillary Materials: An overlay of the XRF spectra, obtained for the different capillary materials, normalized to their associated baseline height between ~5200 eV and ~5500 eV. Legend definitions: PC – Polycabonate; PETG - Polyethylene Terephtalate Glycol-modified; PMMA – Polymethylmethacrylate; PP – Polypropylene; PS – Polystyrene; Zex – Zeonex; Znr – Zeonor;

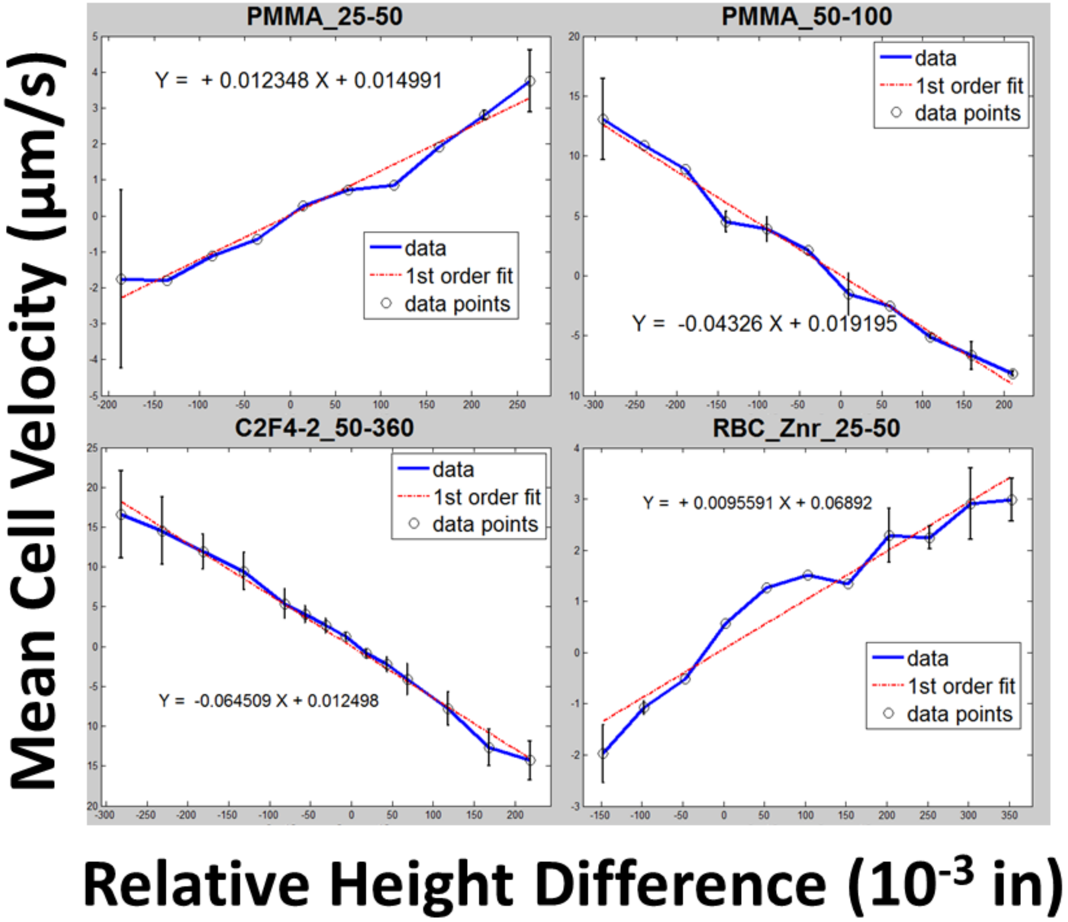

Figure IV.4 Syphon Pump Tests: The plots of cellular velocities of two hydrophilic capillaries and two hydrophobic capillaries as a function of the relative heights of the two sample holders of the syphon pump. PMMA, polymethylmethacrylate; C2F2, Teflon; Znr, Zeonor®; the trailing numbers refer to the inner and outer diameters of the capillary, respectively.

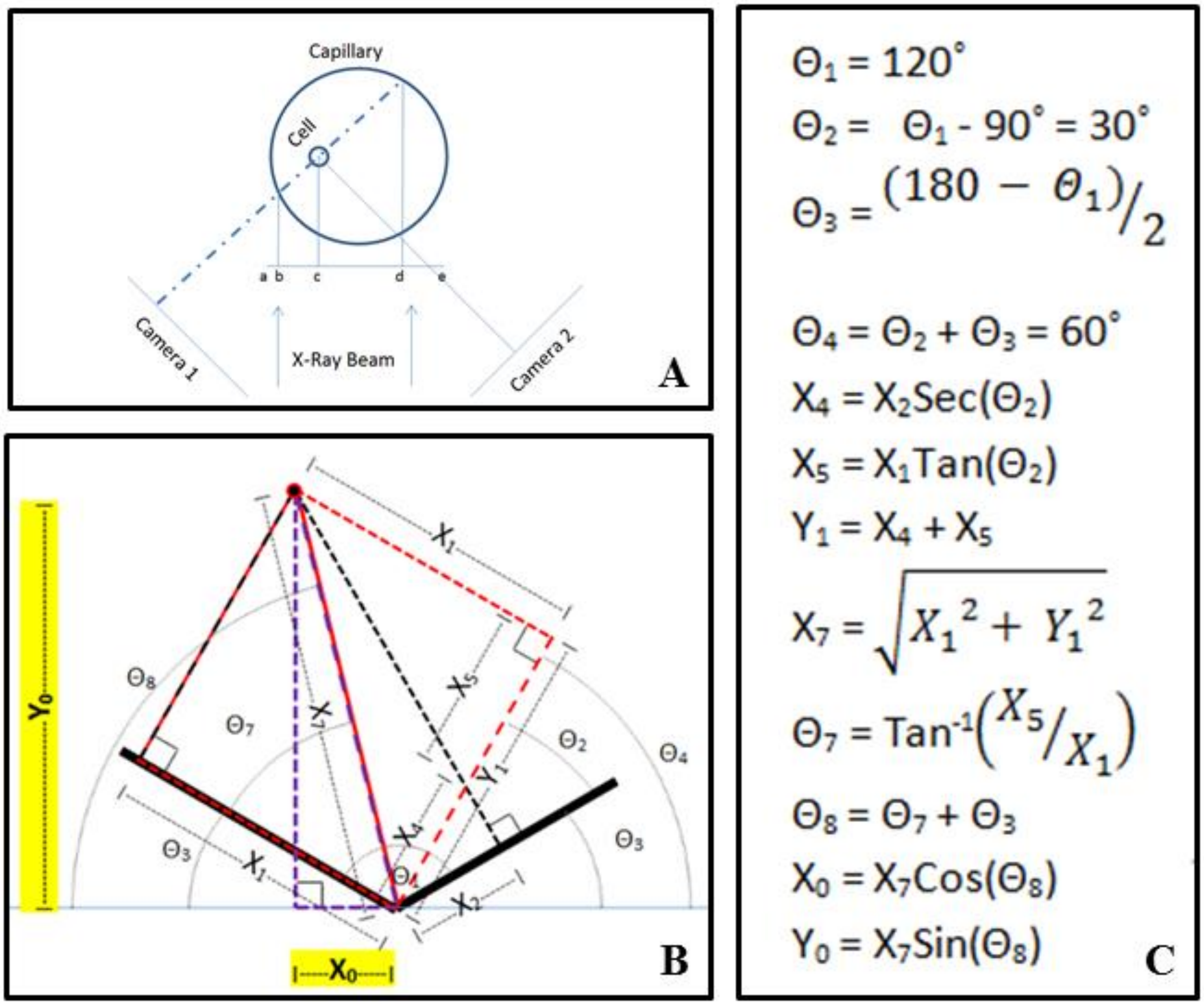

Figure IV.5 Combining Camera Images and Positioning Cells along the Horizontal Profile of the Beam: (A) The schematic illustration of the alignment of the two cameras. Without two separate viewing angles, it is impossible to determine the position of the cell along the horizontal profile of the beam. (B) The geometry for converting the recorded cell positions from the cameras into the cell position in the capillary. (C) The corresponding trigonometry for part B.

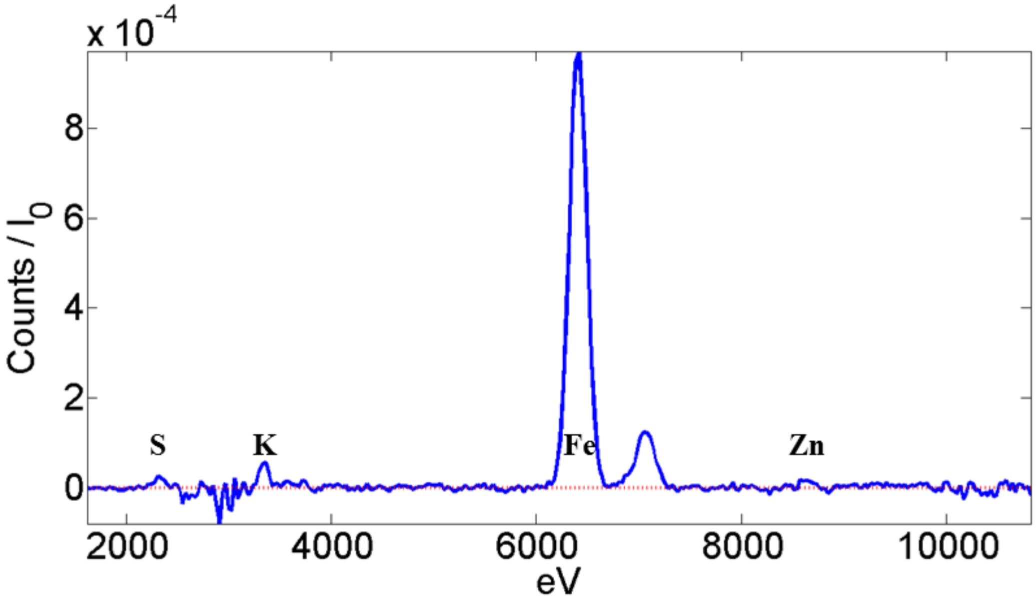

Figure IV.6 Mean bRBC XRF Spectrum: The blank corrected mean XRF spectrum from all the cell time points for the scan discussed in Figure IV.**7**. The associated signal-to-noise ratio for S, K, Fe, and Zn was 3, 6.5, 119, and 2.

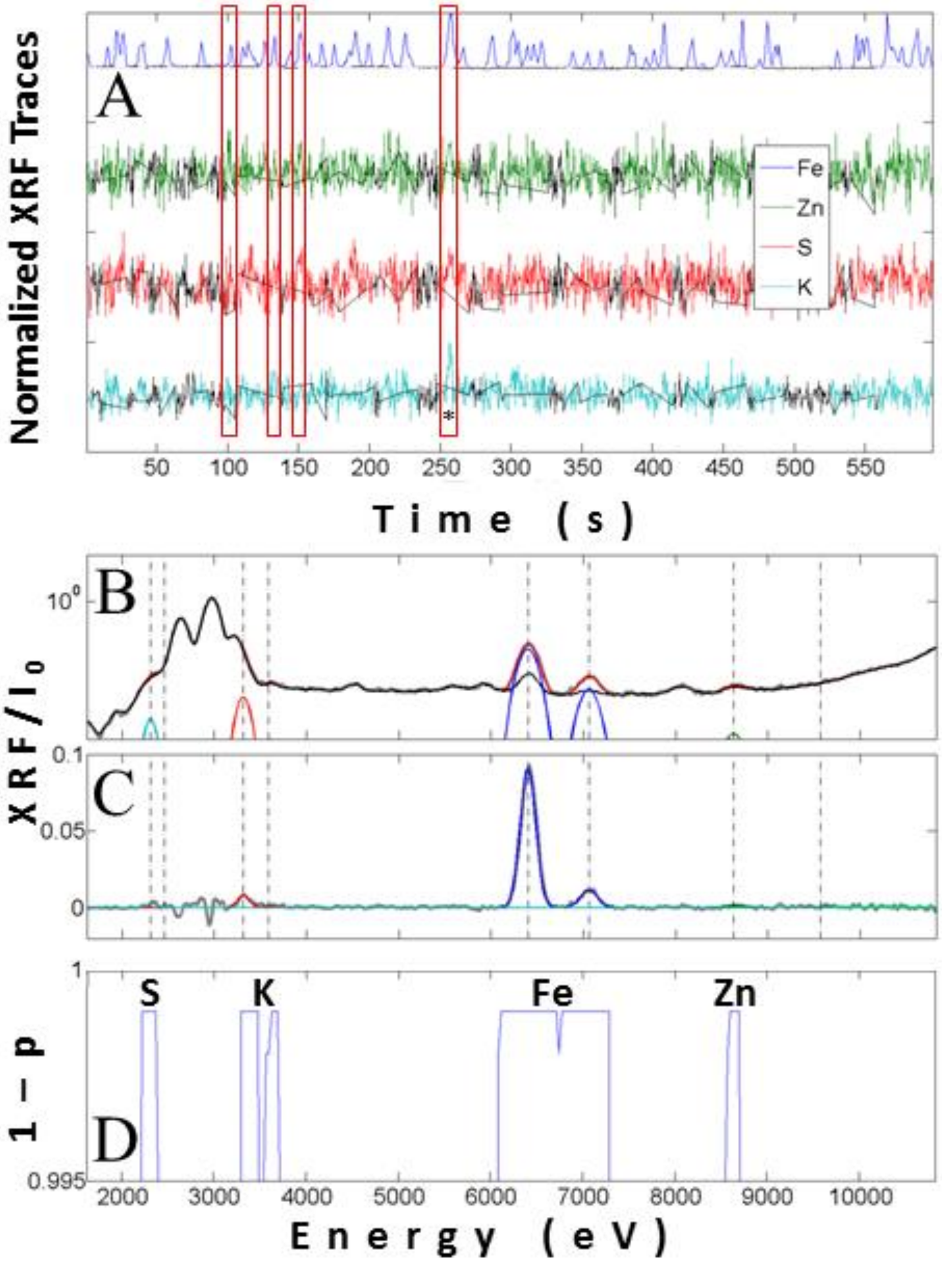

Figure IV.7 bRBC Analysis: Red blood cell data obtained from a ten minute scan using the flow cytometer. (A) The normalized signals from the Fe, Zn, S, and K channels of the scan. (B) The fitted XRF spectrum sum of the red boxed peak with the asterisk from A. (C) The blank corrected signal from the fitted XRF (B) for a single bRBC peak. (D) A statistical t-test across every channel comparing the means of the cell pixels with the mean of the background pixels using a significance cut-off of 0.001.

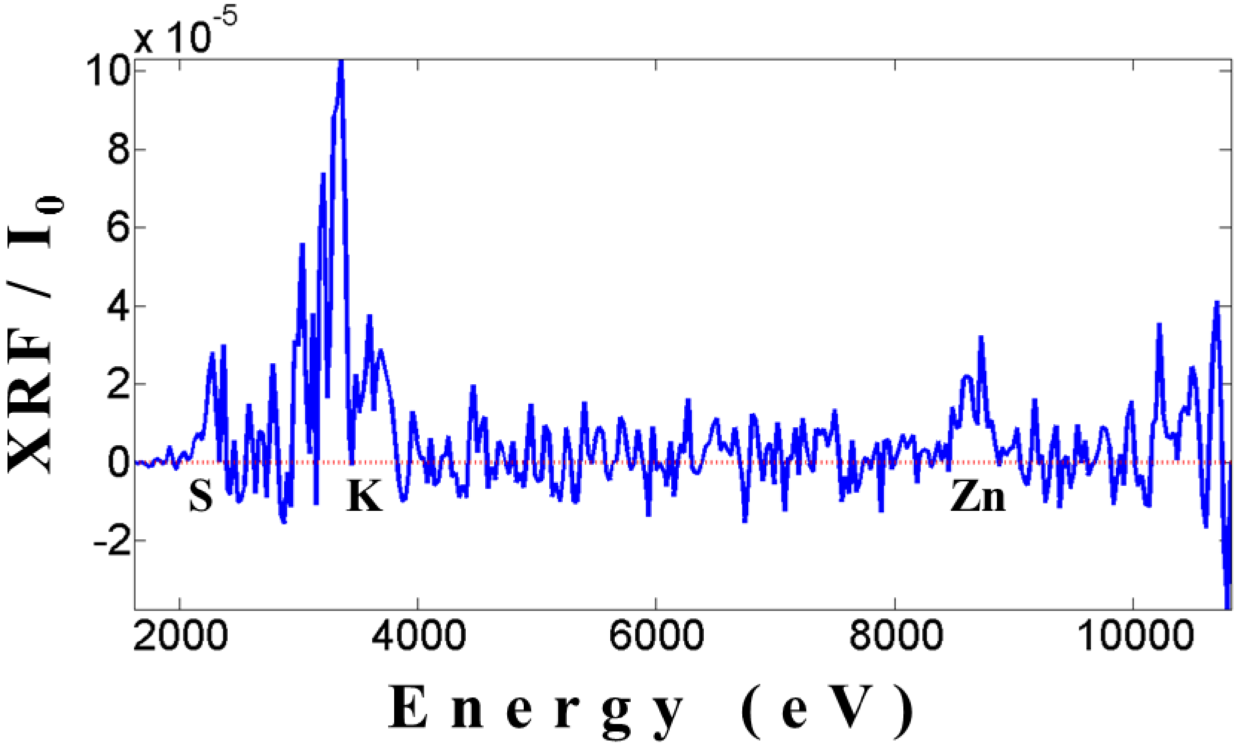

Figure IV.8 Mean Yeast XRF Spectrum: The mean blank subtracted cell spectrum from a scan of yeast taken using 25 µm i.d., 50 µm o.d. Zeonor® capillary. S, K, and Zn are clearly visible with a signal-to-noise ratio of ~2, ~10, and ~3, respectively.

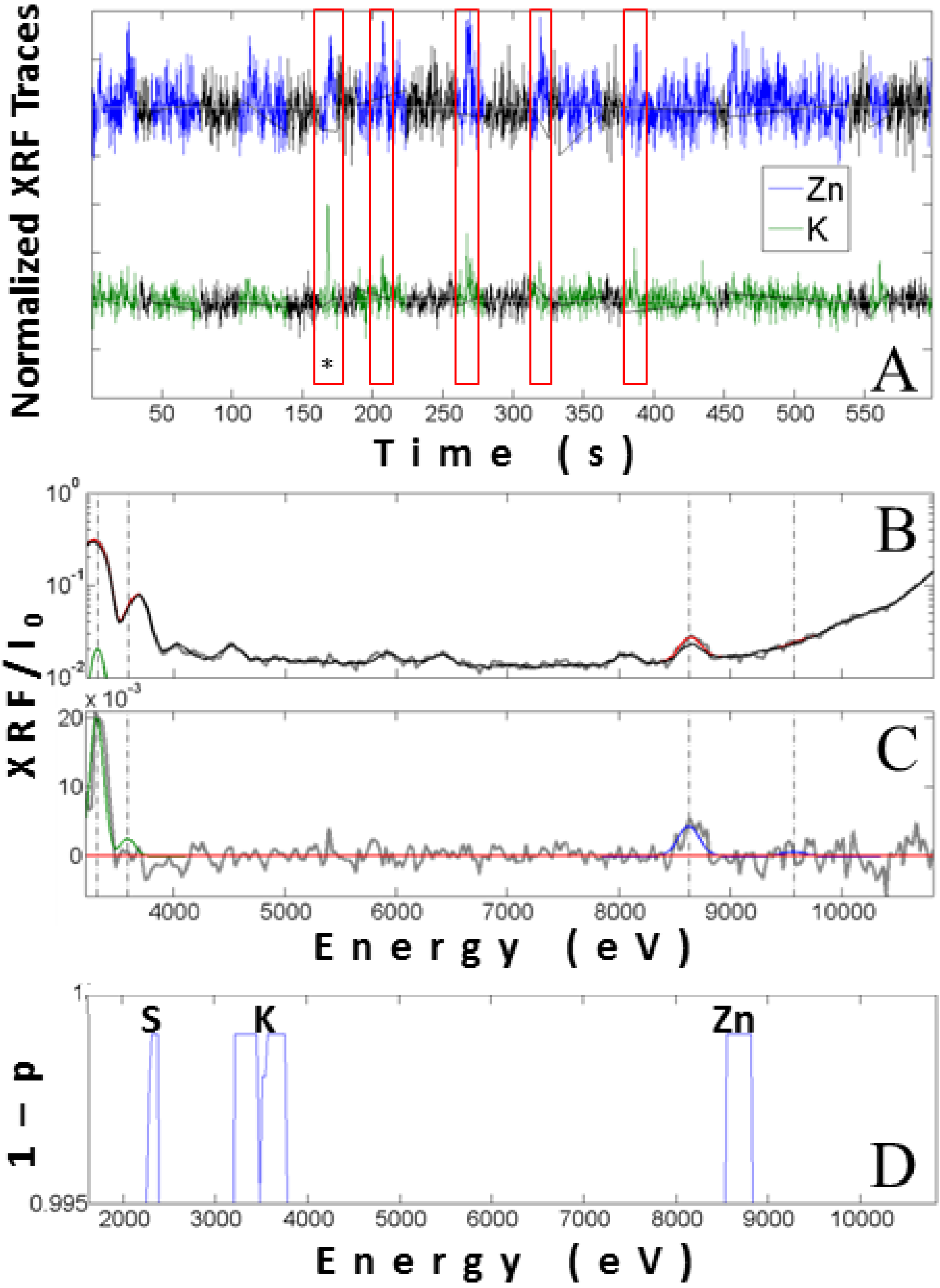

Figure IV.9 Yeast Analysis: (A) the normalized signals from the Zn and K channels of the scan. (B) The fitted XRF spectrum sum of the red boxed peak with the asterisk from A. (C) The blank corrected signal from the fitted XRF (B) for a single yeast peak. (D) A statistical t-test across every channel comparing the means of the cell pixels with the mean of the background pixels using a significance cut-off of 0.001.

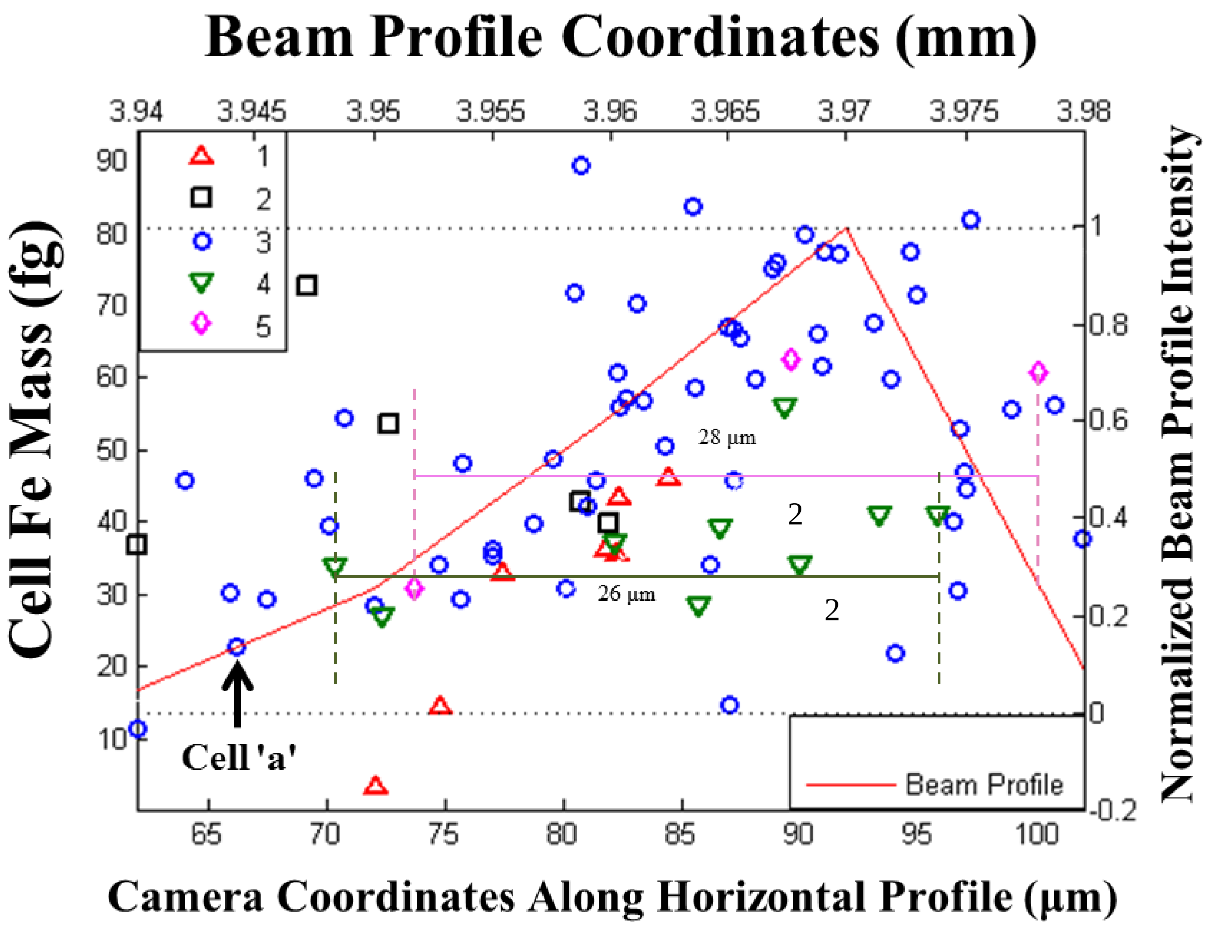

Figure IV.10 Inspection of the Horizontal Beam Profile: The Fe masses from 5 bRBC scans plotted as a function of their coaxial distribution with respect to the horizontal beam profile. The x axes on the bottom and top are the coordinates assigned by the camera (units of and the beam profile, respectively. Mass is in fg.

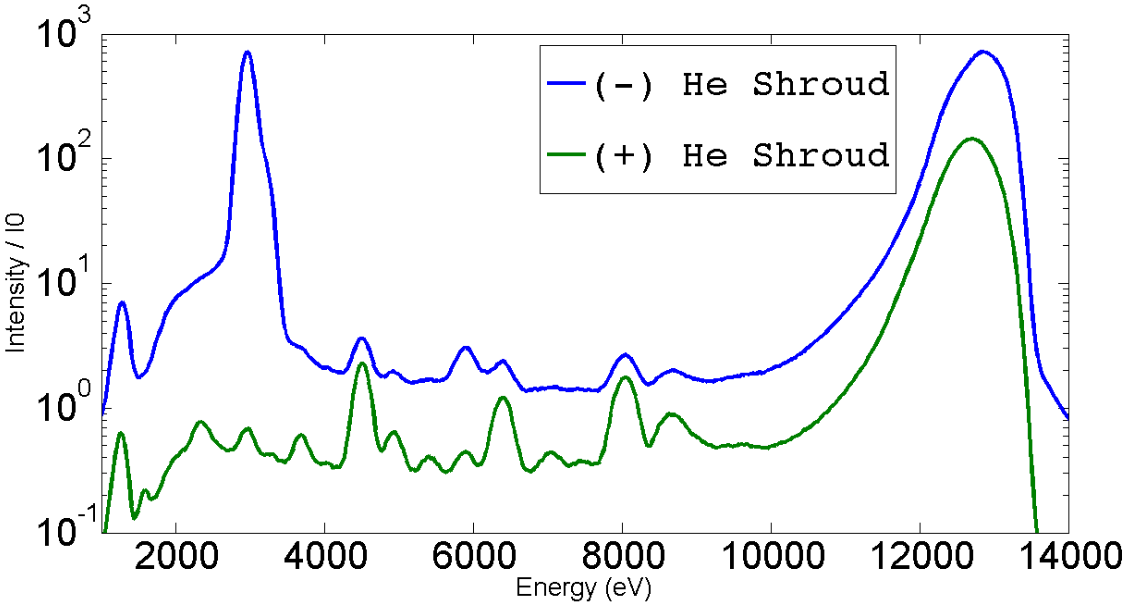

Figure IV.11 The Helium Shroud: Demonstration of the decrease in scatter and secondary Ar fluorescence whn using a He shroud. The two spectra are the mean spectra obtained from empty 15.5 id 31 od Zeonor ® capillaries, normalized to the upstream beam intensity as measured by an N_2 filled ion chamber.

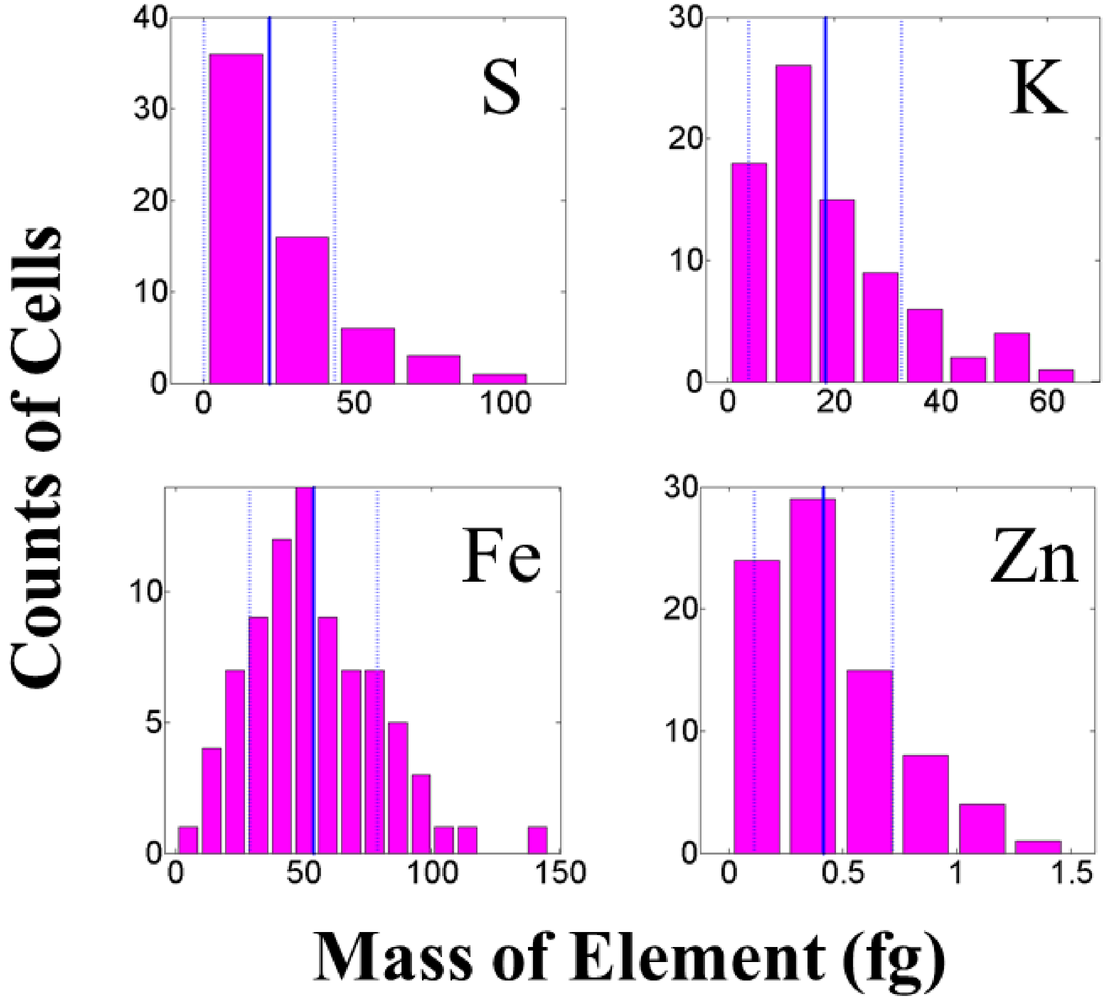

Figure IV.12 Distributions: Cell-mass histograms for bovine RBCs of S, K, Fe, and Zn, moving right then down, respectively. The histogram for S was taken from the sub-population and contains a smaller n.

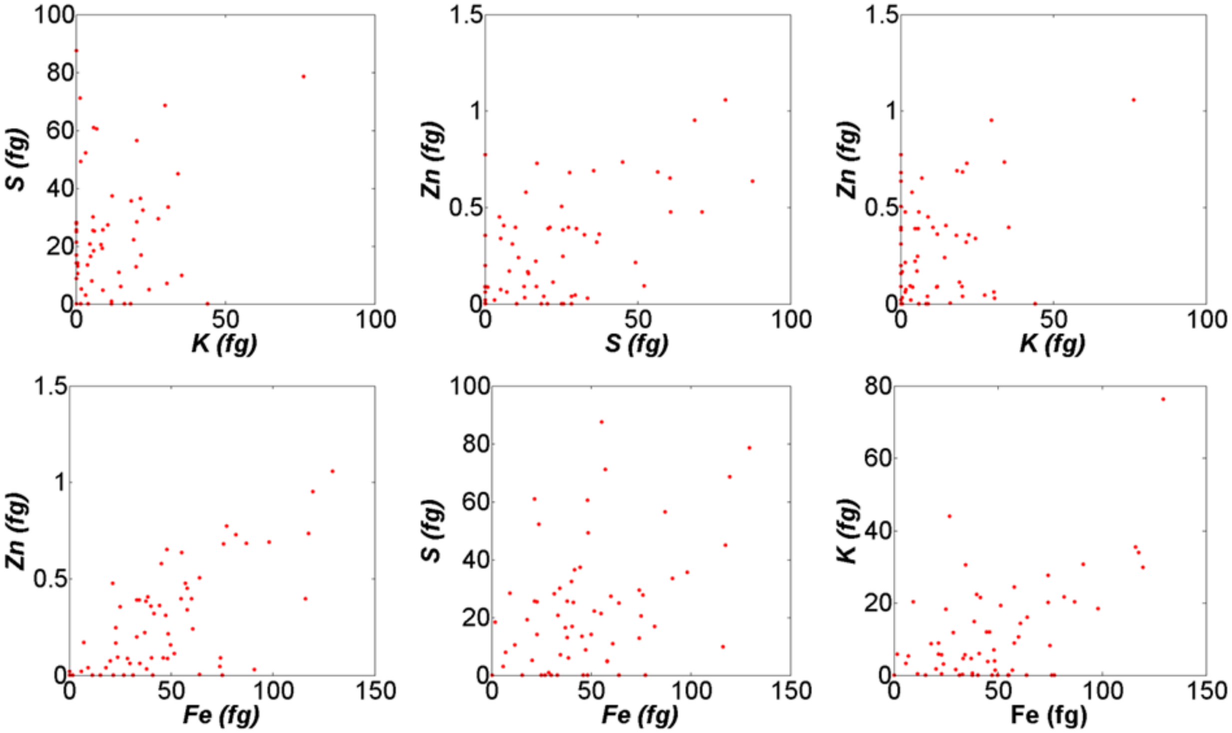

Mean Absolute Uncertainty (fg): K - 1.0 S - 3.3 Zn - 0.038 Fe - 0.86

Figure IV.13 Correlations: Cell-mass correlation plots for bovine RBCs for the various combinations of S, K, Fe, and Zn.

	Helium Shroud (CPS/I0)		
	Without	With	Change
Element	*(a)*	*(b)*	*[b-a]/a*
Ar	1.9E+01	1.2E-02	-100%
Si	3.7E-02	5.2E-04	-99%
K	2.3E-01	4.1E-03	-98%
Cl	4.3E-01	7.9E-03	-98%
P	1.5E-01	5.3E-03	-96%
S	2.4E-01	1.4E-02	-94%
Mn	5.9E-02	4.0E-03	-93%
Cr	5.5E-03	3.0E-03	-44%
Ni	1.0E-03	6.2E-04	-38%
Ca	1.1E-02	9.5E-03	-10%
Ti	5.6E-02	6.1E-02	8%
Zn	1.8E-02	1.9E-02	10%
Fe	2.9E-02	3.3E-02	11%
Cu	5.1E-02	5.7E-02	13%
Total	2.0E+01	2.3E-01	-99%

Table IV.1 Effect of the Shroud: Baseline correction and subsequent quantification of the various elements.

CHAPTER V: M-BLANK

V.1 INTRODUCTION

V.1.1 THE PROBLEM

During the initial stages of developing the flow cytometer, it became apparent that the available tools were inadequate at addressing the fundamental requirements for processing and analyzing the raw data. The tools developed to address that deficit have a much broader application than just the flow cytometer. This chapter delves more deeply into the mechanics of data fitting. The tools developed to address the issues associated with the cytometer data are shown to be useful, not just for the flow cytometer but also for imaging data. This corrects a flaw in XRF imaging analysis that may have important implications for elemental quantitation in cells.

It is important to first understand the problem that is being "solved" when one is fitting XRF data. With XRF, the mass of a particular element, e.g., Fe, K, Zn, is not measured; rather, what is measured is an energy spectrum. From the energy spectrum the area under the peaks that correspond to the various elements are "fit" using calibrated equations. From these "fit" areas, the mass of each element is then calculated using a sensitivity calibration curve obtained from the fitting of standards. The problem is that the area for each element also comes with a background that must be removed.

V.1.2 XRF CONTINUUM AND BACKGROUND ESTIMATION

The two main contributors to the backgroun in x-ray fluorescence are the coherent and incoherent scattering of the incident beam by the sample and the signals from the sample. Furthermore, there is the possibility of escape peaks, pileup and summation peaks, K-LL Auger transitions, and incomplete charge collection in the detector caused by regions of low electric field or a dead layer in the detector all contribute to apparent intensities at lower energy being higher than expected [1]. Finally, the spectrum may be contaminated with emission lines arising from non-sample - e.g. hutch fluorescence excited by the scattered X-Ray beam [2-4]. Even if there were no background, XRF data cannot be quantified by simply summing a region of interest (ROI) [5-8]. Even the best energy dispersive detectors have finite resolution causing some emission lines, such as Cu Kβ and Zn Kα, to overlap [9, 10].

Since scattering from the sample substrate is a majore contributor to the background, it is difficult to measure a blank. Once the sample and sample holder are removed from the beam, the apparent background changes. Many methods have been developed to deal with the issue of XRF background estimation in the absence of a blank [11-20]; all of these calculate a baseline (*i.e.*, a smooth line that is intended to mimic the background) rather than a blank (*i.e.*, an experimentally measured background).

In both cases, blank and baseline, the goal is to model all fluorescence that arises from "non-sample" so that it can be removed leaving only the sample's fluorescence. A baseline, in principle, should follow smoothly along the spectra connecting the two sides of the base of each spectral peak. The most common approach to determining the baseline utilizes what is called a snipping function [1]. A snipping function compares each channel *n*, of a spectrum, to its two neighbouring channels, *n* ± 1; if the intensity at channel *n* is greater than the mean intensity of channels *n* ± 1 then the output intensity at channel *n* is set to the mean intensity value of its two neighbours. If performed iteratively this process creates a baseline that passes through local minima, and thus has the effect of peak-stripping as graphically represented in Figure V**.1**.

An illustration of both a blank and a baseline applied to the spectrum sum of an entire image is presented in **Figure V.2**; visually, it can be seen that a blank includes many features that are not included in the baseline estimate of the background. This problem is even more critical for single pixel analyses due to the low count rate. **Figure V.3** shows the XRF spectrum and the blank for a cell. The black line is the mean of all the non-sample pixels and is identical to the blank that is calculated by M-BLANK. The pink line is the mean spectrum calculated from all the cell pixels. Each of these represents the average of hundreds of pixels. The red dashed line across the image indicates the signal that would seen if there was an average of one count pixel^{-1} at every energy channel. The yellow highlighted portions indicate spectral regions where both the mean background and mean signal are below the red dashed line. For these energies, it is impossible to calculate a baseline, since for most pixels there are no counts. In contrast, the blank can account for the background across the entire spectrum. The affected region where most of the biologically relevant transition metals fluoresce [21].

Although the baseline is a very poor model of the background in this region, it is at least uniform. In contrast, due to the per-pixel noise the lowerenergy baseline calculated on a per pixel basis is not uniform. This is graphically depicted in **Figure V.4**. Panels A and B show the baseline calculated using 500 iterations of a snipping function at each of ~1000 pixels. The calculated baselines for background pixels span two orders of magnitude, while the calculated baselines for cell pixels span another three orders of magnitude. Panel C demonstrates the consequences of the variability in A and B by overlaying the signal and the calculated baseline for one "cell" pixel and one "background" pixel.

Panel D is the image of the baseline amplitudes for the Si region and E the image of the background amplitudes obtained for the Cr region. If the baseline error were uniformly distributed across the associated background/cell pixels it might be possible to correct for this error; however, D demonstrates that uniformity is not the case and the error introduced by per pixel baselines is systematic. This agrees with the apparent cell image from the Si baseline amplitudes. Expectedly, for ~4,000 eV – 8,500 eV, there is no non-zero baseline and therefore a uniform treatment of the associated energy bins by a baseline across all pixels. This baseline amplitude image for the Cr region (E) supports this as it shows a "zero" imaging of the cell by the baseline amplitudes.

Because of this sensitivity to noise a blank is a far better approach than a baseline for calculating the background. If a blank is not possible, then a baseline should be calculated from the mean of all the pixels. Most importantly, a baseline should never be calculated on a per pixel basis. Unfortunately, a per pixel baseline is the dominant approach currently adopted by the field (e.g., MAPS [22], PyMca [18], AXIL [13]).

The attraction of per-pixel baseline fitting can be understood from the nature of many XRF samples. If the sample is a one-of-a-kind mineral, there may not be a viable "blank". In this case, a baseline may be the only practical way to estimate the concentration of element. However, for biological specimens deposited on Si_3N_4 wafers, there is always a region of Si_3N_4 that is sample free and can be used to calculate a blank.

To determine the practical differences between a blank and a baseline, this chapter compares two programs used for the fitting of XRF data sets: M-BLANK (the program used for fitting of the XRF data in this thesis) – which uses a blank when possible but also has a modified snipping functionality (Figure V.**1**B) - and MAPS [22] (a widely used program created in 2003) - that calculates a per pixel baseline. MAPS was chosen simply based on convenience of access and we expect the results from this comparison to be very similar to one between M-BLANK and other programs that implement per-pixel baselines (e.g., PyMca [18], AXIL [23]). Both MAPS and M-BLANK produce maps (or images) of the various elemental contents of cells. However, the main difference between M-BLANK and MAPS is how each program accounts for the background contribution of fluorescence.

M-BLANK's methodology of accounting for the blank should remove the need for a baseline, since in principle the blank should remove everything except the fluorescence contribution of the cells. To test this hypothesis, we fit data obtained from sector 2-ID of the Advanced Photon Source, ANL and then compared our fits directly to those obtained from MAPS.

V.2 EXPERIMENTAL

V.2.1 FITTING AND PROCESING WITH M-BLANK

Prior to fitting, each image that contained multiple cells was digitally separated into separate images so that each data set consisted of one image per cell. This allowed for each cell to have its own unique background.

Blanks were calculated from the background pixels of each image in an iterative process that began by using the potassium Kα emission line to generate a raw image of the cell. Since this was done prior to fitting, a region of interest (ROI) for the potassium Kα emission was defined as the channel of its centroid ± the FWHM of that emission. The summation of this ROI was taken for each pixel. Then all pixels w/ intensity greater than 50% the maximum potassium

Kα were defined as "cell" pixels. All non-"cell" pixels were considered background. These two groups, "cell" and everything else form the initial seed for the iterative process. Then, each round of iteration begins by calculating the mean, $\bar{x}$, and standard deviation, σ, of the non-"cell" pixels. A threshold, T, is calculated by adding 3σ to the mean, $T = \bar{x} + 3\sigma$. Background pixels with a potassium Kα emission intensity greater than T are redefined as "cell" pixels, and this process continues until no new pixels are redefined.

After the identification of "cell", the blank was subtracted from each pixel and each pixel was fit using linear least squares. Following fitting, each cell image was visually inspected to verify an appropriate cell ROI (region of interest) had been generated. Since the data contained images with budding yeast cells, there were instances where a bud had such low concentration of K that the bud did not register as cell. In situations such as these, the ROI was manually modified to include the bud (Figure V.**5** is a prototypical example) and the data was once again fitted. Of 228 cells, only one needed correcting.

V.2.2 PROCCESSING OF THE MAPS FITTED DATA

MAPS fits every single pixel with no *a priori* knowledge of whether a pixel is background or cell. To account for a blank, the mean value of all the fitted background pixels for each element was subtracted from each pixel of that elements image. The cell and background pixels for MAPS were defined to be the pixels used with M-BLANK.

V.2.3 FITTING OF CALIBRATION STANDARDS

The standards were processed using a modified snipping function (Figure V.**1**B) that acts on the mean spectrum of the standard. The function is identical to the snipping function in **Figure V.2**A except that prior to processing, all channels with zero counts are excluded. After processing, the values for the excluded channels are interpolated from the resulting peak-stripped baseline, giving the mean baseline spectrum as its final output. By performing the snipping function only on the nonzero channels we avoid a baseline of zero in any region that has a low count rate (e.g., from ~4000 eV to ~8500 eV). This modified snipping function is compared with the regular snipping function in **Figure V.2**.

Because we fit the samples with an extracted blank but fit the standards using a modified snipping function, it is possible, in principle, that the latter could cause a difference between MAPS and M-BLANK in calibration. The difference between correcting with a blank vs. correcting with a baseline is graphically depicted in **Figure V.6**; 'a' measures the height difference between the blank and the signal and 'b' measures the difference between the baseline and the signal. If $b - a \ll b$, then the difference in quantitation can be neglected. Since the signal from the standard was 7 orders of magnitude larger than that from the samples, the background makes a negligible contribution to the standards, and $a \approx b$.

V.3 RESULTS

V.3.1 BASELINE CORRECTION (MAPS) VS. BLANK CORRECTION (M-BLANK)

Use of a baseline instead of a blank can significantly affect data for the samples. At low energies (<4000 eV) the baseline is non-zero. As expected, at intermediate energy (4000 eV - 8500 eV) the baseline is effectively zero due to the very low counts. Finally, at higher energies the baseline is dominated by scatter. This can be seen in the MAPS fitted output in Figure V**.7**. For comparison, **Figure V.8** is the same data fitted using M-BLANK.

Referring back to Figure V**.7**, the drop off of the baseline at ~4000 eV causes incorrect quantitation of Ca and will almost definitely lead to an overestimation of its concentration as both the Kα and Kβ peak will be overestimated in order to correct for the underestimated baseline, and thus minimize the total residual.

One unexpected consequence of using a baseline is that the calibrated peak widths are wrong. The peaks in region 1 are too wide and short and the peaks in regions 2 and 3 are too tall and too narrow. This can be readily seen by comparing the peak shapes of K and Cu with their respective raw fluorescence. Essentially, overcompensation of the peaks FWHM in region 1 results in the under compensation of the FWHM in regions 2 and 3. The equation that MAPS uses to fit its FWHM is the same one used by M-BLANK: $FWHM = S_0 + S_1\sqrt{E}$.

Due to the baseline error, MAPS overestimate FWHM at low energy, which makes S_1 too small. A direct comparison of these two parameters shows this to be the case. For MAPS, S_0 and S_1 were 131 and 0.019, respectively. For M-BLANK they were 71.3 and 0.124, respectively. The apparent increase in FWHM at low energy results from an apparent broadening of the peaks in order to compensate for an underestimate of the baseline XRF continuum.

V.3.2 COMPARISON OF RESIDUALS: BASELINE CORRECTION (M-BLANK) VS BLANK CORRECTION (M-BLANK)

To see if we could explain the observed difference in FWHM as a consequence of the calculated baseline (the blank being referred to as a 'baseline' here), we compared the fitted data from M-BLANK using its snipping function to estimate the background with the fitted data from M-BLANK using the blank. As an important note, the baseline corrected fits produced by M-BLANK for this comparison (and only for this comparison) did not exclude channels with zero counts during baseline estimation. This was done to make this comparison more representative to one with MAPS. Figure V.**9** shows the results obtained from that comparison. The results of that comparison are different from those observed in MAPS. For the fitted baseline corrected data relative to the fitted blank corrected data, we see an increased residual at the centroids for the lower energies (e.g., Al) paired with decreased residuals immediately on either side of the centroid. This pattern corresponds to what one would expect to see if a peak is artificially lifted up to compensate for fluorescence on either side of the peak due to a negligent accounting of the background fluorescence.

V.3.3 COMPARING QUANTITATION BETWEEN BOTH METHODS

The normalized quantified masses determined by both programs are compared in **Figure V.10**. For each element, the masses were normalized between negative one and one using the range spanned by output values from both programs and dividing each value by the maximum absolute value from that set. **Figure V.10** shows an expansion of these data with the mean M-BLANK fitted values plotted to the x-axis and MAPS' to the y-axis. The bold black line shows the expected 1:1 correlation. Although the data fall on a straight line, the slope varies with atomic number. There is a general systematic over-estimation by MAPS, relative to M-BLANK, at low energy and a systematic under-estimation at energies above ~Fe (6.4 keV).

V.3.4 COMPARING BACKGROUND DISTRIBUTION WIDTHS

To compare the relative precisions of the two programs, the histograms for each element's background pixels were fitted with Gaussian and normalized to a constant area. These are shown in **Figure V.11**. This shows that in addition to differences in quantitation, there are also differences in precision. For all elements less than ~4,000 eV, the MAPS precision is much worse than the M-BLANK precision while at higher energy the MAPS precision is slightly better.

Since these are background pixels, this speaks to the harmful nature of using the snip width. This behaviour is consistent with what we would expect based on **Figure V.4** A and B;

variability in the line shape of the snipping baseline causes a significant variation in the apparent peak area.

To further investigate the relative associated precisions, in **Figure V.12**A the fitted standard deviations from MAPS were divided by those from M-BLANK. The ratios of the fitted Gaussians standard deviations for cell pixels are also included. This shows that the lack of precision displayed for background pixels is also present for the cell pixels and that the contribution of the baseline is once again not negligible. The noise that arises from the baseline in sample pixels will broaden population distributions and may blur images.

V.3.5 PER-PIXEL CORRELATIONS FOR ARGON AND SILICON

Looking at **Figure V.12** B and C, an interesting observation was made when comparing the mean cellular values for Ar and Si. M-BLANK gave positive values whereas MAPS yielded negative values. Therefore, even though these elements usually are not biologically interesting (apart from aquatic protists for Si, [24]), for the comparison of these two programs, both Ar and Si were found to be diagnostically relevant.

V.3.5.1 COMPARISON OF FITTED BACKGROUND CORRECTED Ar MASSES

When looking at fitted Ar fluorescence, there are four things to consider. 1) Ar is present in the atmosphere at ~1% concentration; 2) there is no biologically relevant Ar signal 3) increased scattering of the x-ray beam will cause increased secondary excitation of Ar fluorescence; and 4) the amount of beam scatter is proportional to the amount of material in the beam. Taken together, this means that an increase in cellular content should cause a small increase in scatter and, in atmospheres that contain Ar, secondary excitation of Ar by that scatter should lead to a small increase in Ar fluorescence. The correlation plots for both cell and background pixels for Ar with elements below 4,000 eV are plotted in **Figure V.13**.

For the cell pixels, M-BLANK fitted data yield the expected positive correlation between Ar and the other elements for cell pixels. For the MAPS fitted data, all of these correlations are negative (except for with Si) and the Ar background corrected cellular masses collect at a corrected mass value equal to the negative mean of the fitted background mass for Ar.

V.3.5.2 COMPARISON OF FITTED BACKGROUND CORRECTED Si MASSES

Things to consider when looking at correlations with Si are that the sample is resting on a Si_4N_3 wafer and that there is no biologically relevant Si signal. Referring back to **Figure V.12**, note that similar to Ar, the mean of the fitted background corrected Si masses for cell pixels is also negative. In principle, it is possible that cell blocks the fluorescence of the Si causing a decrease in the detected Si fluorescence by the detector; however, this is ruled out by a small but detectable increase in Si fluorescence when comparing the peaks of the mean cellular and background XRF calculated from the raw data (see **Figure V.14**). Consistent with this M-BLANK fitted data shows a ~ 24X increase in Si fluorescence for cell pixels over background pixels. We attribute this to a slight increase in secondary Si excitation, arising either from scatter or, more likely, from K fluorescence.

In the same manner that was done with Ar, **Figure V.15** shows the plotted correlations of Si with the elements in the non-zero baseline region for both M-BLANK and MAPS. Just like Ar, the M-BLANK and MAPS fitted cell pixels yielded opposing results.

V.4 DISCUSSION

V.4.1 SLIGHT OVERESTIMATION TO UNDERESTIMATION OF THE ELEMENTS FROM 4,000 EV TO 8,500 EV

There is a transition from slight overestimation to slight underestimation of the elements in the region where the baseline falls to zero. There are two contributing factors to this, both of which are caused by the zero baseline. First, there will be over estimation of the peak amplitudes by the fitting program. Second, the scatter fall off (which is not accounted for) will cause the elements at higher energy to be underestimated in proportion to the amount of unaccounted for scatter in that region.

Since the fitted baseline has zero amplitude for this energy region (see **Figure V.7**), every time there is a random count due to instrumental noise, an emission line that overlaps with that count will register a nonzero fitted value for that pixel. This will have the effect of artificially augmenting the apparent intensity of that element. This will impact both cell and non-cell pixels.

V.4.2 NON-UNIFORM QUANTITATION AND LACK OF PRECISION

There is non-uniform quantitation in the region where the snipping function is able to provide a non-zero baseline. **Figure V.4** explains the increased distribution widths and lack of precision for MAPS relative to M-BLANK. Importantly, **Figure V.12** shows the presence of a exponential trend of increasing precision from low energy to high energy on the part of MAPS relative to M-BLANK. The fluctuating non-zero baseline at energies below 4,000 eV is almost certainly a big contributory factor to the increased noise. Additionally, the increased lack of precision at lower energy may be caused by the cumulative raising of the baseline (and with it, an increased distribution of noise around any answer) which occurs due to incomplete charge collection of the detector [1].

V.4.3 BASELINE ELEVATION IS PROPORTIONAL TO AMOUNT OF CELLULAR MATERIAL IN THE BEAM.

The trend from the correlations between MAPS and M-BLANK of over-estimation to under-estimation from low energy to high energy isn't perfect. Si, Cl, Ca, and Ar do not obey this trend. In order of increasing atomic number (neglecting Ar), the elements should be S, Cl, K, Ca; however, what we see is S, Ca, K, Cl. Though the trend itself could be explained by a calibration error, the switching of Ca and Cl cannot. **Figure V.17** combines the relevant observations from Figures 0, 0, and 1 to explain these deviations; it also explains the decreased quantitation for Zn (from MAPS relative to M-BLANK). Figures 0C and 0C explain the inverse relationships (negative slopes) apparent for Ar and Si, respectively.

The inverse relationships between the two programs for the fits of Ar and Si masses for cellular regions (seen in **Figure V.10**), from MAPS fitted data, is a result of an elevated baseline in those regions for cell pixels relative to background pixels. This can be seen by looking at Figures 0C and 0C, respectively. What these show is a non-negligible increase in the elevation of the baseline for cell pixels relative to background pixels. This was demonstrated by **Figure V.4** A and B. This means that in addition to the considerably large amount of noise added by the fluctuations inherent in a per-pixel baseline, there is an increase in the baseline for cell pixels relative to background pixels which leads to decreased quantitation. More importantly, this error is systematically linked to the amount of cellular content in the beam. The impact of the baseline on Si is also supported by its positive correlation with Ar. Although unrelated here, this impact of the elevated baseline due to increased stuff in the beam may have very important implications on other work where the impact of the Si peak is extremely important [25].

The deviations of Cl and the decreased quantitation of Zn (by MAPS relative to M-BLANK) can also be explained by the elevated baseline. **Figure V.17**A shows an elevated cellular baseline for Cl. he large K peak for cell pixels causes the snipping function to give a larger baseline in the cl region of cell pixels than in the Cl region of non-cell pixelsFrom the mean cellular and background raw fluorescence in **Figure V.17**C, (and remembering that the red line is the cut-off for a single count being detected by the detector) it can be seen that there is a potential non-zero baseline for cell pixels where there most likely won't be one for background pixels. The increased quantitation of Ca is rooted differently. The Kβ peak for Ca is at 4013 eV; this is in the region where the baseline falls to zero. **Figure V.17**B shows that because of this, the Kβ peak of Ca is possibly elevated to compensate for the missed fluorescence by the baseline. Note the baseline falls off right at the Kβ peak and that there is a significant gap between the raw fluorescence line (white) and the line of total fit (red). For comparison, the Ca Kβ peak has been noted in the fit to the same in M-BLANK (see **Figure V.18**).

V.4.4 INCORRECT TAIL FUNCTION ASSIGNMENT

The increased baseline for cell pixels explains the presence of negative values for Ar; however, by itself it does not explain why so many values for fitted Ar fluorescence following ROI processing and post fitting blank correction are collected at – 2.7 cts/I0 (the negative of the background mean). This means that those (those that are -2.7) values prior to the post processing blank correction performed by MAPS were set at a value of 0 cts/I0.

The apparent decrease in Ar fluorescence below that value for cells indicates that its fluorescence is being accounted for elsewhere. For example, it's possible that MAPS may be over-accounting for the tailing end (lower energy side) of K with its applied tail function. This can best be seen in Figure **V.7** by looking at the expanded portion of the image of the MAPS fitted spectrum. The tail function appears to be overcompensating for the tail of K causing the total fit to the data to be elevated above raw fluorescence. This would result in a depression of Ar fluorescence to compensate for the over-accounting of the K tail. This would happen most when there is an intense K peak such as when there is a cell in the beam. When that happens, the fitted Ar fluorescence would be depressed. Since the tail functions are linked by a quadratic polynomial, this suggests that the tail function used by MAPS to accommodate for tailing at the lower energy end of other peaks may be incorrect as well.

If the fitted Ar fluorescence is decreased in cellular regions, we would expect to see a lot of values at or close to zero. For the background corrected fluorescence of MAPS, the lower limit is the negative mean of the element's background pixels. For Ar, that value is -2.7. Looking at the correlation plots for MAPS in **Figure V.13**B, this is exactly what we see for the background corrected cell pixels (noted by the blue line on the left of each individual plot).

Overcompensation by the tail function can be seen by looking again at **Figure V.7** and noting that the total fitted fluorescence directly above the Ar Kα peak is greater than the raw fluorescence. This absolutely necessitates a point where the fitted Ar fluorescence became zero as the fitted K fluorescence continued to increase. This point also agrees with all the values of -2.7 for Ar that are present in the correlation plots in **Figure V.13**. Additionally, since M-BLANK shows a positive correlation of Ar that does not plateau for all other biologically relevant elements, and since that correlation from MAPS shows a negative correlation that plateaus, then if we divided the M-BLANK Ar image by the MAPS Ar image, we should see cells that have a negative ratio at the outer edge of the cell. Moving in to the center of each cell, that negative value should initially remain more or less constant until the MAPS background corrected Ar value plateaus at -2.7 (the background mean). Then the ratio of the two values should steadily decrease in negativity as the M-BLANK values continues to steadily rise due to increased secondary excitation from increased cellular fluorescence; however, it won't ever actually become positive because the MAPS Ar image will be locked at -2.7. This happens and can be seen in **Figure V.16**.

V.5 BIOLOGICALLY RELEVANT DIFFERENCES:

One of the biggest differences between the two programs is the ability to see Cl. This can be understood by looking at **Figure V.18**. At an intensity of 75% of the elastic scattering, the background signal from Cl is the third most intense background signal. The Cl background is ~14-fold more intense than the cellular Cl signal, making quantitation of Cl challenging when a stable blank is used, and problematic when a per-pixel baseline is used due to much larger noise. This can be seen by comparing the correlation plots of Cl with K, P, and elastic scatter from both MAPS and M-BLANK (see **Figure V.19**).

Not surprisingly, given the data in **Figure V.10**, the composition ratios that are calculated from the two different fits are different. **Table V.1** reports the ratios of the mean cellular concentrations for the scans of *Saccharomyces cerevisiae* Zrt1Δ (high affinity membrane importer of Zn) supplemented with and without 100 μM Zn. Although the sample-dependent changes are directly identical (G and H), the apparent element:element ratios are quite different (C and F).

Table V.2 lists the mean cellular concentrations for the scans of *S. cerevisiae* Zrt1Δ (high affinity membrane importer of Zn) with and without supplementation of 100 μM Zn. As expected, the trend noted in **Figure V.10** can be seen in columns C and F. Importantly, column I shows potentially biologically relevant differences in the calculated changes between the two conditions by MAPS and M-BLANK for Zn, Mn, Ca, Cl, and S.

V.6 CONCLUSIONS

Per-pixel baseline fitting makes the precision much worse and, for some elements, appears to also affect the accuracy. Because the fluctuating pixel-to-pixel baseline affects low and high energies differently, system wide parameters, such as FWHM, are changed by the baseline errors. Based on visual comparison alone of Figure V**.7** and Figure V**.8**, M-BLANK provides a level of accuracy, precision and sensitivity that MAPS cannot match. This is best demonstrated with the detection of Cl.

In addition to giving more accurate results, the use of a blank allows for much faster fitting.

V.7 REFERENCES

1. Van Grieken, R.E. and A.A. Markowicz, *Handbook of X-Ray Spectrometry*. 2 ed. Practical Spectroscopy. 2002: Marcel Dekker.
2. Bos, A.J.J., R.D. Vis, and H. Verheul, *Experimental Comparison of Synchrotron Radiation with Other Modes of Excitation of Xrays for Trace Element Analysis.* Nucl. Intruments Methods Phys. Res. Sect. B Beam Interact. with Mater. Atoms, 1984. **3**(1-3): p. 232-240.
3. Gordon, B.M., *North-Holland Publishing Company Sensitivity Calculations for Multielemental Trace Analysis by Synchrotron Radiation Induced X-Ray Fluorescence.* Nuclear Instruments and Methods 1982. **204** p. 223 223.
4. Sherman, J., *Simplification of a formula in the correlation of fluorescent X-ray intensities from mixtures.* Spectrochimica Acta, 1959. **15**: p. 465-470.
5. West, M., et al., *Atomic spectrometry update–X-ray fluorescence spectrometry.* J. Anal. At. Spectrom., 2010. **25**: p. 1503-1545.
6. Knoechel, A., W. Peterson, and G. Tolkeihn, *X-Ray Fluorescence Analysis with Synchrotron Radiation.* Nuclear Instruments and Methods 1983. **208** p. 659-663.
7. Sitko, R. and B. Zawisza, *X-Ray Spectroscopy: Quantification in X-Ray Fluorescence Spectrometry*. 2012. 280.
8. Scruggs, B., et al., *XRF Mapping : New Tools for Distribution Analysis.* Advances in X-ray Analysis, 2000. **42**: p. 19-25.
9. Reid, A.F. and M. Zuiderwyk, *Method and Apparatus for Material Analysis*. 1984: United States.
10. Krause, M.O. and J.H. Oliver, *Natural Widths of Atomic K and L Levels, Kα X-Ray Lines and Several KLL Auger Lines.* J. Phys. Chem. Ref. Data, 1979. **8**(329).
11. Brunetti, A., *A fast fine-grained genetic algorithm for spectrum fitting: An application to X-ray spectra.* Computer Physics Communications, 2013. **184**(3): p. 573-578.
12. Brunetti, A. and T.J. Steger, *X-Ray spectra background fitting by projection onto convex sets.* Nuclear Instruments & Methods in Physics Research Section a-Accelerators Spectrometers Detectors and Associated Equipment, 2000. **441**(3): p. 504-509.
13. Janssens, K., et al., *Accurate evaluation of μ-PIXE and μ-XRF spectral data through iterative least squares fitting.* Nuclear Instruments and Methods in Physics Research Section B: Beam Interactions with Materials and Atoms, 1996. **109–110**(0): p. 179-185.
14. Kataoka, Y., K. Kasai, and H. Kohno, *STUDY OF NET INTENSITY CALCULATION METHOD IN X-RAY FLUORESCENCE ANALYSIS.* Analytical Sciences, 1991. **7**: p. 513-516.
15. Kneen, M.A. and H.J. Annegarn, *Algorithm for fitting XRF, SEM and PIXE X-ray spectra backgrounds.* Nuclear Instruments & Methods in Physics Research Section B-Beam Interactions with Materials and Atoms, 1996. **109**: p. 209-213.
16. McClanahan, T., J. Trombka, and M. Loew, *Automated spectroscopy of X-ray and gamma-ray pulse height spectra using energy space subdivision.* Nuclear Instruments & Methods in Physics Research Section a-Accelerators Spectrometers Detectors and Associated Equipment, 2005. **546**(1-2): p. 176-179.
17. Ren, L.Q., et al., *Background estimation methods for quantitative X-ray fluorescence analysis of gold nanoparticles in biomedical applications.* Biophotonics and Immune Responses Ix, 2014. **8944**.
18. Solé, V.A., et al., *A multiplatform code for the analysis of energy-dispersive X-ray fluorescence spectra.* Spectrochimica Acta Part B: Atomic Spectroscopy, 2007. **62**(1): p. 63-68.
19. Vekemans, B., et al., *COMPARISON OF SEVERAL BACKGROUND COMPENSATION METHODS USEFUL FOR EVALUATION OF ENERGY-DISPERSIVE X-RAY-FLUORESCENCE SPECTRA.* Spectrochimica Acta Part B-Atomic Spectroscopy, 1995. **50**(2): p. 149-169.

20. Yi, L.T., et al., *A new background subtraction method for energy dispersive X-ray fluorescence spectra using a cubic spline interpolation.* Nuclear Instruments & Methods in Physics Research Section a-Accelerators Spectrometers Detectors and Associated Equipment, 2015. **775**: p. 12-14.
21. Thompson, A., et al., *Center for X-Ray Optics and Advanced Light Source: X-Ray Data Booklet*. 3 ed. 2009.
22. Vogt, S., *MAPS: A set of software tools for analysis and viualization of 3D X-ray fluorescence data sets.* J. Phys. IV France, 2003. **104**: p. 635-638.
23. Alfeld, M. and K. Janssens, *Strategies for processing mega-pixel X-ray fluorescence hyperspectral data: a case study on a version of Caravaggio's painting Supper at Emmaus.* Journal of Analytical Atomic Spectrometry, 2015. **30**(3): p. 777-789.
24. Twining, B.S., et al., *Quantifying Trace Elements in Individual Aquatic Protist Cells with a Synchrotron X-ray Fluorescence Microprobe.* Anal Chem, 2003. **75**(15): p. 3806-3816.
25. Baur, K., et al., *Laboratory and Synchrotron Radiation total – reflection X-ray fluorescence: New Perspectives in Detection Limits and Data Analysis.* Spectrochim. Acta - Part B At. Spectrosc., 2001. **56**(11): p. 2049-2056.
26. Sherman, J., *The theoretical derivation of fluorescent X-ray intensities from mixtures.* Spectrochimica Acta, 1955. **7**: p. 283-306.
27. Rousseau, R., *Fundamental Algorithm Between Concentration and Intensity in XRF Analysis.* X-Ray Spectrometry, 1984. **13**(3): p. 115-120.
28. Mantler, M. and H. Ebel, *X-Ray Fluorescence Analysis Without Standards.* X-Ray Spectrometry, 1980. **9**(3): p. 146-149.

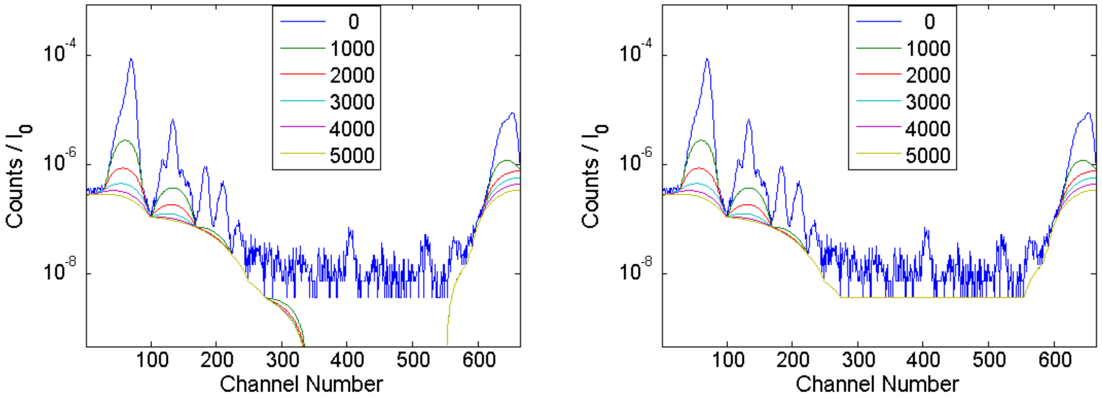

Figure V.1 Snipping Functions: A) Channels with zero counts were included in processing. B) Channels with zero counts were excluded from processing and later interpolated. For both panels, the smooth (colored) lines are the calculated baselines after the indicated number of *different iterations*.

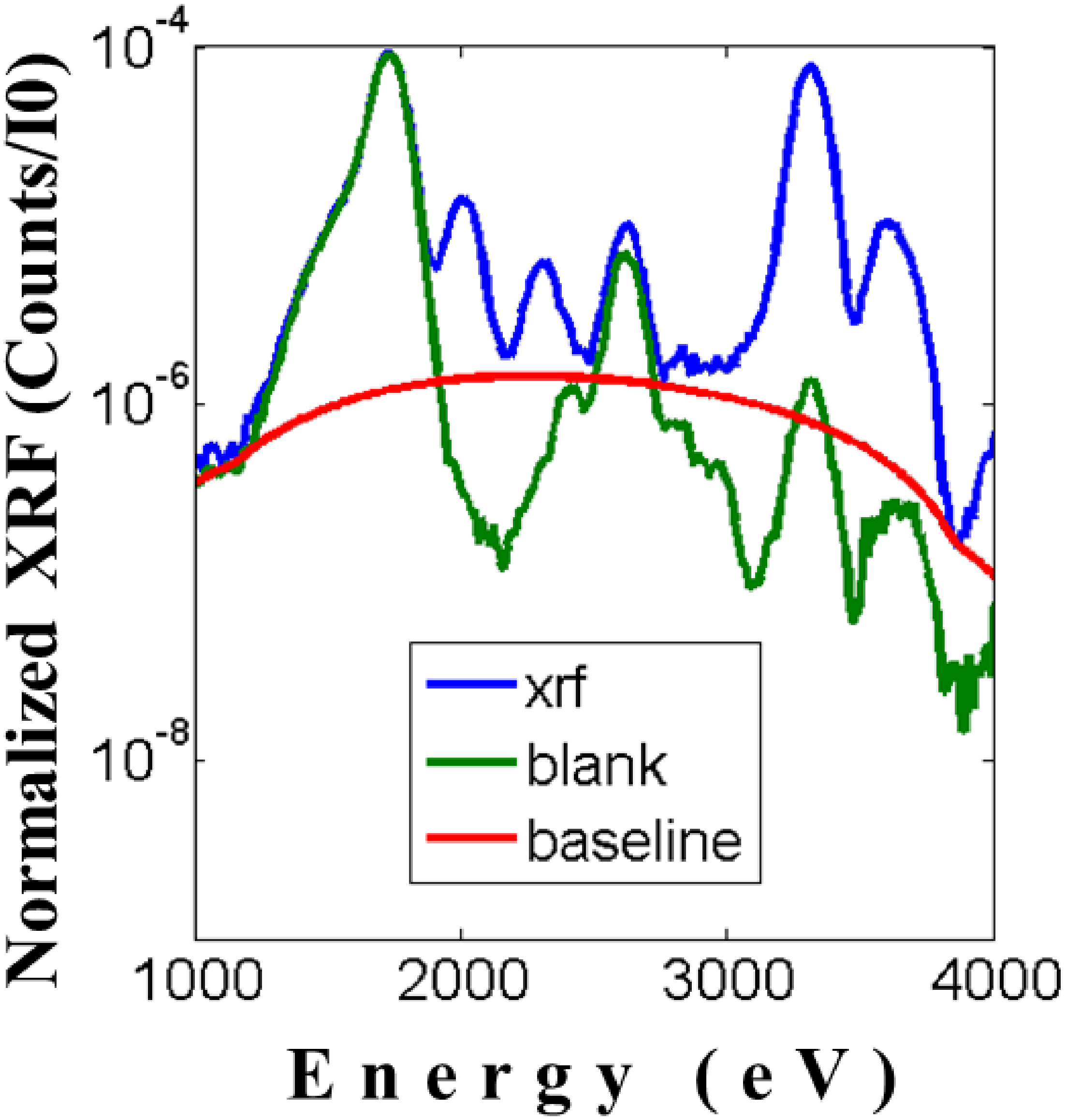

Figure V.2 An Example of Blank and Baseline: Above models the use of a baseline (red) and a blank (green) overlaid on raw XRF (blue).

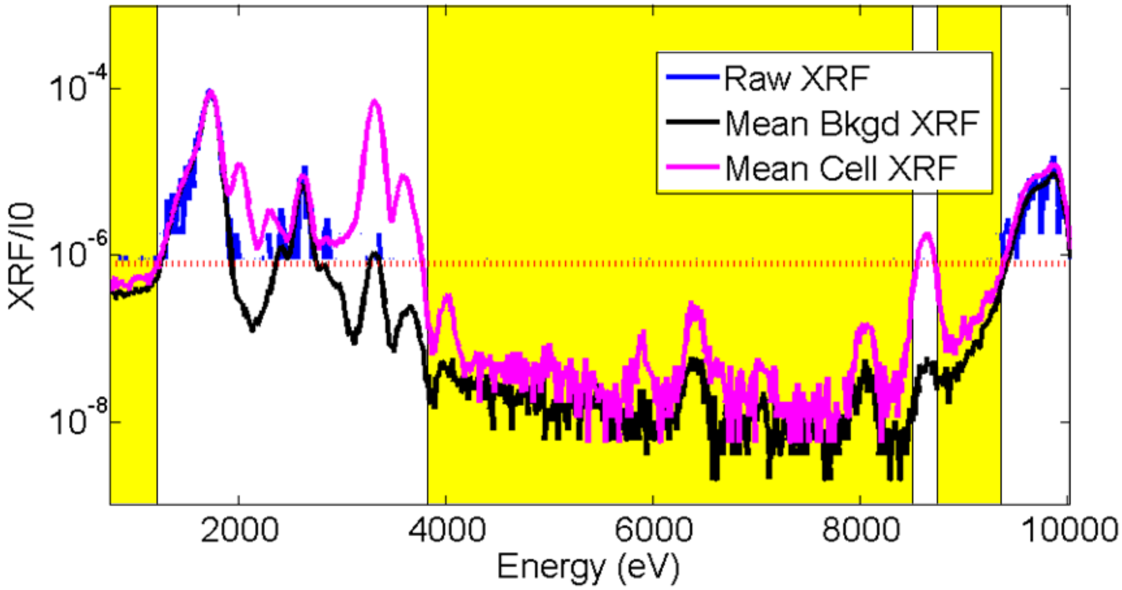

Figure V.3 XRF spectrum of a single pixel: The above spectrum is a single integrated time point from an image taken at Sector 2 ID-E at APS with an integration time of 1.5 seconds. The blue lines crowning the black peaks are actual counts for a single pixel. The black line is the mean spectrum of all non-cell pixels (and is functionally identical to the blank used in M-BLANK). The pink line is the mean spectrum of all the cell pixels. The dashed red line is at 7/8 of one count and marks just below what the detectors sees as one count for the average pixel.

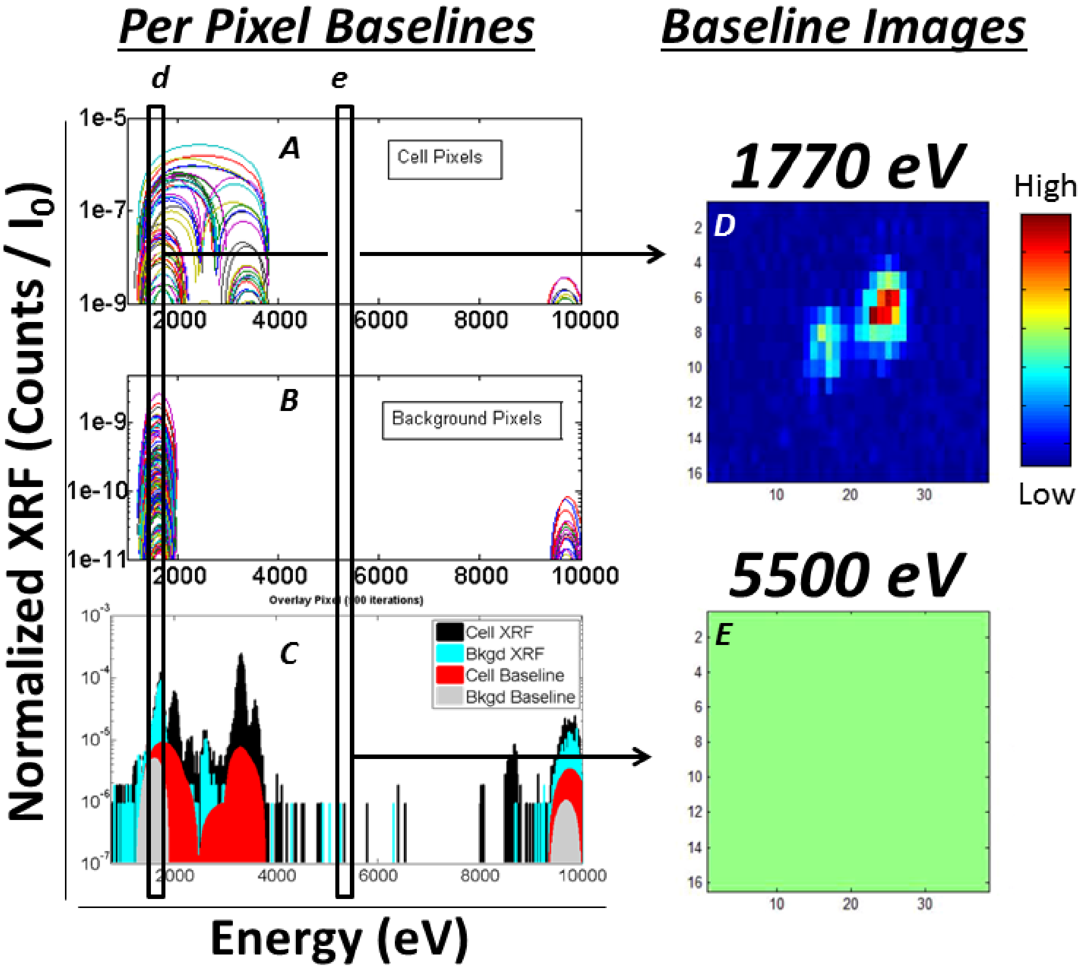

Figure V.4 Per-Pixel Baselines and Baseline Images: All the per-pixel baselines were calculated in M-BLANK for a single image using 500 iterations of a snipping function. (A) and (B) show all the baselines that were calculated for cell pixels and background pixels, respectively. The multiple lines in both A and B represent baselines for *different pixels* and should not be confused with the multiple lines from Figure V.**1** which indicate baselines calculated for the same pixel using *different iteration* number. (C) shows an overlay of raw data from a cell pixel and a background pixel with the associated calculated baseline backgrounds for both. It is not a stacked area plot; rather, the area under each curve was colored to show contrast. (D) is the image generated by summing the baselines contained in box (d) for each pixel. It shows that the four orders of magnitude spanned by the baselines for cell pixels is systematic distributed across the image. Likewise, (E) is the image generated by summing the baselines contained in box (e). Note the uniform nature of the image and the lack of the systematic introduction of noise.

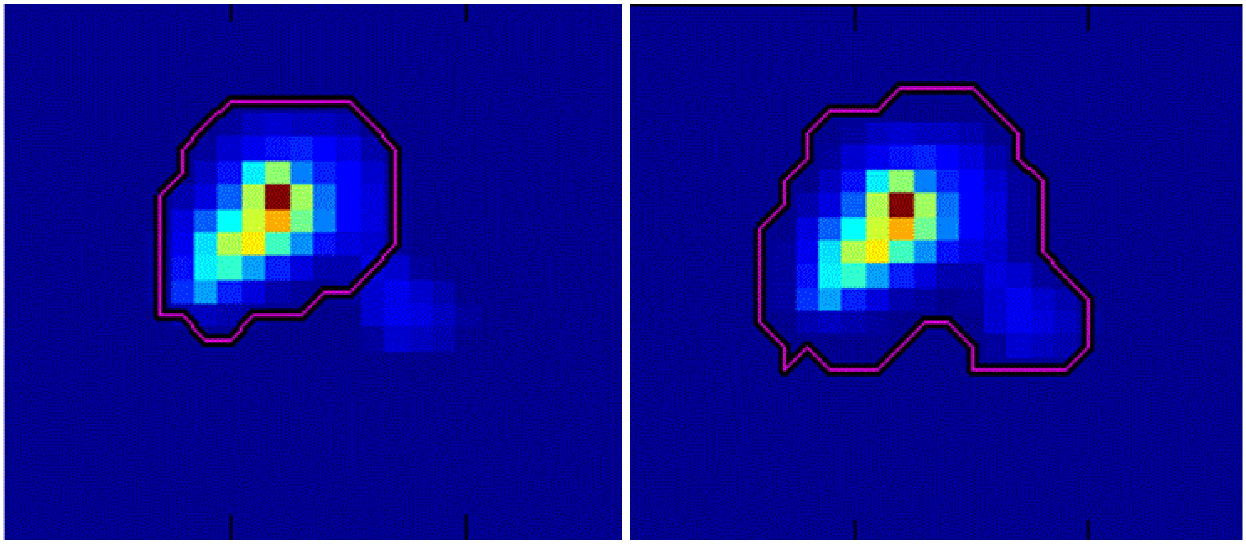

Figure V.5 Correcting ROI Assignment: A) and B) serve as a prototypical demonstration of (A) incorrect cell ROI assignment and (B) the product of manual correction

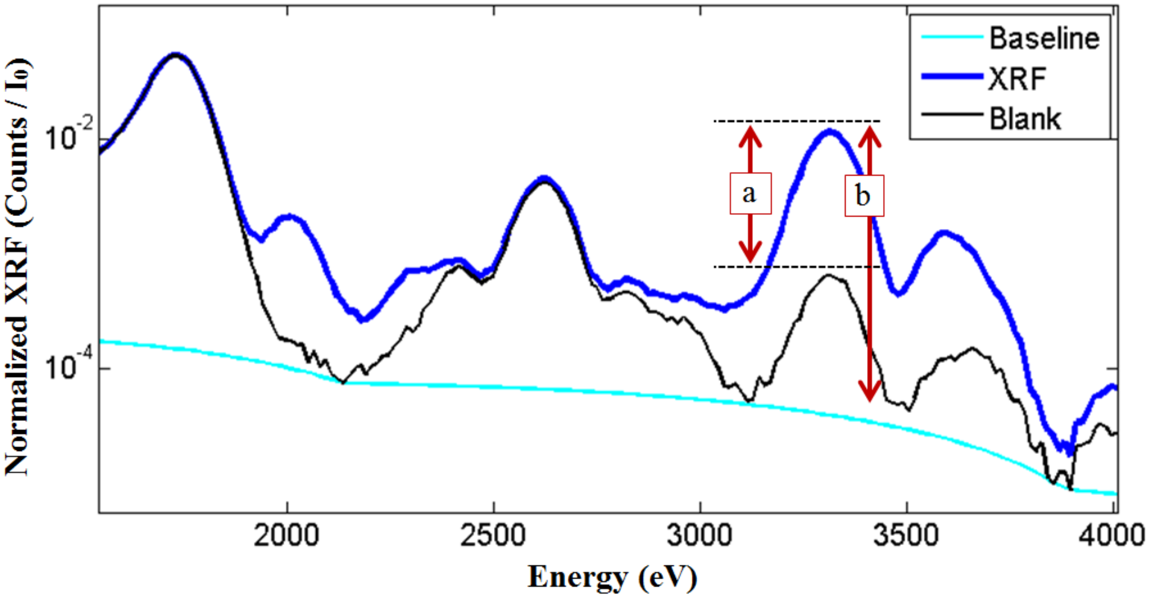

Figure V.6 Comparison of blank corrected data with baseline corrected data: (A) Raw XRF overlaid with the blank and a baseline. (B) The result of correcting the raw XRF in A by the baseline and the blank. (C) The potential error that could arise in calibration between MAPS and M-BLANK if there is a non-negligible blank contribution to the standards.

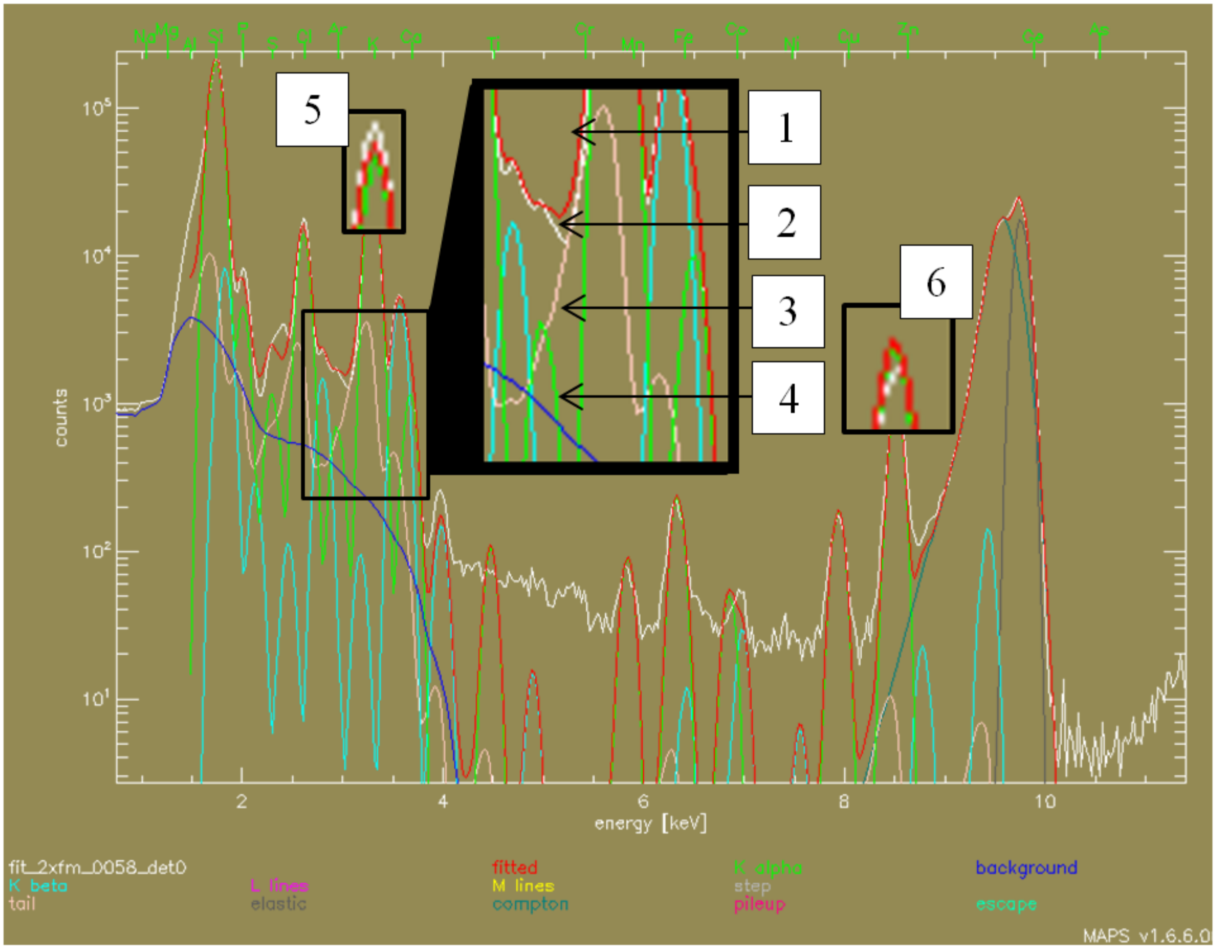

1. Fit to data; 2. Raw data; 3. K step function; 4. Ar Kα; 5. K Peak; 6. Cu Peak

Figure V.7 Prototypical MAPS Fitted Data: The magnified region containing 1-4 shows that the (3) tail function that MAPS uses to account for the low energy end tailing of peaks (most likely due to ramen scatter [26-28] and detector dead space) is overcompensating for the tailing end of K. This can be seen as the function rests right on the (2) raw fluorescence line forcing the (1) fit to data up which causes the (4) Ar Kα to be depressed. Also, note the drop off of the baseline at ~4000 eV affecting the Ca Kβ quantitation. (5) and (6) show the incorrect parameterization of the energy dependence of the FWHM of detector resolution. notice the peaks are too short and wide in (5) and too tall and narrow in (6).

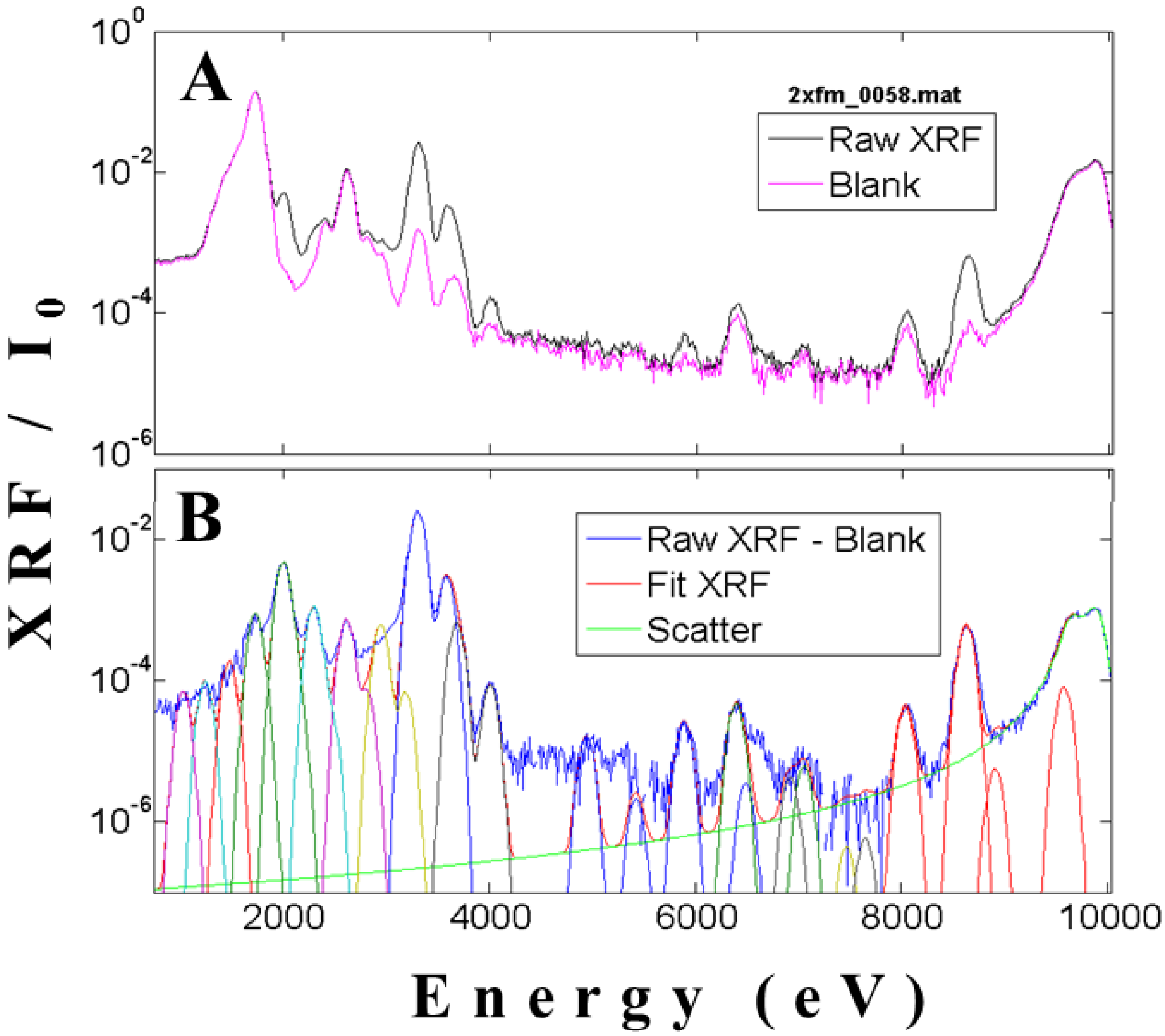

Figure V.8 Representative M-BLANK Fit: For visual comparison to the MAPS fitted data presented in Figure V**.7**, the same data is presented here fitted by M-BLANK. (A) Overlay of the raw XRF with the calculated blank for the integrated spectrum of an image. (B) The blank corrected raw XRF plotted with the fitted XRF for each element, scatter, and the total summed fit.

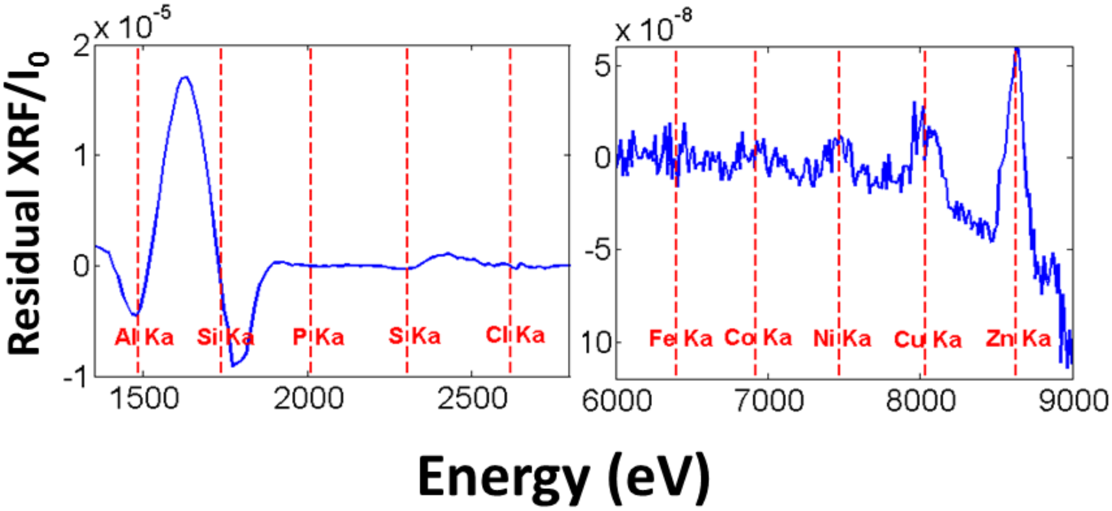

Figure V.9 Residual of Residuals: The total residual spectrum obtained from the fitting of blank corrected data was subtracted from the total residual spectrum obtained from the fitting of that same data corrected with a baseline to give the residual residuals from the two methods. This is plotted above. Both data sets were fit in M-BLANK.

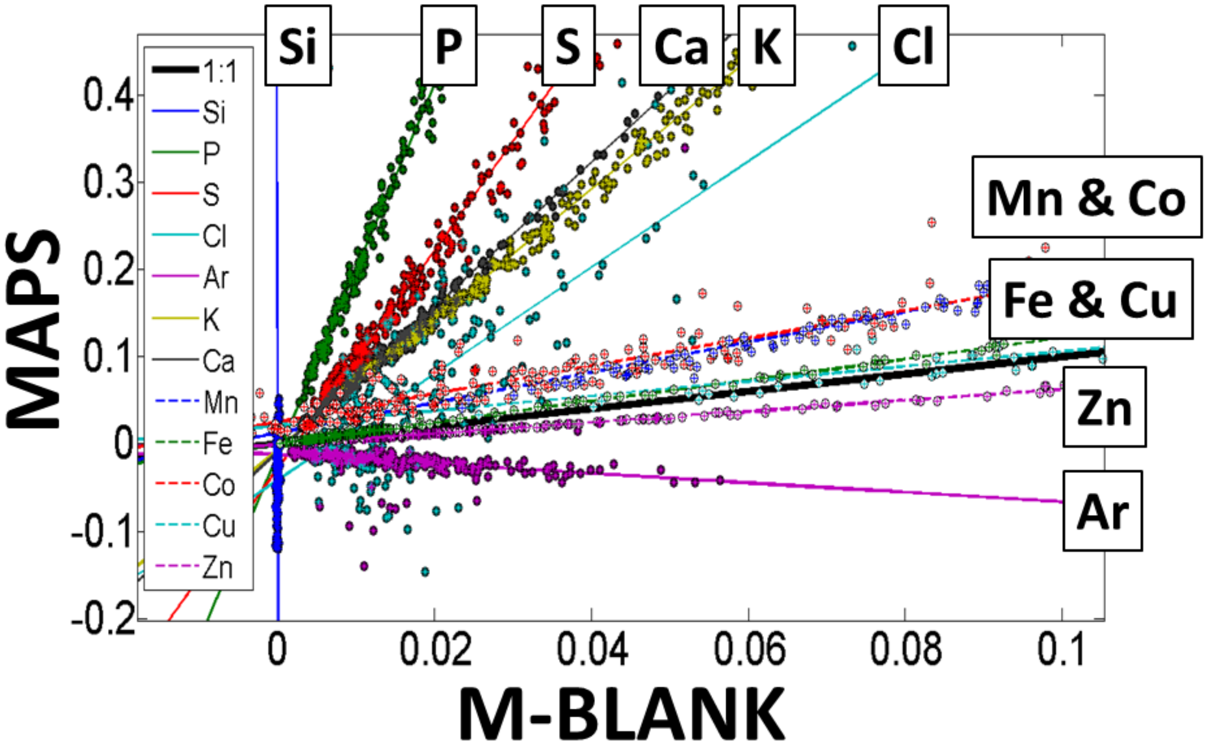

Figure V.10 MAPS Fitted XRF vs M-BLANK Fitted XRF: The values of each element were collectively normalized between -1 and 1 according to the range of values spanned by the combination of both fitted data sets by dividing each by the maximum absolute value from that set. All elements have positive slopes except for Si and Ar. The bold black line marks a 1:1 ratio between the two programs. Any points falling on this line show agreement for that point between the two programs. Points above this line show overestimation by MAPS relative to M-BLANK; points below it show a relative underestimation.

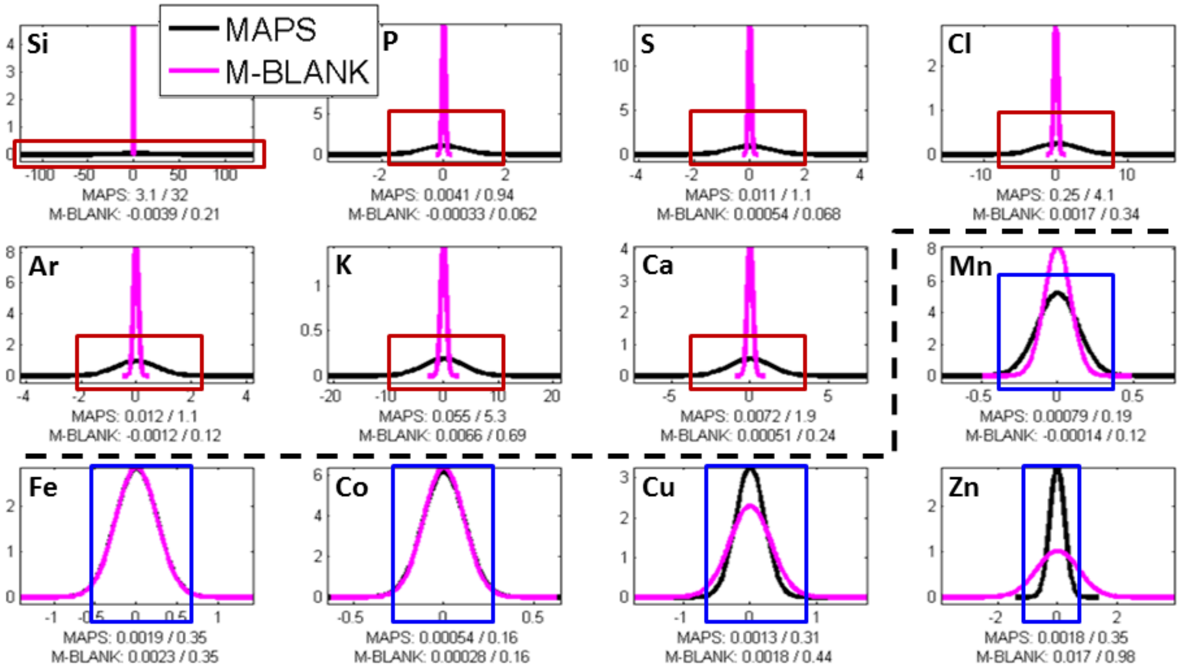

Figure V.11 Fitted Gaussian Distributions for Blank Corrected Background Pixels: The fitted Gaussian distributions for MAPS background pixels were calculated following subtraction of all the pixels for the elemental map by the associated mean for that element. The fitted Gaussian distributions for M-Blank were calculated directly from the fitted background pixels. Both distributions were then normalized to a constant area. The numbers underneath the fitted distribution plots for each element are the *fitted distribution means* followed by the *fitted distribution standard deviations* for both MAPS and M-BLANK.

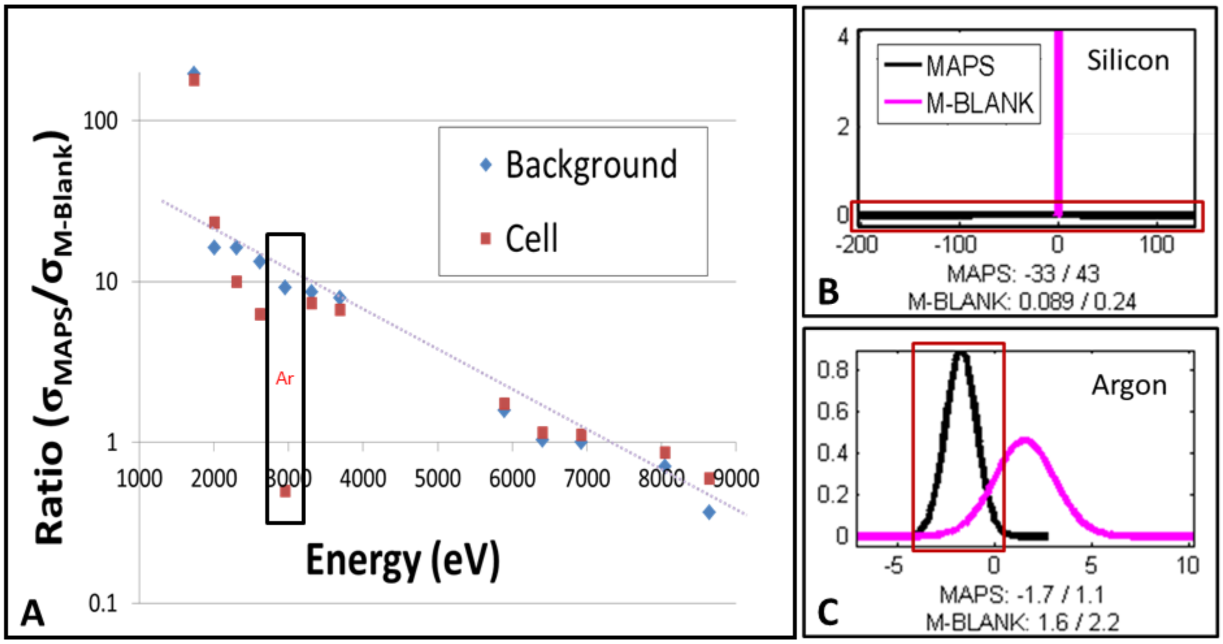

Figure V.12 Distribution Width Ratios and Fitted Gaussian Distributions for Cellular Pixels: A) The ratios of the fitted Gaussian distribution widths (standard deviations) for MAPS are divided by the values from M-BLANK and are plotted vs energy. From left to right, the points correspond to Si, P, S, Cl, Ar, K, Ca, Mn, Fe, Co, Cu, and Zn. Any points falling on the line y = 1 shows agreement between the two programs for that elements fitted Gaussian distribution. Points above this line indicate a lack of precision for MAPS relative to M-BLANK for the associated element; points below the line indicate a relative increase. B) and C) The fitted Gaussian distributions for cellular pixels for Ar and Si respectively. The numbers underneath the fitted distribution plots for each element are the *fitted distribution means* followed by the *fitted distribution standard deviations* for both MAPS and M-BLANK. Importantly, note that the mean value for both are negative for MAPS while they are positive for M-BLANK.

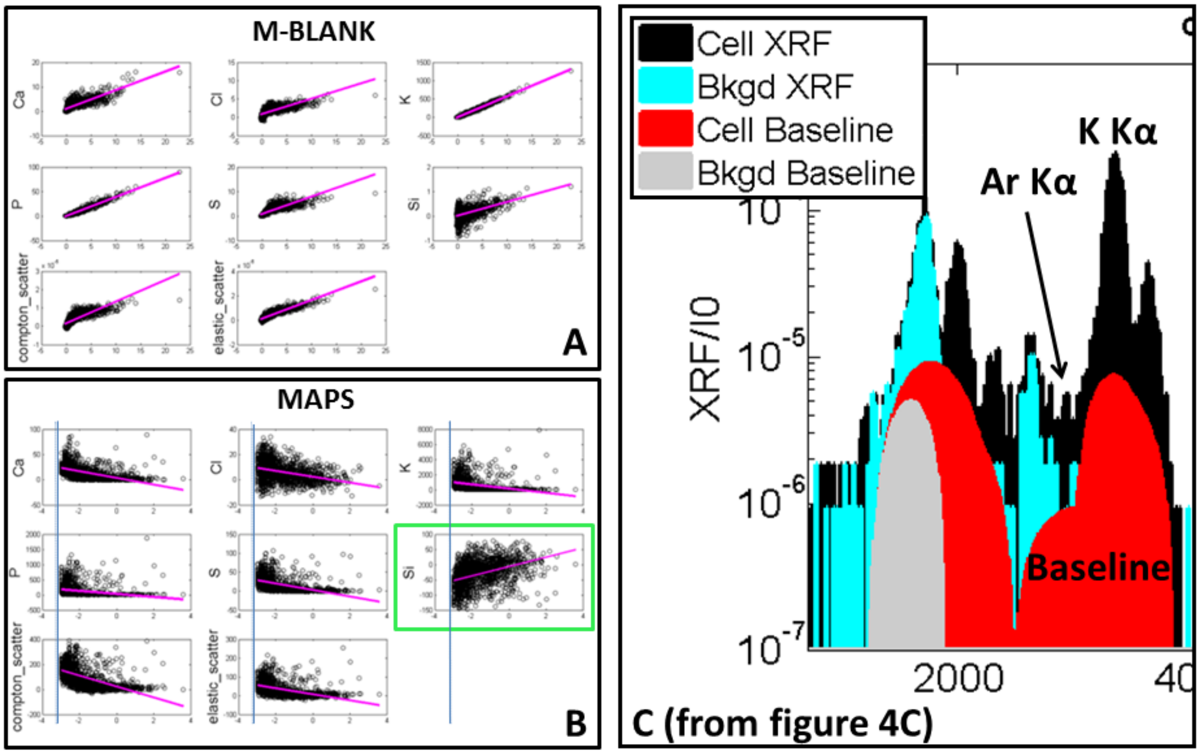

Figure V.13 Per-Pixel Correlation Plots of Ar: The per-pixel correlation plots for Ar with elements <4000 eV are plotted for both M-BLANK (A) and MAPS (B). Ar is plotted to the x-axis of each plot. The blue lines in (B) mark the fitted value of -2.7 for Ar. This value is the mean of the background pixels for Ar. C) Borrowed and cropped from Figure V.**4**C, this illustrates That there is a non-zero baseline for cell pixels in the Ar region, where a zero baseline exists for the background pixels.

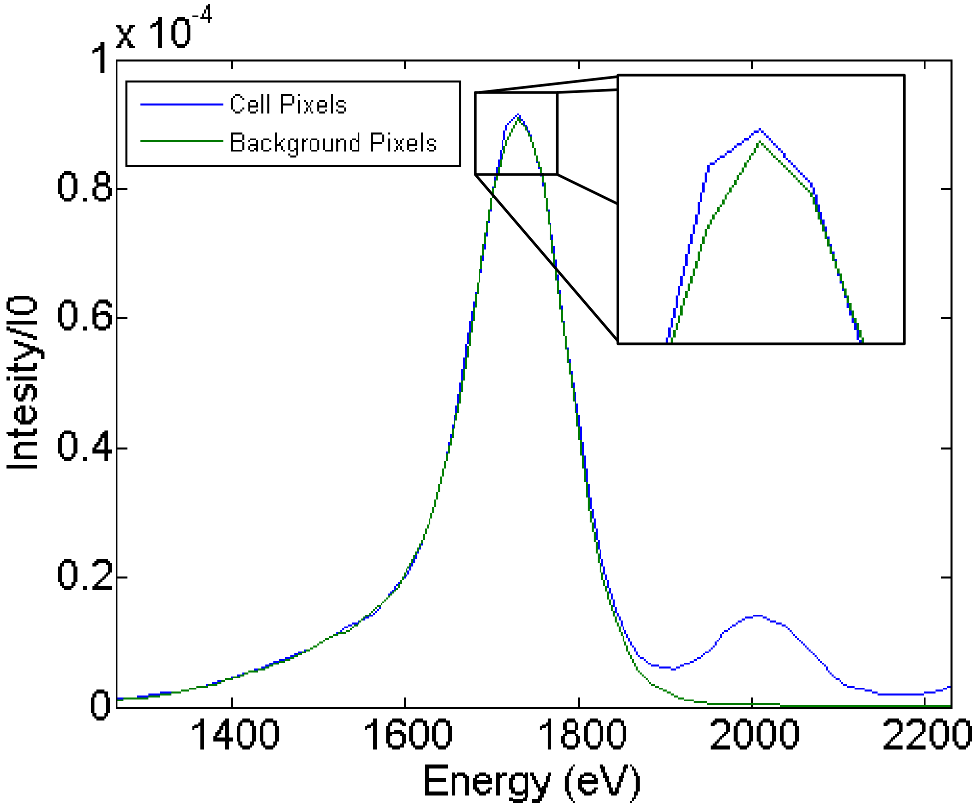

Figure V.14 Raw Cell and Background XRF in the Si Region: The mean raw cellular and background fluorescence are plotted in blue and green, respectively. Importantly, note the positive difference in the Si peak at 1740 eV. It's very small relative to the size of the background signal, however, the background signal is caused by the fact that the sample is sitting on a Si wafer.

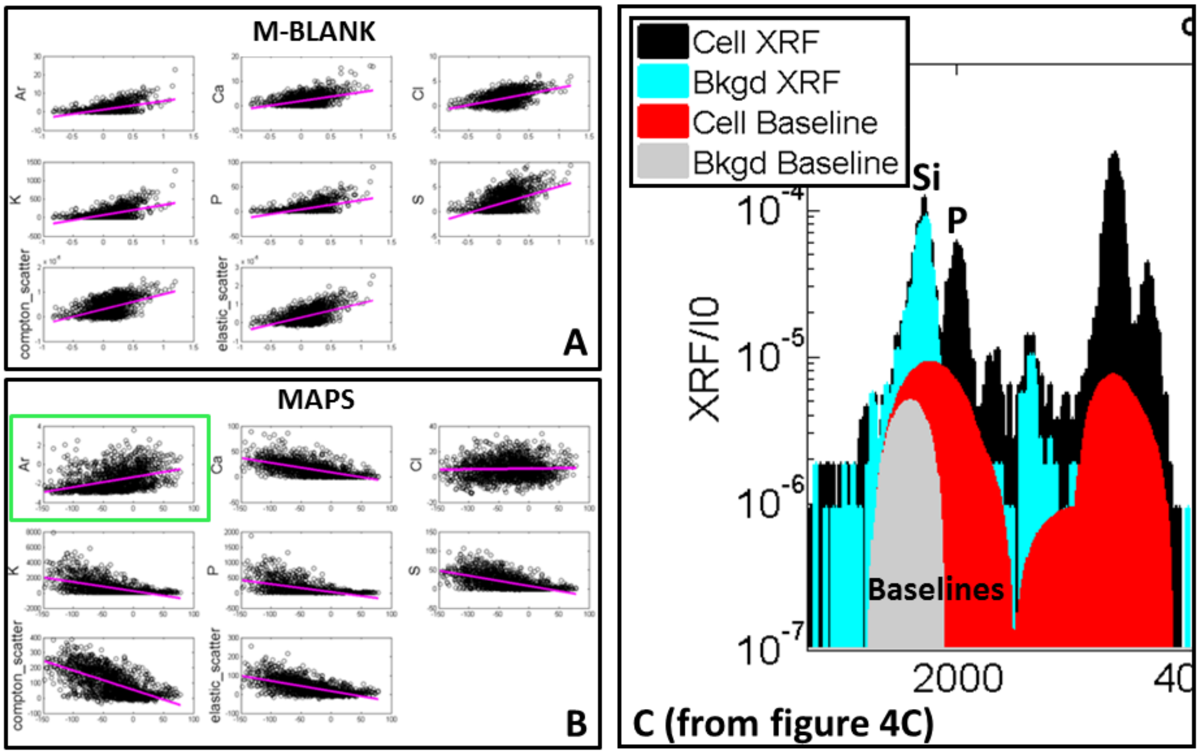

Figure V.15 Per-Pixel Correlation Plots of Si: The per-pixel correlation plots for Si with elements <4000 eV are plotted for both M-BLANK (A) and MAPS (B). Si is plotted to the x-axis of each plot. C) Borrowed and cropped from Figure V.**4**C, this illustrates the increased baseline for cell pixels in the Si region relative to the background pixels.

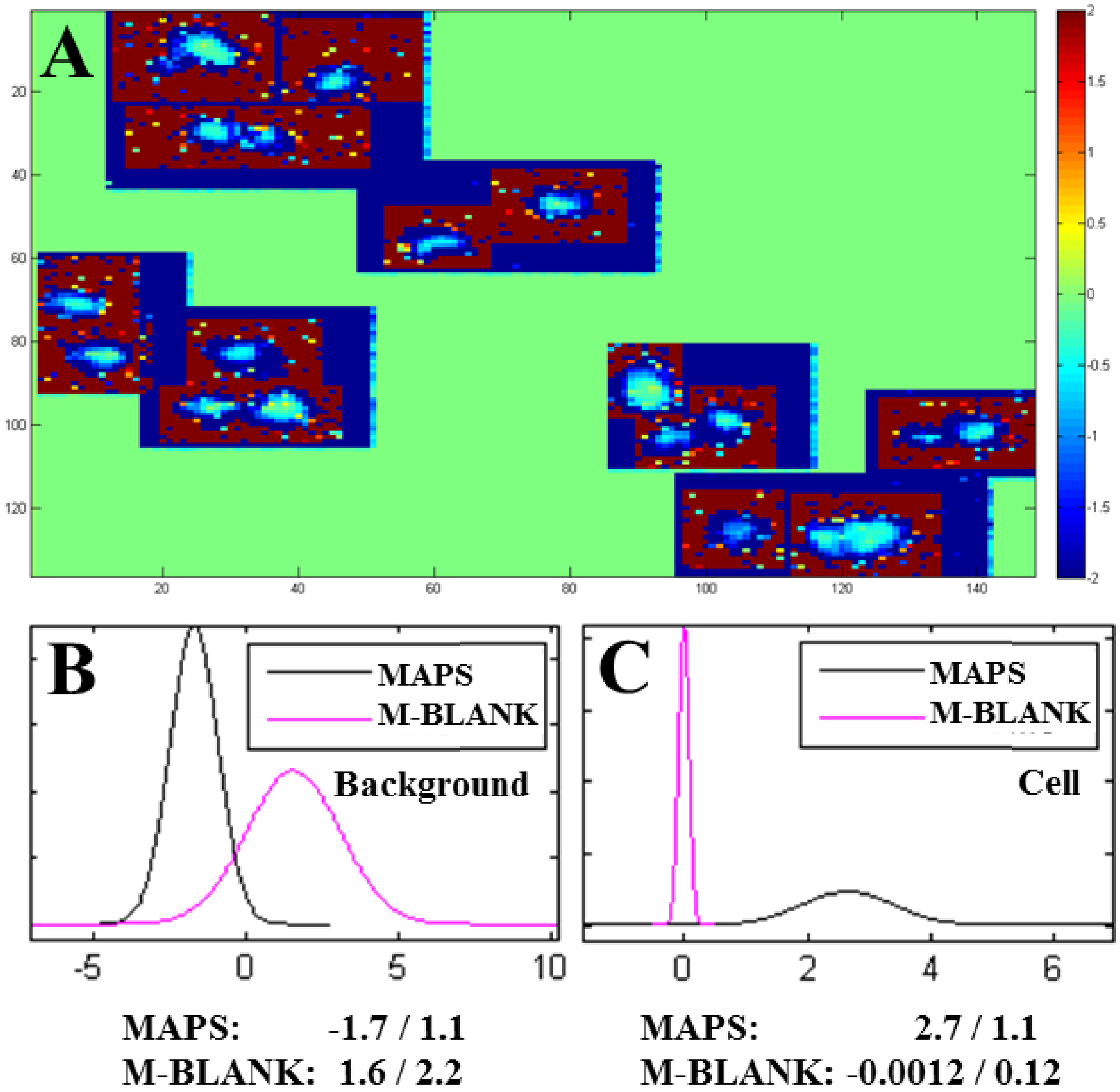

Figure V.16 Imaged Ar Ratios: (A) The image created by taking the per pixel ratio of MAPS:M-BLANK in terms of quantified Ar fluorescence. The bulk green space does not correspond to fitted data; the image was created by stitching together separate fluorescence images to create the slide of samples used at the beam line. Additionally, the range of ratios is much greater than presented. In order to visualize the range of ratios inside the cell, all values greater than 2 or less -2 were set to 2 and -2, respectively. The bottom two images are the Gaussian fitted histograms of fitted Ar fluorescence for the (B) background and (C) cell pixels.

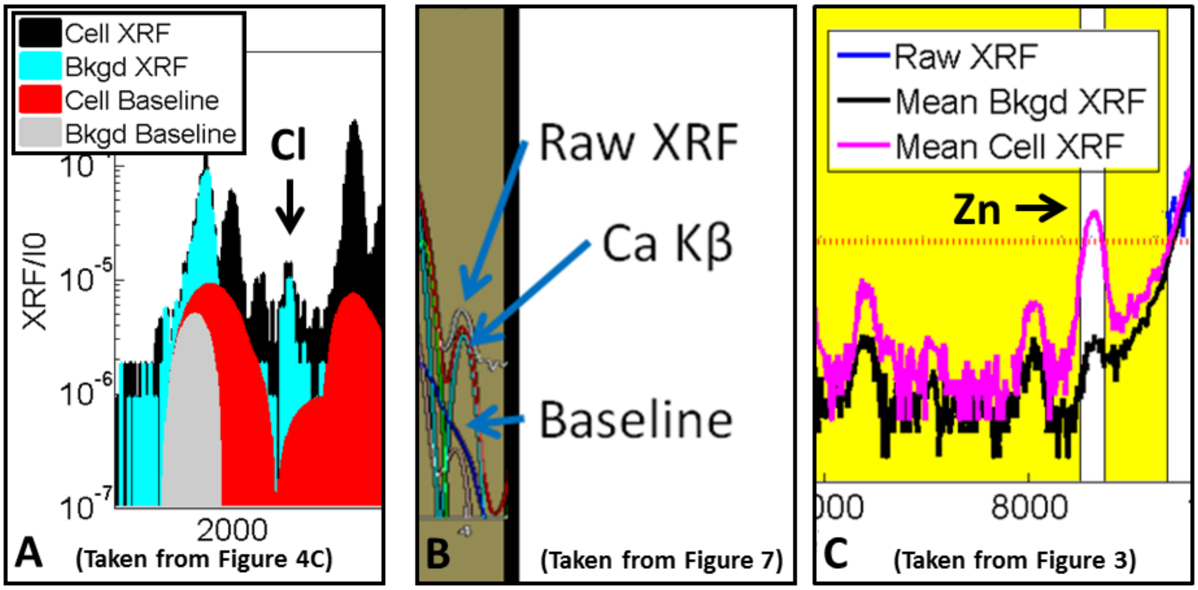

Figure V.17 Trend Non-uniformity: Not all the elements in Figure V**.10** follow the trend of over-estimation to under-estimation by MAPS relative to M-BLANK. A) An increase in the baseline for cellular pixels relative to background pixels could cause a decrease in the quantitation of Cl. B) The fall-off of the baseline at 4000 eV causes an apparent increase in cellular Ca. C) The mean cellular XRF for Zn is above the threshold of probability for being seen by the average cell pixel whereas the mean for the background is much below that probability. This potentially leads to a non-zero baseline for cell pixels while there is most likely a zero baseline for background pixels.

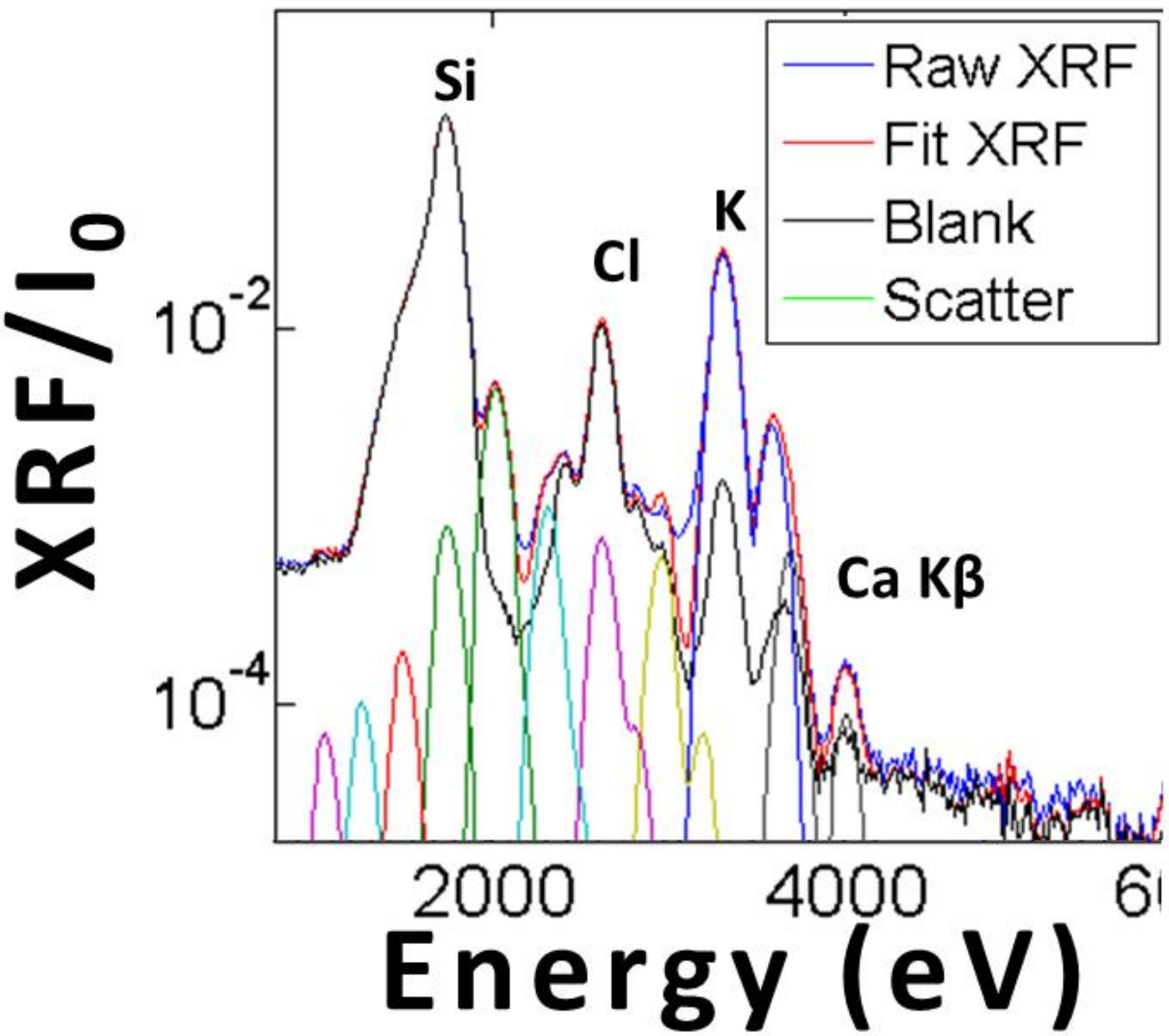

Figure V.18 Chlorine Region from Figure V.8: In addition to raw and overall fitted data, the K_α and K_β peaks that are fitted for each element are shown. It highlights the detectable Cl peak by M-Blank and demonstrates how that signal arises from a very small difference between two very large numbers. The Ca Kβ has been noted for comparison with Figure V.**17**B, the MAPS fit for the same region.

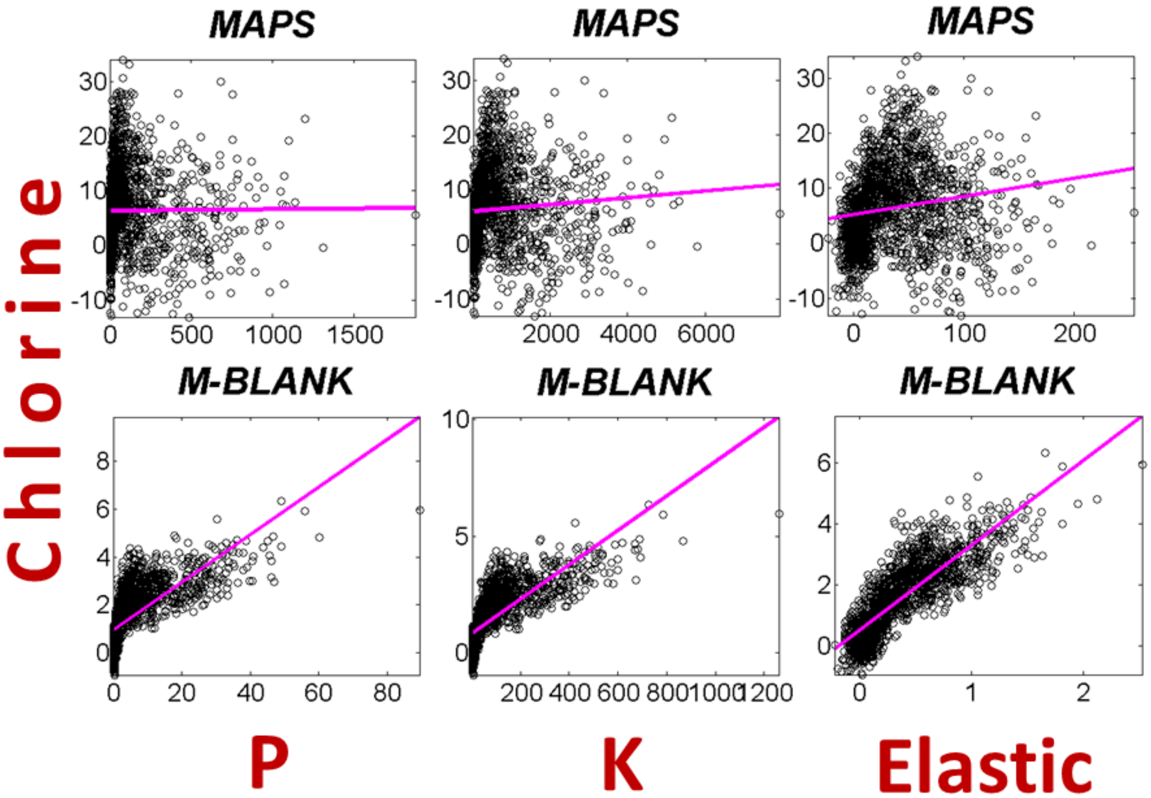

Figure V.19 Cl Correlation Plots: The quantitation of Cl as a function of P, K, and elastic scatter has been plotted for both MAPS and M-BLANK above.

Zrt1 ZLM (+ 100 µM Zn)

A — Ratios: MAPS

	S	Cl	K	Ca	Mn	Fe	Cu	Zn
P	6.6	20.4	0.2	6.8	179	88.8	102	8.6
S		3.1	0.0	1.0	27.3	13.5	15.5	1.3
Cl			0.0	0.3	8.8	4.3	5.0	0.4
K				32.4	855	425	488	41.1
Ca					26.4	13.1	15.0	1.3
Mn						0.5	0.6	0.0
Fe							1.1	0.1
Cu								0.1

B — Ratios: M-BLANK

	S	Cl	K	Ca	Mn	Fe	Cu	Zn
P	3.1	4.1	0.1	2.3	15.8	5.1	4.7	0.2
S		1.3	0.0	0.7	5.0	1.6	1.5	0.1
Cl			0.0	0.6	3.8	1.2	1.2	0.1
K				32.9	222.5	72.2	67.1	3.5
Ca					6.8	2.2	2.0	0.1
Mn						0.3	0.3	0.0
Fe							0.9	0.0
Cu								0.1

C — Ratio of Ratios (MAPS/M-BLANK):

	S	Cl	K	Ca	Mn	Fe	Cu	Zn
P	2.1	4.9	2.9	2.9	11.3	17.4	21.4	34.9
S		2.4	1.4	1.4	5.4	8.3	10.3	16.8
Cl			0.6	0.6	2.3	3.5	4.3	7.1
K				1.0	3.8	5.9	7.3	11.8
Ca					3.9	6.0	7.4	12.0
Mn						1.5	1.9	3.1
Fe							1.2	2.0
Cu								1.6

$$\frac{B}{A}$$

Zrt1 ZLM

D — Ratios: MAPS

	S	Cl	K	Ca	Mn	Fe	Cu	Zn
P	4.5	18.8	0.3	5.5	141.1	128	63.0	3.9
S		4.2	0.1	1.2	31.3	28.5	14.0	0.9
Cl			0.0	0.3	7.5	6.8	3.3	0.2
K				19.8	513	467	229	14.1
Ca					25.9	23.5	11.5	0.7
Mn						0.9	0.4	0.0
Fe							0.5	0.0
Cu								0.1

E — Ratios: M-BLANK

	S	Cl	K	Ca	Mn	Fe	Cu	Zn
P	2.5	4.2	0.1	2.0	13.2	7.9	3.0	0.1
S		1.7	0.0	0.8	5.3	3.2	1.2	0.0
Cl			0.0	0.5	3.2	1.9	0.7	0.0
K				21.3	138	82.5	30.8	1.2
Ca					6.5	3.9	1.4	0.1
Mn						0.6	0.2	0.0
Fe							0.4	0.0
Cu								0.0

F — Ratio of Ratios (MAPS/M-BLANK):

	S	Cl	K	Ca	Mn	Fe	Cu	Zn
P	1.8	4.5	2.9	2.7	10.7	16.2	21.3	32.5
S		2.5	1.6	1.5	5.9	8.9	11.7	17.9
Cl			0.6	0.6	2.4	3.6	4.7	7.2
K				0.9	3.7	5.7	7.4	11.3
Ca					4.0	6.1	8.0	12.1
Mn						1.5	2.0	3.0
Fe							1.3	2.0
Cu								1.5

$$\frac{E}{D}$$

%-Change

G — MAPS

	S	Cl	K	Ca	Mn	Fe	Cu	Zn
P	-31%	-8%	32%	-19%	-21%	45%	-38%	-55%
S		34%	91%	17%	15%	110%	-10%	-34%
Cl			43%	-13%	-14%	57%	-33%	-51%
K				-39%	-40%	10%	-53%	-66%
Ca					-2%	80%	-23%	-44%
Mn						83%	-22%	-43%
Fe							-57%	-69%
Cu								-27%

$$\frac{D-A}{D}$$

H — M-BLANK

	S	Cl	K	Ca	Mn	Fe	Cu	Zn
P	-21%	1%	35%	-13%	-16%	55%	-38%	-51%
S		28%	72%	11%	7%	97%	-21%	-38%
Cl			34%	-13%	-17%	54%	-38%	-52%
K				-35%	-38%	14%	-54%	-64%
Ca					-4%	77%	-29%	-44%
Mn						84%	-26%	-42%
Fe							-60%	-69%
Cu								-22%

$$\frac{E-B}{E}$$

I — Difference (M-BLANK - MAPS):

	S	Cl	K	Ca	Mn	Fe	Cu	Zn
P	10%	9%	4%	7%	5%	10%	0%	3%
S		-6%	19%	-6%	-8%	-13%	-11%	4%
Cl			-9%	-1%	-2%	-3%	-5%	-1%
K				3%	2%	5%	-1%	2%
Ca					-2%	-3%	-6%	-1%
Mn						1%	-4%	1%
Fe							-3%	0%
Cu								5%

$$H-G$$

Table V.1Comparison of Elemental Ratios: The numbers in the red boxes highlight significant changes between the two fitting programs that could lead to biologically different conclusions. The ratios of the mean cellular concentrations for the scans of *Saccharomyces cerevisiae* Zrt1Δ (high affinity membrane importer of Zn) supplemented with 100 μM Zn are represented for MAPS (A) and M-BLANK (B). (C) The ratios MAPS (A)/M-BLANK(B). Likewise, (D), (E), and (F) are the same analyses for *S. cerevisiae* Zrt1Δ without Zn supplementation. (G and H) are the percentage differences for the two conditions as seen by MAPS and M-BLANK, respectively. The differences of those differences between the two fitting programs are reported in (I).

	Differences in Quantitation								
	Zrt1 ZLM (+ 100 µM Zn)			Zrt1 ZLM			Change		
Element	MAPS	M-BLANK	% Difference	MAPS	M-BLANK	% Difference	MAPS	M-BLANK	% Difference
P	3.7E-01	1.8E-02	2020%	3.4E-01	1.6E-02	2016%	-8%	-8%	0%
S	5.7E-02	5.6E-03	918%	7.6E-02	6.6E-03	1062%	33%	17%	16%
Cl	1.8E-02	4.3E-03	329%	1.8E-02	3.9E-03	368%	-1%	-9%	8%
K	1.8E+00	2.5E-01	619%	1.2E+00	1.7E-01	637%	-30%	-32%	2%
Ca	5.5E-02	7.6E-03	629%	6.3E-02	8.0E-03	690%	14%	5%	9%
Mn	2.1E-03	1.1E-03	87%	2.4E-03	1.2E-03	98%	16%	9%	7%
Fe	4.2E-03	3.5E-03	22%	2.7E-03	2.1E-03	30%	-37%	-41%	4%
Cu	3.7E-03	3.7E-03	-1%	5.5E-03	5.5E-03	-1%	48%	48%	0%
Zn	4.4E-02	7.2E-02	-39%	8.9E-02	1.4E-01	-35%	103%	89%	14%
	A	B	C = [A-B]/B	D	E	F = [D-E]/E	G	H	I = G-H

Table V.2 Differences in Calculated Mean Concentrations: The mean cellular concentrations for the scans of *Saccharomyces cerevisiae* Zrt1Δ (high affinity membrane importer of Zn) with and without supplementation of 100 µM Zn are represented for MAPS (A and D) and M-BLANK (B and E). (C and F) are the percent differences relative to M-BLANK between the two programs. (G) and (H) report the percentage change between the two conditions observed by MAPS and M-BLANK, respectively. (I) is the difference reported for those changes between MAPS and M-BLANK.

CHAPTER VI: BIONANOPROBE, FIBROBLASTS, AND SPECTRAL FILTERING[4]

VI.1 INTRODUCTION

Previous studies using XRF imaging have examined the effect of Cd on metal homeostasis in yeast. In an attempt to expand this work to other species, freeze dried mouse fibroblasts (NIH3T3) cells were studied in 2010. Surprisingly, the cells showed significant Cu contamination and, for most of the cells, a nucleus that appeared to contain almost no metal. In order to test these results, new studies were undertaken on mouse fibroblasts (NIH3T3) cells, but not dried cells. In contrast with earlier work, on freeze dried cells, these measurements were done at low temperature on plunge frozen cells, which retain the original cell structure.

---

[4] Lubomir Dostal was lead on this project. I was present at data collection and performed the fitting and analysis. Jim Penner-Hahn provided guidance during analysis. This research used resources of the Advanced Photon Source, a U.S. Department of Energy (DOE) Office of Science User Facility operated for the DOE Office of Science by Argonne National Laboratory under Contract No. DE-AC02-06CH11357. "This project was supported by grant 9 P41 GM103622 from the National Institute of General Medical Sciences of the National Institutes of Health." The content is solely the responsibility of the authors and does not necessarily reflect the official views of the National Institute of General Medical Sciences or the National Institutes of Health.

Imaging experiments at such low temperatures are made possible by the Bionanoprobe (undulator beamline, Sector 21, Advanced Photon Source, Argonne National Lab, Lemont, Illinois, USA) [1]. This instrument is an x-ray fluorescence nanoprobe with a cryogenic sample environment and cryo transfer capabilities specifically designed for studying frozen, hydrated, biological samples. This probe permits imaging of hydrated cells and therefore avoids structural deformation of cells due to collapse and cell shrinkage associated with freeze drying. This preserves the ultrastructure of cellular organelles.

There have been many advances over the years in the analytical approaches and methodologies used to fit x-ray fluorescence data sets. Chapter 5's M-BLANK comparison touched on some of those advances, particularly those having to do with background estimation and data fitting. The fitting of mouse fibroblasts in this study presented an additional opportunity. In the course of applying M-BLANK to imaging studies of NIH3T3 cells, I believe I have been able to identify an issue related spectral filtering of raw XFR data sets using single value decomposition (SVD) [2] to reduce noise.

The application of SVD filtering of raw XRF data sets to reduce noise is based on the fact that correlations between the different elements from pixel-to-pixel should exist; whereas noise should not be correlated. Therefore, performing SVD and then selecting the optimum number of eigenvectors and reconstructing the spectra based on those values, should, in principle, retain all of the actual elemental signals while filtering out noise.

VI.2 EXPERIMENTAL

VI.2.1 SAMPLE PREPARATION

NIH3T3 cells were grown in complete medium (CM) containing DMEM (Invitrogen) and 10% calf serum (Gibco) at 37 C° and 5% CO_2 until confluency. Cells were then detached using 0.05% trypsin, EDTA solution (Invitrogen). Then 100,000 cells per well were plated in CM containing 2 to 3 Si_3N_4 slides. After 24 hours cells were washed with PBS and DMEM containing 2% bovine serum albumin (BSA) was added for 24 hours. Then BSA containing medium was removed and cells were exposed to 2 or 0 μM $CdCl_2$ in DMEM for 6 hours. Finally cells were exposed to 1 μg/ml Hoechst 33324 for 25 minutes followed by plunge freezing. Plunge freezing was performed using FEI Vitrobot in liquid ethane and cells were kept in liquid nitrogen until BNP measurement.

VI.2.2 PARAMETER DETERMINATION AND FITTING

Fitting parameters were determined using a sample scan by fitting the MCA for the cellular region of a scan using the methodologies discussed in Chapter 3. As discussed in Chapter 5, a blank was subtracted rather than a baseline. Following this, both the samples and the standards were fit using those parameters as discussed in Chapter 3.

VI.2.3 DETECTOR ELEMENTS 1 AND 2

The scans taken at the Bionanoprobe (BNP) utilized a four element detector. In the course of our analysis, it was discovered that elements 1 and 2 were sporadic and unreliable. For instance, across all scans and all pixels, detector elements 1 and 2 gave mean count rates with associated standard deviations that were, on average, 300% of the count rate. In contrast, detector elements 3 and 4 gave highly reproducible count rates with relative standard deviations on the order of 15%. As such, all data from detector elements 1 and 2 were discarded from all analyses.

VI.2.4 IMAGE FILE MANIPULATION

The data sets contained 2048 channels of fluorescence, with the first ~800 channels reflecting energies below ~10 keV. To reduce memory requirements, files were reduced by cropping the extra channels. Some large cells were imaged in parts across multiple scans at the beamline. In these cases, small overlapping regions of each scan were used to stitch the fitted data from the separate scans into a single image for subsequent analyses.

The x-, y-coordinates of all the images corresponding to each slide were used to stitch the individual cell images into a single image using the K channel, and these were matched to the bright field images of the slides taken at APS.

VI.2.5 MxM DIGITAL BINNING OF DATA SETS

Digital binning of the data was performed to increase the signal-to-noise ratio and decrease the memory requirements of the associated computations. This was done by taking all the pixels in an MxM neighborhood and summing the counts for each of the channels into a single value. For the data analyzed in this chapter, digital binning was performed for 5x5, 10x10, 15x15, and 20x20 neighborhoods corresponding to effective pixel sizes of 2.5, 10, 22.5, and 40.0 μm^2. This increased the signal-to-noise ratio, and gave faster processing as a result of the reduced size of the data set, thus allowing for the analysis of the different modes of blank/background calculations discussed in section VI.2.6. Quantitation of each element fitted from the binned data sets was identical to that found with the unbinned data.

VI.2.6 BLANK CALCULATION

Blanks were calculated from the background pixels of each image using the K-Kα emission line to generate a raw image of the cell using an ROI centered on the K Kα line. This was then used to identify the background pixels as those with low K; these pixels were used to calculate the blank. For two of the five scans, there were small groups of pixels that contained large amounts of contaminant Fe, Cr, Cu, Mn, and/or Ni, with amplitudes ~10,000X greater than other pixels (see **Figure VI.1**). Those pixels were removed from the data set prior to fitting and analysis.

Initially, we assumed that the background had a constant shape but might be adjusted by a scale factor. However, allowing for a scale factor caused an apparent gradient in concentration of all of the elements (see Fe-1 in **Figure VI.1**), presumably due to variability in the true Si signal causing variability in the background. A uniform blank gave the images Fe-2 and Si-2. Note the loss of the gradient in Fe-2 and the increase of the gradient for Si-2. Importantly, the size of the gradient in the Fe signal is sufficiently large that it overwhelms the true Fe signal. Only when a fixed, uniform background is used are we able to see the expected presence of Fe in the cytosol (compare Fe-1 and Fe-2 in **Figure VI.1**).

The effect of the background on the total I_0 normalized cellular counts per second is shown in Table VI.**1**. For intense signals, e.g., K, P, Zn, and S, there is < 1% change. In contrast, for Cl, Mn, Fe, and Cu, the differences were 2.8%, 9.2%, 16%, and 2,500%, respectively. In all cases, there is an increase in the amount of metal that appears to be contained within the cell boundaries. The underestimation that is seen when a variable background scale factor is used is a consequence of the small amount of each element that is present. Our unconstrained fits allow both position and negative values fr each element. For Cu, the gradient (negative to the left, positive to the right) completely overwhelms the true Cu signal, making it appear that no Cu is present. While the details of this error will vary, depending on the nature of the Si gradient, the effect will always be to significantly perturb the quantitation.

VI.3 RESULTS

VI.3.1 CELLULAR ELEMENTAL CONTENT OF Cd(-) CELLS

The approximately circular region in the cell with the highest K was assigned to be the nucleus. Although it is difficult to see Cu in the cell in the unbinned data, 20x20 binning shows a slight Cu signal from the cell. A two-tailed t-test comparing the means of the cell pixels to the background pixels yielded p-values of <0.001 for Cu suggesting that cellular Cu concentration is, as expected, above background level.

Visual analysis of the Cd(-) cells (the top set of images in Figure VI**.3**) shows that most of the Fe and Mn are outside the nucleus with Mn being localized to the periphery of the nucleus and Fe being distributed uniformly. The localization of Mn appears to be in the shape of what one might expect of a mitochondrion. Such localization would be consistent with a study of human fibroblasts by Crosti et al [3] which showed a >7:1 ratio of MnSOD in the mitochondria relative to the nucleus. Cl shows a distribution that is similar to that of Fe, with higher concentration in the cytoplasm and lower concentration in the nucleus. K and Zn reside in the nucleus with P residing primarily in the nucleus but with a greater degree of distribution throughout the rest of the cell than either K or Zn. S appears to have the most uniform distribution throughout the cell.

VI.3.2 EFFECT OF CD TREATMENT

Visual comparison of Cd(+) cells to the Cd(-) cells shows changes for Cl, Mn, and P. Cl and P appear to increase in concentration in the nucleus while Mn appears to decrease in concentration at the external periphery of the nucleus. To quantify these observations, we normalized the metal composition to cellular content, using K as a surrogate for total cellular material. While K is not equivalent to cellular content, this should still normalize for many of the factors that come into play when comparing two cells (e.g., the size of the cell, the area, the mass cancel out). Table VI.2 shows statistically significant changes for many of the elements. Specifically, Cd(+) cells, when compared with Cd(-) cells, show increased cellular concentrations for S and Cl (both with P-values < 0.05) and decreased cellular concentrations for Zn (P-value < 0.01); see Table VI.2A. Since S and Cl increase while Zn decreases, these changes cannot arise solely from changes in cellular K. Looking at the nucleus and cytosol separately (Table VI.2B and Table VI.2C), it seems possible that these changes are not uniform across the cell. The Cd treated cells appear to be somewhat smaller, consistent with growth inhibition by Cd.

VI.3.3 SPECTRAL FILTERING

It has been suggested [2] that principal-component filtering can be used to improve the accuracy of pixel-by-pixel fitting. In this approach, PCA is used to identify the dominant eigenvectors for fluorescence, and these alone are used in subsequent analyses. While it is true that PCA does remove high-frequency noise, we find that it can severely distort the resulting quantitation. This can be seen in the comparison of PCA-filtered per-pixel fits for 3T3 cells (**Figure VI.4**, left elemental images) and the results from per-pixel M-BLANK fits for the same data (**Figure VI.4**, right elemental images). While the qualitative appearance for K is independent of fitting method, the other elements (e.g., Mn, Fe, P, Cl, S) are significantly perturbed. With PCA-filtering, the Mn appears to be distributed throughout the nucleus, while for M-BLANK fits, the Mn is localized, as expected, to a region outside of the nucleus that resembles the appearance of the mitochondria. This may explain published reports [4] showing Mn to be distributed throughout the nucleus in NIH3T3 cells. Importantly, the total amount of Mn both slightly increases and becomes very localized to the periphery of the nucleus. Although the effect is most dramatic for Mn, every element showed artificially increased localization to the nucleus in the PCA filtered images relative to unfiltered images.

Figure VI.5 would suggest that a large number of components are needed to define the data set. Greater than 100 eigenvectors are required to account for differences in the data. Furthermore, given the continual fall off of the residuals, it doesn't seem as if there is a clear distinct cut off between signal and noise.

VI.3.4 DISCUSSION AND CONCLUSION

Prior work with NIH3T3 cells under similar conditions using ICP to perform bulk measurements showed decreased concentrations of both Zn and Mn when cells were exposed to Cd [5]. The present work extends those observations to the single cell level. Our observations are broadly consistent with bulk measurements. We see a 36% mean decrease in cellular Zn for Cd doped cells, identical to that seen in ICP studies. Comparison of our mean values for Fe, Cu, and Mn to those reported in [5], show ratios of 0.1, 0.5, and 0.2 for Fe, Cu, and Mn, respectively. This decrease in absolute quantitation may reflect cell-to-cell variability (we studied only 3 cells) or may reflect a systematic calibration error. However, this will not affect the Cd dependent relative changes in composition.

This study demonstrated the potential dangers of using PCA filtering for raw data noise removal. Doing so was shown to drastically change the apparent localization of all elements except for K, with a spurious increase in the apparent concentration of each element in the nucleus. For Mn and Fe, this gave completely wrong results as both tend to be dominantly outside of the nucleus.

We appear to have been able to detect Mn in the mitochondria. This would be consistent with literature [3, 6-9], and the ROIs containing Mn in this study look very similar to the localization of mitochondria and the Golgi apparatus in fibroblasts seen previously [4, 10]. In order to test this hypothesis, these measurements should be repeated using fluorescent labels to identify the mitochondria.

All five cells look roughly the same, and the Cd (+) cells have lower Zn/K. This is consistent with ICP confirms (albeit with low N) the results found in bulk measurements. This rules out, the alternative explanation of the bulk data, which would have been that some cells lost all Zn (*i.e.*, were "ghosts") while other cells were unaffected. There are hints that Cd treatment also causes increase in cellular S/K and Cl/K, increased areal concentrations of S and P in the nucleus, and increased areal concentrations of K, P, S, and Cl in the cytosol. Future studies should attempt to confirm these with more cells.

Finally, in addition to the follow studies from Chapter 5 to verify the differences between M-BLANK and MAPS, the differences noted in this chapter pertaining the use of PCA filtering necessitate follow up as well.

VI.4 REFERENCES

1. Chen, S., et al., *The Bionanoprobe: hard X-ray fluorescence nanoprobe with cryogenic capabilities.* Journal of Synchrotron Radiation, 2014. **21**: p. 66-75.
2. Vogt, S., J. Maser, and C. Jacobsen, *Data analysis for X-ray fluorescence imaging.* J. Phys, 2003. **IV**(104): p. 617-622.
3. Crosti, N., et al., *Coordinate Expression of MnSOD and CuZnSOD in Human Fibroblasts.* Experimental Cell Research, 1985. **160**: p. 396-402.
4. McRae, R., et al., *Correlative microXRF and optical immunofluorescence microscopy of adherent cells labeled with ultrasmall gold particles.* Journal of Structural Biology, 2006. **155**(1): p. 22-29.
5. Dostal, L., et al., *Fibroblasts From Long-Lived Rodent Species Exclude Cadmium.* J Gerontol A Biol Sci Med Sci, 2013.
6. Whittaker, J.W. and M.M. Whittaker, *Active Site Spectral Studies on Manganese Superoxide Dismutase.* J. Am. Chem. Soc., 1991. **113**: p. 5528-5540.
7. Holley, A.K., et al., *Manganese Superoxide Dismutase: Guardian of the Powerhouse.* Int. J. Mol. Sci., 2011. **12**.
8. Sheng, Y., et al., *Comparison of Two Yeast MnSODs: Mitochondrial Saccharomyces cerevisiae versus Cytosolic Candida albicans.* J. Am. Chem. Soc., 2011. **113**: p. 20878-20889.
9. Ozden, O., et al., *Acetylation of MnSOD directs enzymatic activity responding to cellular nutrient status or oxidative stress* Aging, 2011. **3**(2): p. 102-107.
10. Yang, L.C., et al., *Imaging of the intracellular topography of copper with a fluorescent sensor and by synchrotron X-ray fluorescence microscopy.* Proc. Natl. Acad. Sci., 2005. **102**(32): p. 11179-11184.

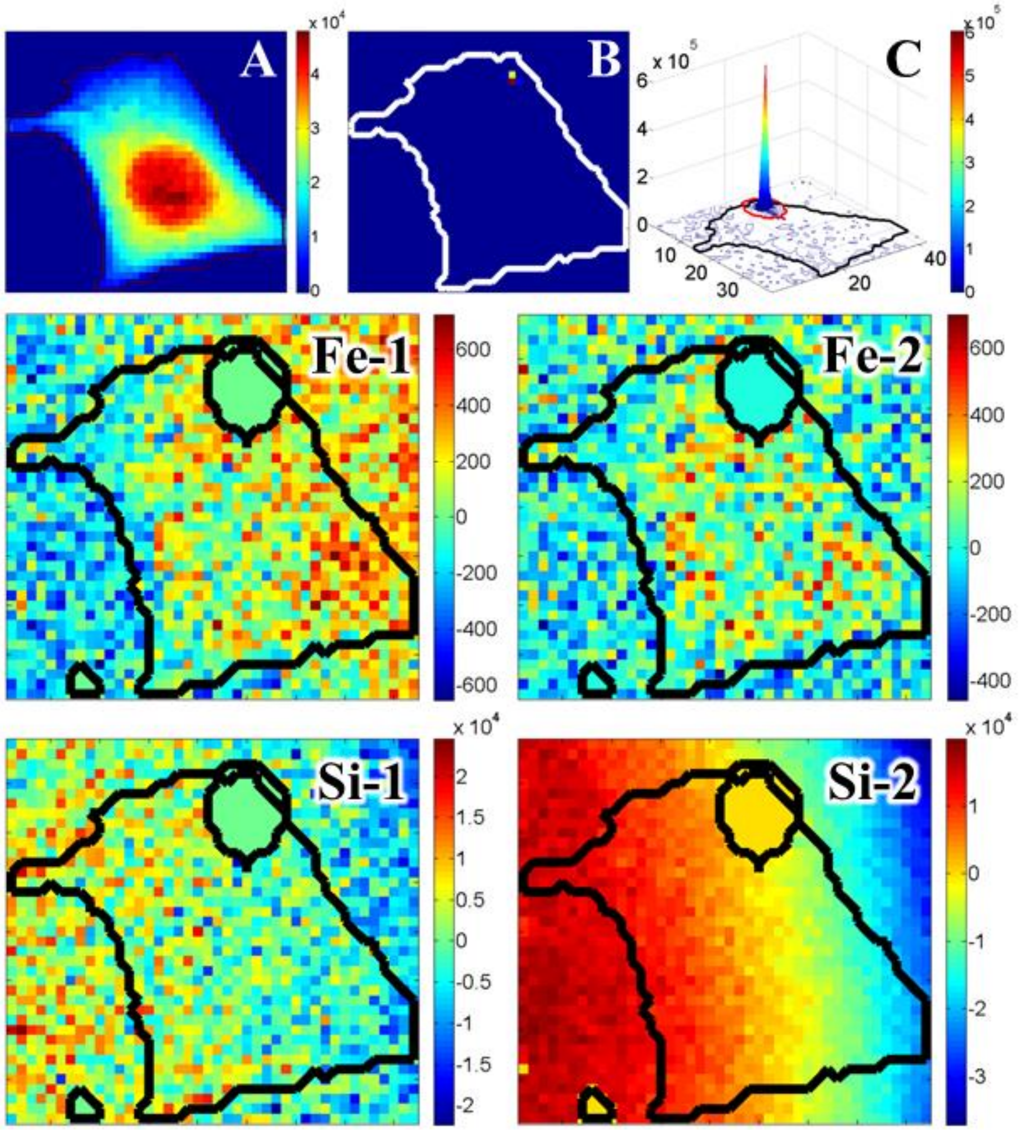

Figure VI.1 Comparison of Potential Backgrounds: (A) demonstrates the intensity of the K channel used to differentiate and segregate cell from background. (B) demonstrates the presence of a contaminant Fe particle. (C) demonstrates how the size of that contaminant particle, hidden in the auto scaling of the image, completely hides the detail of the Fe signal from the cell. The color bar to the right of C applies to B as well. The black and red lines in C mark the boundaries of the cell and cropped out pixels respectively. For the second and third rows, the contaminant from the Fe particle has been removed; both the removed contaminant dust and the cell have been outlined. (Fe-1 and Si-1) show the application of a blank where the amplitude was allowed to fluctuate. (Fe-2 and Si-2) show the application of a uniform blank.

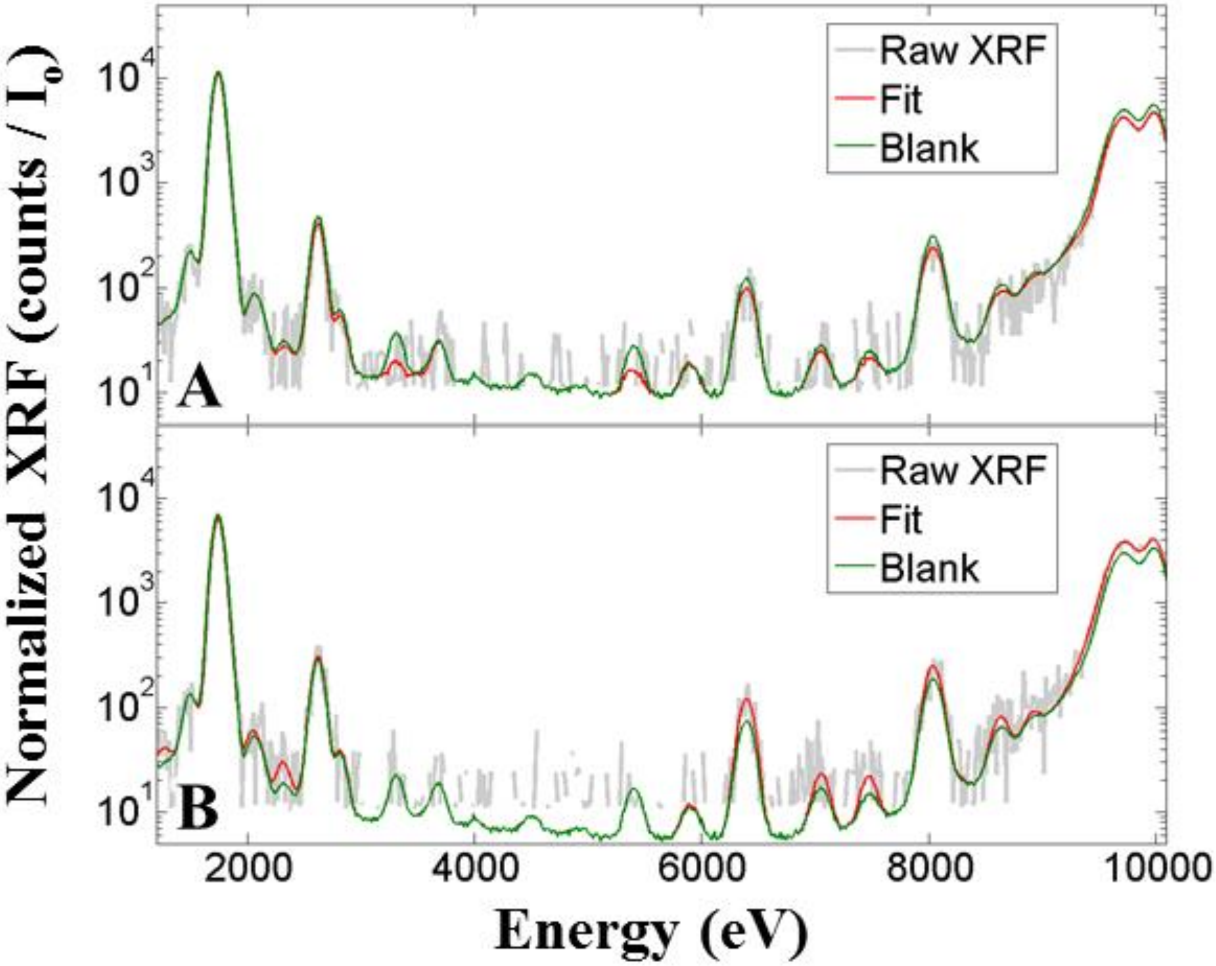

Figure VI.2 Raising and Lowering of the Blank at the Level of a Single Pixel when Allowing for a Variable Scaling Factor: (A) The spectrum of a single pixel showing the raising of the blank across the entire spectrum leading to a linear least squares solution where the fitted fluorescence for all other emissions would be negative. (B) The spectrum of a single pixel showing the lowering of the blank across the entire spectrum leading to a linear least squares solution where the fitted fluorescence for all other emissions would be greater than their true value.

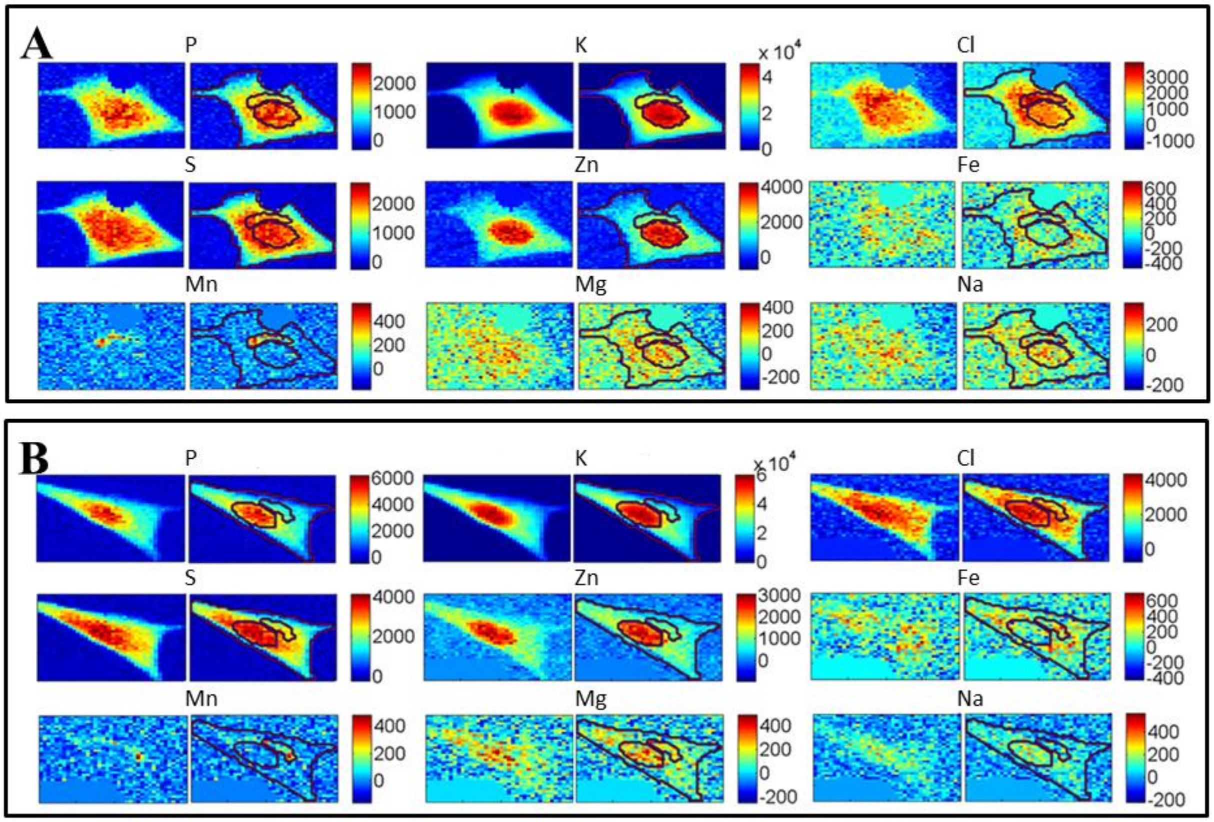

Figure VI.3 Visual Comparison of NIH3T3 cells under Cd(-) (A) and Cd(+) (B) conditions: A border was drawn around the nucleus using the K image intensity to draw the ROI. An ROI was also drawn around the area encasing the Mn.

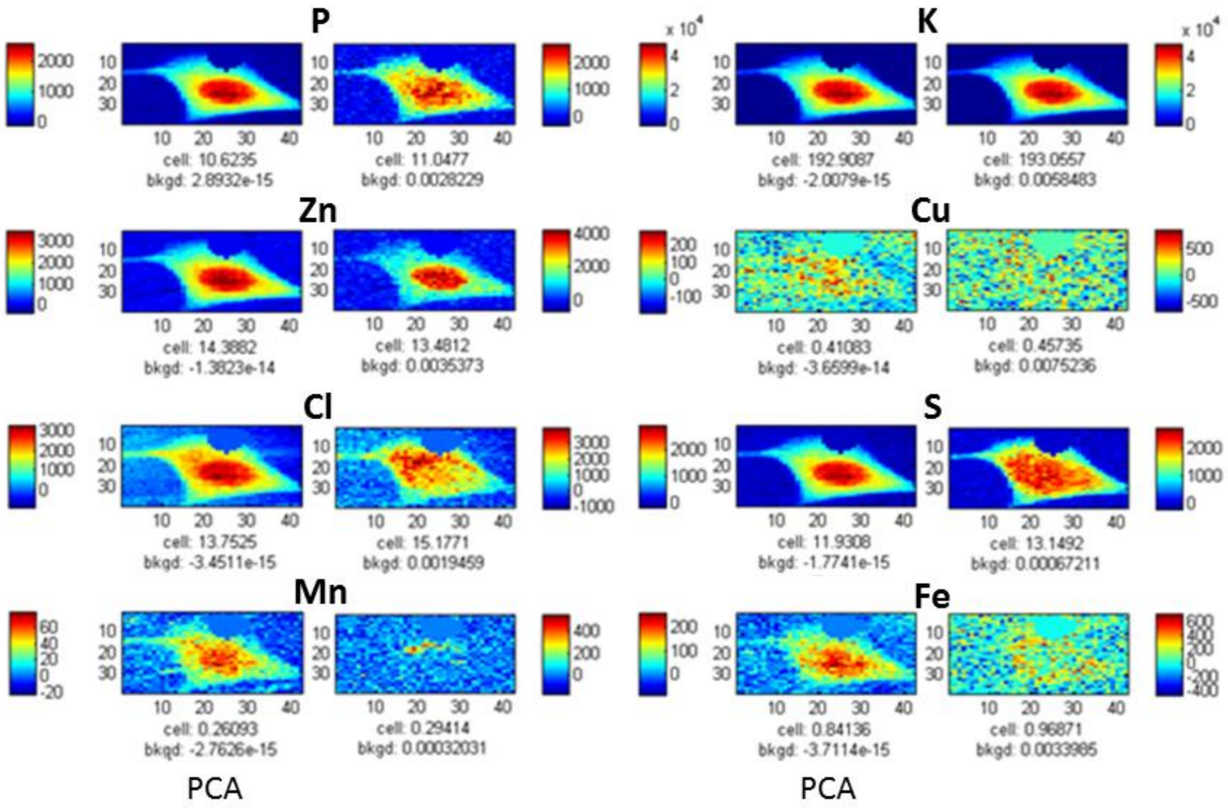

Figure VI.4 Comparison with PCA: The left image for each element pair corresponds to the image that was fit following PCA spectral filtering of noise. The right image of each pair corresponds to the image from the fitted set used in this study of NIH3T3 cells.

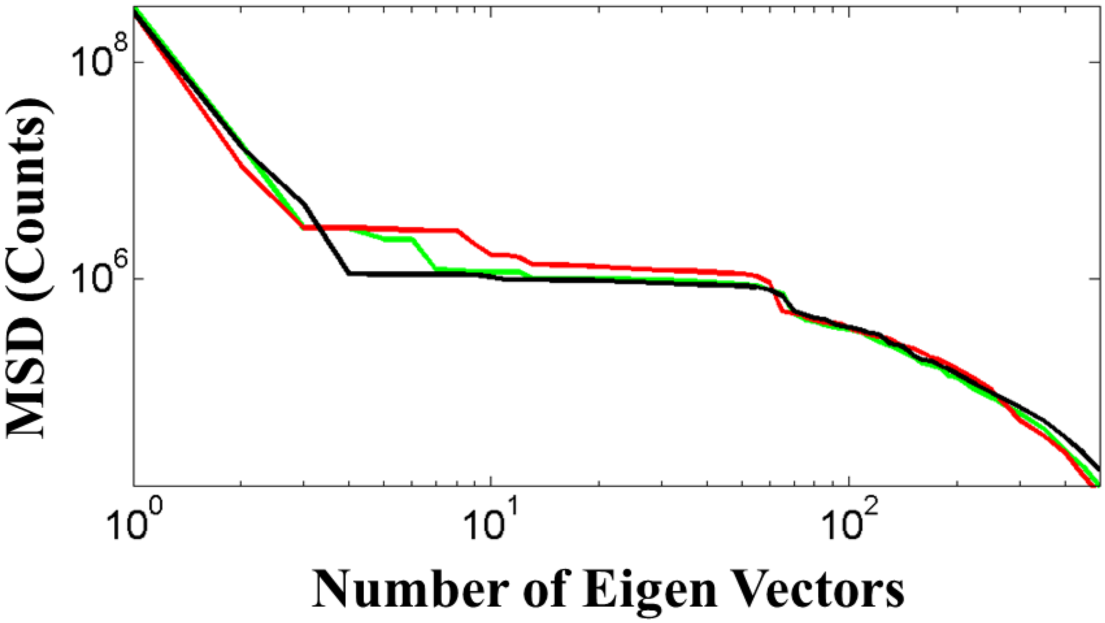

Figure VI.5 First 500 Eigen Vectors: Plot of the mean squared deviation between the reconstructed filtered data and the original data based on reconstruction using the first 500 eigenvectors.

Integrated Cellular Counts per Second			
	Variable Background Scale Factor	**Uniform Background**	**% Change**
S	13.11	13.15	0%
Mn	0.26	0.28	9%
Fe	0.82	0.95	16%
Cu	0.01	0.36	2457%
Zn	13.32	13.42	1%
K	193.04	193.01	0%
P	10.95	11.03	1%
Cl	14.88	15.29	3%

Table VI.1 The change in the integrated counts per second normalized by the upstream diamond diode for cell pixels

	A	**Cd(-)**		**Cd(+)**		**T - Statistic**			
		Mean	**% StDev**	**Mean**	**% StDev**	**Difference**	**df**	**t-stat**	**P**
Cell	P/K	**0.035**	18%	**0.050**	3%	**43%**	1	3.3	
	Zn/K	**0.388**	3%	**0.250**	5%	**-36%**	2	11.2	***
	S/K	**0.044**	6%	**0.056**	4%	**25%**	2	5.0	*
	Cl/K	**0.057**	2%	**0.071**	7%	**25%**	2	4.7	*
	Fe/K	**0.014**	9%	**0.011**	30%	**-17%**	3	1.1	
	Mn/K	**2.9E-03**	41%	**2.0E-03**	28%	**-31%**	1	1.0	

	B	**Cd(-)**		**Cd(+)**		**T - Statistic**			
		Mean	**% StDev**	**Mean**	**% StDev**	**Difference**	**df**	**t-stat**	**P**
Nucleus	P/K	**0.032**	19%	**0.046**	6%	**41%**	1	2.9	
	Zn/K	**0.434**	7%	**0.291**	8%	**-33%**	2	5.8	*
	S/K	**0.039**	14%	**0.045**	5%	**17%**	1	1.6	
	Cl/K	**0.049**	9%	**0.056**	8%	**14%**	2	1.7	
	Fe/K	**0.009**	12%	**0.005**	18%	**-47%**	2	4.7	*
	Mn/K	**2.4E-03**	29%	**1.0E-03**	52%	**-58%**	2	2.5	

	C	**Cd(-)**		**Cd(+)**		**T - Statistic**			
		Mean	**% StDev**	**Mean**	**% StDev**	**Difference**	**df**	**t-stat**	**P**
Cytosol	P/K	**0.037**	19%	**0.053**	3%	**42%**	1	3.0	
	Zn/K	**0.347**	4%	**0.221**	3%	**-36%**	1	11.5	
	S/K	**0.049**	4%	**0.063**	6%	**27%**	3	5.3	**
	Cl/K	**0.063**	5%	**0.081**	9%	**28%**	3	3.9	*
	Fe/K	**0.018**	10%	**0.016**	30%	**-13%**	3	0.8	
	Mn/K	**3.2E-03**	45%	**2.6E-03**	33%	**-20%**	1	0.6	

Table VI.2 K-Normalized Elemental Content: P-values < 0.05, 0.02, and 0.01 have been noted by *, **, and *** respectively. The N for Cd(-) and Cd(+) were 2 and 3, respectively.

CHAPTER VII: CONCLUSIONS AND FUTURE WORK

VII.1 CONCLUSION

This thesis has focused on the development of a novel probe for the investigation of single cell elemental content with an enhanced rate of sampling frequency. In the course of developing the instrument, the software that was written to analyze the data was adapted to the fitting of XRF imaging data. In doing so, the software was shown to give superior fits and identified some significant problems with spectral filtering using PCA [1] and with using a baseline to correct for a background. The implications of these problems should be thoroughly explored. We have already identified one study [2] that we believe gives misleading results due to PCA filtering of raw data. Further studies that have used PCA filtering need to be identified and the data should be refit without spectral filtering and those results compared with the previous results. The use of PCA to filter out noise associated with raw XRF data (*e.g.,* [1]) appears to afford a non-zero baseline across the dataset. This raises concerns about loss of precision from per-pixel baseline correction.

In terms of per-pixel baselines, a study should be done using tissues with sample free borders to identify an appropriate method for background correction when "non-sample" spectra are not available. This is potentially very important for "one-of-a-kind" samples where there is no possible blank, and the error associated with the baseline could introduce inaccuracies similar to those demonstrated in Chapter 5.

VII.2 FUTURE WORK

Future work from this thesis should focus on two things: 1) continued development of the cytometer and 2) M-BLANK program upgrades and enhancements.

There is still a lot left to improve with the cytometer. Since the He shroud showed significant signal improvement and background removal, future work should encase the entire instrument in the shroud. The detectors should be tied to x-, y-, z-, and rotation stages to optimize detector placement and guarantee that the Mo collimator is aligned properly.

Additionally, the detected count rate can be further enhanced by including a Maia detector [3] upstream from the sample to detect backscattering. Depending on the efficiency and sensitivity afforded by the Maia detector, removal of the 4-element detectors may be possible to make room for some other advancement not yet conceived.

Currently, M-BLANK does not account for the tailing of energies at the low energy side of peaks, nor does it account for the scattering continuum at low energies. The former can be seen in Figure 8 of Chapter 5. Additionally, M-BLANK does not account for pile up peaks or escape peaks. Referring again back to Figure 8 of Chapter 5, there exist peaks that we were not able to explain with single emission lines (*e.g.*, the peak to the right of Fe at ~6,650 eV).

The tailing function is important to studies herein as the Cd L-lines are slightly wider and directly underneath the K K-lines. The increased width of the group of Cd L-lines causes the series to be elevated (similar to the artifact identified with Ca quantitation from MAPS in chapter 5) to minimize the residual associated with the lower energy end of K. Because of this, the apparent Cd concentrations in Cd treated and untreated cells were identical.

Ultimately, M-BLANK has superior accuracy and precision. It is also much faster and allows for users to select for different combinations of elemental K, L, and M series emissions (see chapter 3) with almost an instantaneous feedback on the visual fit quality. Additionally, the raw data can be searched to identify the best combinations of emissions for the fitting of specific regions of the data; also, with almost instantaneous feedback.

Further studies should be performed with a data set fitted by the most current version of MAPS to verify these results. Ideally, that study would also involve comparisons with the fits obtained from other programs such as PyMca, AXIL, Datamuncher, and GeoPIXE [4].

VII.3 REFERENCES

1. Vogt, S., J. Maser, and C. Jacobsen, *Data analysis for X-ray fluorescence imaging.* J. Phys, 2003. **IV**(104): p. 617-622.
2. McRae, R., et al., *Correlative microXRF and optical immunofluorescence microscopy of adherent cells labeled with ultrasmall gold particles.* Journal of Structural Biology, 2006. **155**(1): p. 22-29.
3. Ryan, C.G., et al., *Elemental X-ray imaging using the Maia detector array: The benefits and challenges of large solid-angle.* Nuclear Instruments and Methods in Physics Research Section A: Accelerators, Spectrometers, Detectors and Associated Equipment, 2010. **619**(1-3): p. 37-43.
4. Alfeld, M. and K. Janssens, *Strategies for processing mega-pixel X-ray fluorescence hyperspectral data: a case study on a version of Caravaggio's painting Supper at Emmaus.* Journal of Analytical Atomic Spectrometry, 2015. **30**(3): p. 777-789.